STUDIES OF TERAHERTZ METAMATERIALS IN TRANSFORMATION OPTICS AND PLASMONICS

By

WEI CAO

Bachelor of Electrical Engineering
Tianjin University
Tianjin, P.R. China
2007

Master of Electrical Engineering
Tianjin University
Tianjin, P.R. China
2009

Submitted to the Faculty of the
Graduate College of the
Oklahoma State University
in partial fulfillment of
the requirements for
the Degree of
DOCTOR OF PHILOSOPHY
May, 2014

STUDIES OF TERAHERTZ METAMATERIALS IN TRANSFORMATION OPTICS AND PLASMONICS

Dissertation Approved:

Dr. Weili Zhang

Dissertation Adviser

Dr. Daniel R. Grischkowsky

Dr. Daqing Piao

Dr. Albert T. Rosenberger

ACKNOWLEDGEMENTS

I would never have been able to finish my dissertation without the guidance of my advisor and committee members, help from friends, and support from my family.

I would like to express my deepest gratitude to my advisor, Dr. Weili Zhang, for his excellent guidance, caring, patience, and providing me with an excellent atmosphere for doing research. His continual and convincing inspiration made possible the completion of this dissertation and the achievements in my research. I am always grateful for all the knowledge, wisdom and training from Dr. Zhang, which will keep benefiting me in my career.

I would also like to thank Dr. Daniel R. Grischkowsky for introducing me in the world of terahertz, and for guiding me in the spirit of scientific truth and excellence. My appreciation is extended to Dr. Daqing Piao and Dr. Albert T. Rosenberger for serving on my advisory committee. They were all very generous with their time, patience, and suggestions.

I would like to specially thank Dr. Ranjan Singh who inspired me a lot of thoughts on my research. I feel fairly fortunate to have had the opportunity to work with him all these years. The valuable discussions and advice from him have greatly improved my research and my dissertation. I am very proud of the quality of the works we did together.

Acknowledgements reflect the views of the author and are not endorsed by committee members or Oklahoma State University.

Very special thanks to Dr. John F. O'Hara. His beneficial teaching, assistance, and suggestions on numerical simulations have extensively improved my research.

It is also my pleasure to thank my team mates here at UTOL with whom I have enjoyed great many good times. I owe a lot to Dr. Xinchao Lu, Dr. Jianqiang Gu, and Dr. Zhen Tian for all your experimental training on the microfabrication and THz-TDS system. I want to thank my colleagues, Dr. Yongyao Chen, Ningning Xu, and Yihong Yang for all the helpful insights and discussions.

Thanks a lot Dr. Mingxia He. Without her valuable help, support, and motivation, I cannot accomplish my dream PhD degree for which I came to America.

I would like to express my deepest gratitude to my family. They were always supporting me and encouraging me with their best wishes, and have never ceased to convey utter confidence in my abilities.

Finally, I offer my regards and blessings to all of those who helped me in any respect during the completion of this dissertation.

Acknowledgements reflect the views of the author and are not endorsed by committee members or Oklahoma State University.

Name: Wei Cao Date of Degree: May, 2014

Institution: Oklahoma State University Location: Stillwater, Oklahoma

Title of Study: STUDIES OF TERAHERTZ METAMATERIALS IN TRANSFORMATION OPTICS AND PLASMONICS

Pages in Study: 139 Candidate for the Degree of Doctor of Philosophy

Major Field: Electrical Engineering

Scope and Method of Study:

Terahertz (THz) metamaterials in transformation optics and plasmonics were investigated. The metamaterial structures with a minimum feature size of 2 μm were fabricated using microelectronic lithography techniques. The transmission properties of THz radiation through these metamaterials were systematically investigated by using THz time-domain spectroscopy. Numerical simulations and theoretical calculations were carried out to further verify the experimental results.

Findings and Conclusions:

An invisibility cloak has successfully concealed both the geometrical and spectroscopic features of an alpha-lactose monohydrate absorber, making it undetectable from 0.3 to 0.6 THz. A broadband transformed Luneburg lens for THz imaging without geometric aberrations was numerically and experimentally demonstrated. A metamaterial induced transparency resonance with an extraordinary high quality factor was achieved by introducing a tiny asymmetry in the metamaterial structure. Furthermore, the tunable plasmon-induced transparency and slow light behavior can be generated by a thermally active superconductor-metal coupled resonator based hybrid THz metamaterial. At last, the polarization-dependent resonant transmission of THz pulses was explored through the plasmonic metamaterial patterned on a silver nanorod film with subwavelength hole arrays. The selective excitation of spoof surface plasmons derived from the anisotropic conductivity of the nanorod film was demonstrated.

ADVISER’S APPROVAL: Dr. Weili Zhang

TABLE OF CONTENTS

Chapter Page

LIST OF FIGURES

Figure Page

Figure Page

LIST OF SYMBOLS

A	Resonance amplitude
AgNR	Silver nanorod
ASRs	Asymmetric split ring resonators
c	Velocity of light in free space, $3 \times 10^8\ m/s$
CRRs	Close ring resonators
d	Thickness (μm)
E	Electric field (V/m)
EIT	Electromagnetically induced transparency
f	Filling ratio
FOM	Figure of merit
FDTD	Finite-difference time-domain
g	Geometric parameter
H	Magnetic field (A/m)
HDDA	Hexanediol diacrylate
i	Coordinate base
k	Wavevector (1/m)
k_x	Wavevector along x-direction (1/m)
k_y	Wavevector along y-direction (1/m)
k_{sp}	Wavevector of surface plasmons (1/m)

LC	Inductive-capacitive
m, *n*	Order of mode
n_r	Real refractive index
OAD	Oblique angle deposition
P	Periodicity (μm)
PIT	Plasmon-induced transparency
PμSL	Projection micro-stereo-lithography
QCM	Quasiconformal mapping
Q-factor	Quality factor
r	Reflection coefficient
SEM	Scanning electron microscope
SOS	Silicon-on-sapphire
SPs	Surface plasmons
SRRs	Split ring resonators
t	Transmission coefficient
T	Transmission
TDS	Time-domain-spectroscopy
TM	Transverse magnetic
UV	Ultra violet
v_g	Group velocity (m/s)
x	Charge oscillations
YBCO	Yttrium barium copper oxide
γ	Damping rate (THz)

δ	Detuning of resonance frequency (THz)
ε	Electric permittivity (F/m)
ε_i	Imaginary dielectric constant
ε_r	Real dielectric constant
κ	Coupling coefficient (THz^2)
$\mathit{\Lambda}$	Transformation operator
λ	Wavelength (μm)
μ	Magnetic permeability (H/m)
ρ	Resistivity (Ω·m)
φ	Phase shift (radian)
χ	Susceptibility
ω	Angular frequency (radian/s)
ω_p	Plasma frequency (THz)
Δt_g	Group delay (ps)

CHAPTER I

INTRODUCTION

Metamaterials are artificial materials with intentionally designed characteristics which allow both field ingredients of electromagnetic waves to couple to meta-atoms. Metamaterials are capable of achieving new electromagnetic properties and exciting applications with such double-handed electromagnetic waves, the most fascinating property being of a negative refractive index, which is most famous characteristic of electromagnetic wave propagation in materials.

In decades, the rapid development of artificially structured metamaterials has resulted in a large amount of phenomena that can hardly be fulfilled with natural materials. This is fairly good news for the researchers working in the terahertz (THz) frequency regime, mainly due to the introduction of metamaterials that can be essentially designed to have desired characteristics to THz radiation. Metamaterials have opened a promising pathway to artificially manipulating THz radiation by controlling the designed structures. It promises a wide range of applications, such as THz sources, lenses, switches, modulators, cloaking devices, filters and detectors [1-7].

In this dissertation, the first section describes the background of metamaterial-based invisibility cloaking and Luneburg lens by using transformation optics, high quality factor (Q-factor) metamaterial induced transparency and a thermal tunability in plasmon induced transparency, and a THz plasmonic metamaterial. The second section presents numerical and experimental studies of a THz invisibility cloak which is able to conceal a realistic object over a broadband THz frequency range and a transformed Luneburg lens for THz imaging. The third section describes numerical and experimental studies of metamaterial induced transparency with high Q-factor and its active control in a superconductor-metal hybrid metamaterial. At last, a conventional microscale metamaterial with nanoscale metallic rod array is numerically and experimentally explored for proof of conception studies of developing the novel THz devices.

CHAPTER II

FUNDAMENTAL BACKGROUND

2.1 Background of invisibility cloaking and Luneburg lenses

2.1.1 Invisibility cloaking

The invisibility cloaking has been a long-standing dream for many researchers over the decades. The introduction of transformation optics has revitalized this field by providing a general method to design material distributions to hide the subject from being detected [8,9]. By transforming space and propagation of electromagnetic waves, a three-dimensional (3D) object is perceived as having a reduced number of dimensions, in the form of points, lines, and thin sheets, making it “undetectable” judging from the scattered field [10,11].

Although a variety of cloaking devices have been reported at microwave and optical frequencies [12-17], the spectroscopically important THz regime [18,19] remained unexplored. Moreover, due to the difficulties in fabricating cloaking devices that are optically large in all three dimensions, hiding realistic 3D objects has yet to be demonstrated.

Transformation design is to use the coordinate transforms to design material objects. The material properties that give the same electromagnetic behavior as a distorted space are found from the transformation properties of the electromagnetic material property tensors [20]. The electric permittivity, ε (or the magnetic permeability, μ), transforms as a second rank tensor-density of unit weight [21]

$$\varepsilon^{i'j'} = \det(\Lambda_i^{i'})^{-1}\Lambda_i^{i'}\Lambda_j^{j'}\varepsilon^{ij}, \tag{2-1a}$$

$$\mu^{i'j'} = \det(\Lambda_i^{i'})^{-1}\Lambda_i^{i'}\Lambda_j^{j'}\mu^{ij}, \tag{2-1b}$$

where $\Lambda_i^{i'}$ is the transformation operator. When the bases denoted by the indices i and i' are coordinate bases, the transformation operator can be expressed as

$$\Lambda_i^{i'} = \frac{\partial x^{i'}}{\partial x^i}. \tag{2-2}$$

One should write the desired transformation in terms of spherical or cylindrical coordinates and use the corresponding unit basis to describe the material properties. Thus the total transformation operator is

$$\Lambda_{\hat{\imath}}^{\hat{\imath}'} = \Lambda_{i'}^{\hat{\imath}'}\Lambda_i^{i'}\Lambda_{\hat{\imath}}^{i}. \tag{2-3}$$

Then in spherical transformation the matrices are given by

$$\left(\Lambda_{i'}^{\hat{\imath}'}\right) = \begin{pmatrix} 1 & 0 & 0 \\ 0 & r' & 0 \\ 0 & 0 & r'sin\theta' \end{pmatrix}, \tag{2-4a}$$

$$\left(\Lambda_{\hat{\imath}}^{i}\right) = \begin{pmatrix} 1 & 0 & 0 \\ 0 & \frac{1}{r} & 0 \\ 0 & 0 & \frac{1}{rsin\theta} \end{pmatrix}. \tag{2-4b}$$

The transformation matrices for cylindrical coordinates are

$$\left(\Lambda_{i'}^{\hat{\imath}'}\right) = \begin{pmatrix} 1 & 0 & 0 \\ 0 & \rho' & 0 \\ 0 & 0 & 1 \end{pmatrix}, \tag{2-5a}$$

$$\left(\Lambda_{i'}^{\hat{\imath}'}\right) = \begin{pmatrix} 1 & 0 & 0 \\ 0 & \frac{1}{\rho} & 0 \\ 0 & 0 & 1 \end{pmatrix}. \tag{2-5b}$$

A new strategy for cloaking, named “carpet invisibility cloaking”, was proposed by Li and Pendry [11]. The carpet cloaking is able to hide an object invisible under a reflective surface by mimicking a flat ground plane. Based on complete cylindrical cloak and carpet cloak, it is natural to utilize half of complete cloak [12] to take advantage of its perfect invisibility property. Schematic diagram of the carpet cloak with semi-cylindrical reflective surface is illustrated in Fig. 2-1(a,b). If we consider a transformation lies within the *x*-*y* plane, the transformation from the virtual space (*r’, θ’, z’*) to the physical space (*r*, *θ*, *z*) in cylindrical coordinate is mathematically expressed as:

$$r' = R2 + \frac{R1-R2}{R1} r, 0 < r < R1, \tag{2-6a}$$

$$\theta' = \theta, 0 < \theta < \pi, \tag{2-6b}$$

$$z' = z, \tag{2-6c}$$

where R_1 and R_2 are the radii of the outer and inner circles in *x*-*y* plane, respectively. The transform from Cartesian coordinate to cylindrical coordinate is defined as:

$$r = \sqrt{x^2 + y^2}, 0 < r < R1, \tag{2-7a}$$

$$\theta = \arctan(y/x), 0 < \theta < \pi, \tag{2-7b}$$

$$z = z, \tag{2-7c}$$

Then in terms of this transformation the spatially varying electromagnetic properties in the physical space is

$$\varepsilon = diag(\frac{r'-R2}{r'}, \frac{r'}{r'-R2}, (\frac{R1}{R1-R2})^2 \frac{r'-R2}{r'}) \tag{2-8}$$

The performance of the invisibility cloak is demonstrated with simulations in Fig. 2-2. The carpet cloak is capable of mimicking a bump under the cloak as a flat mirror plane as shown in Fig. 2-1(c, e). For comparison, figure 2-1(d) illustrates that a bump without the cloak strongly scatters the incident beam. This serves as a numerical evidence of effectiveness of carpet cloak in controlling the trajectory of the incident beam. However, this scheme of transformation requires extreme material properties, which narrows the bandwidth and causes extreme difficulties in the fabrication of THz cloaks. In our scheme of carpet cloak, the bump located at the ground plane is defined by a cosine function with a height of h and a width of w.

$$x' = x, \tag{2-9a}$$

$$y' = y + (\frac{h}{2} cos\frac{2\pi x}{w} + \frac{h}{2})(\frac{w-2y}{w})^2, \tag{2-9b}$$

$$z' = z. \tag{2-9c}$$

The transformation defined by Eq. 2-9, is represented by the mesh grids shown in Fig. 2-2. In the mesh grids of the cloak with tiny cells, a smaller area of the transformed cell indicates a larger refractive index.

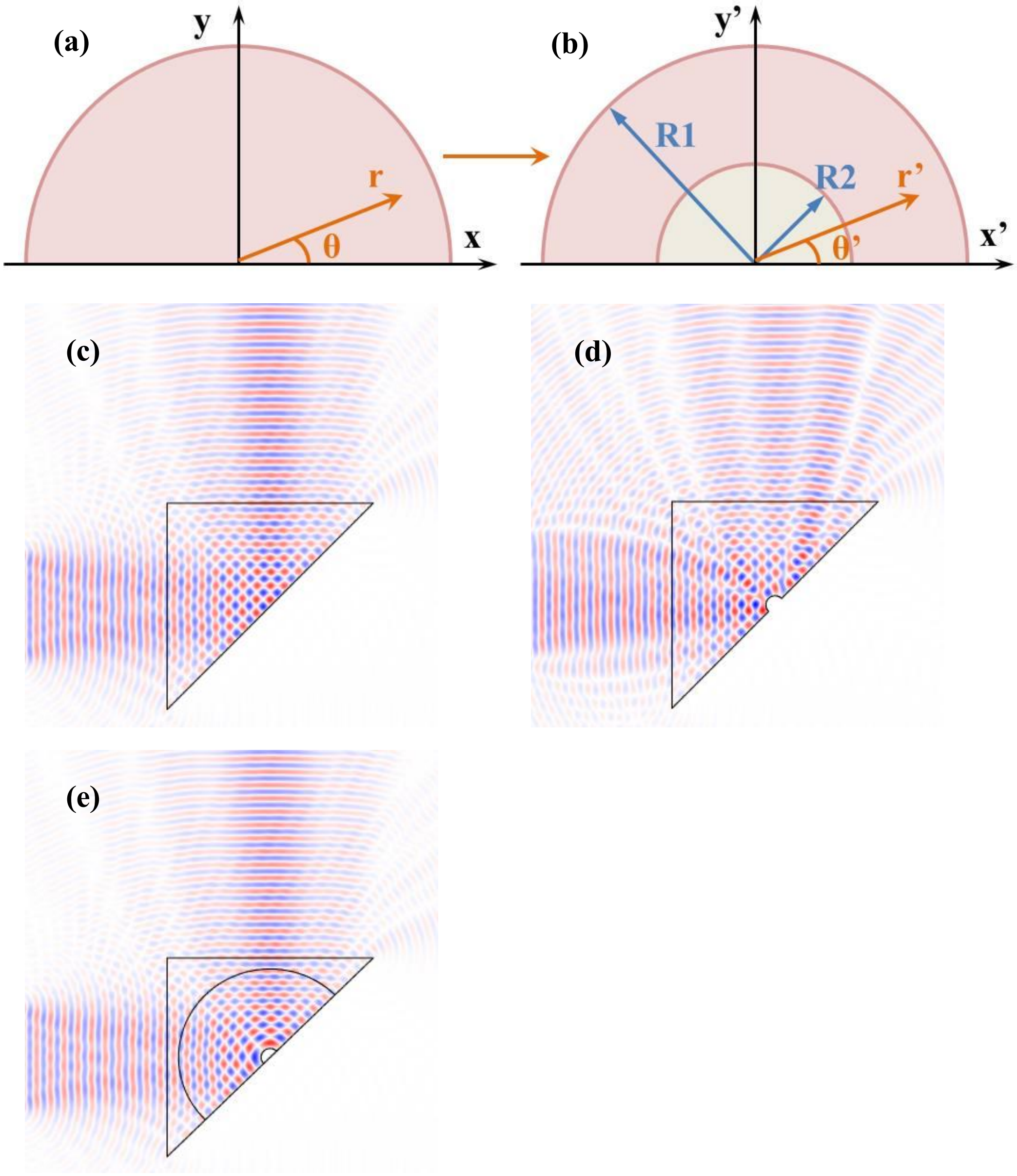

Figure 2-1. (a,b) Schematic diagram of spatial transformation for a carpet cloak with semi-cylindrical reflective surface, out of scale. The simulation indicates that (c) the reflective beam preserves the original shape of the incident beam. (d) A control simulation shows that the incident beam is strongly scattered by a bump without the cloak. (e) The invisibility cloak effectively transforms a bump into a flat reflective ground plane. The triangular area surround the cloak is the transition area reducing the scattering.

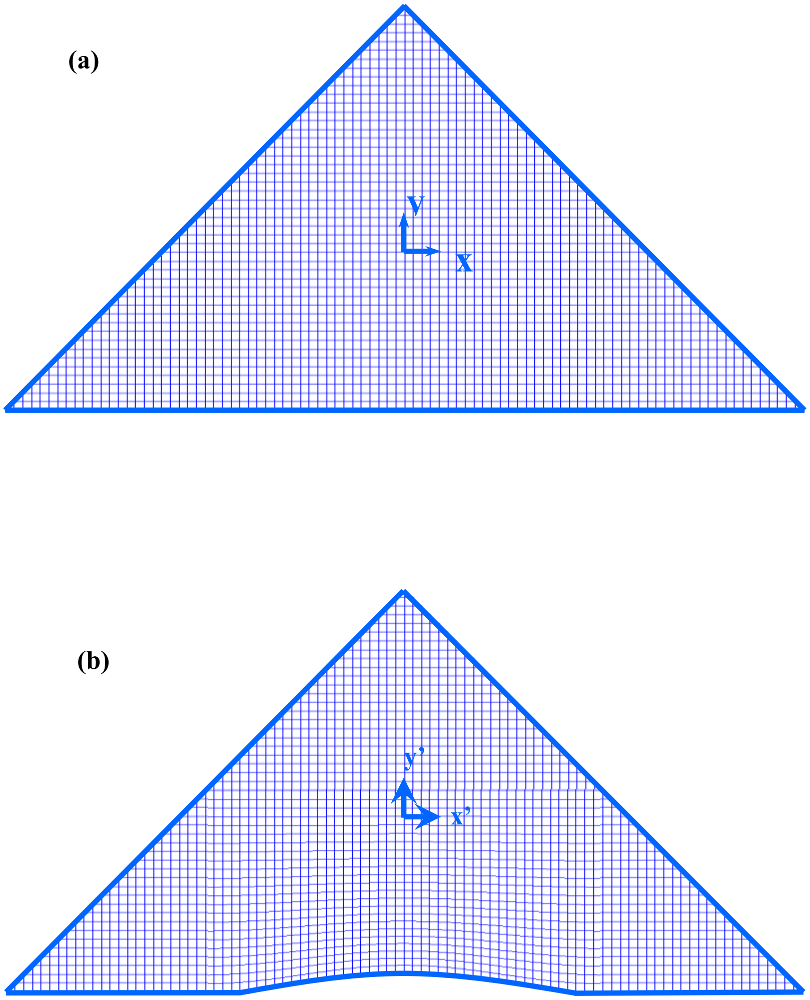

Figure 2-2. The mesh grids of the coordinate transformation for (a) the flat ground plane and (b) the bump functioned as Eq. 2-9 in *x'*-*y'* plane.

The cylindrical cloaks require extreme material parameters, which can only be obtained by using subwavelength resonant metamaterials with high loss and narrow bandwidth, limiting the practical applications of invisibility cloaking.

For carpet cloaking, the physical system is considered as an isotropic homogeneous medium of permittivity ε_{ref} and unit permeability induced by the coordinate transformation [11] is defined as:

$$\varepsilon = \varepsilon_{ref}/\sqrt{\det|\Lambda\Lambda^{\mathrm{T}}|}, \tag{2-10}$$

$$[\mu^{ij}] = \Lambda\Lambda^{\mathrm{T}}/\sqrt{\det|\Lambda\Lambda^{\mathrm{T}}|}, \tag{2-11}$$

where μ_T and μ_L are the principal values of the permeability tensor in the physical medium and the corresponding refractive indices are $n_T = \sqrt{\mu_L\varepsilon}$ and $n_L = \sqrt{\mu_T\varepsilon}$ for a plane wave traveling along the principal axes. In order to indicate the extent of anisotropy in the physical medium, there is

$$\frac{n_T}{n_L} + \frac{n_L}{n_t} = \frac{Tr(\Lambda\Lambda^{\mathrm{T}})}{\sqrt{\det|\Lambda\Lambda^{\mathrm{T}}|}}. \tag{2-12}$$

A smaller value of $\frac{Tr(\Lambda\Lambda^{\mathrm{T}})}{\sqrt{\det|\Lambda\Lambda^{\mathrm{T}}|}}$ indicates a smaller anisotropy.

The average refractive index n with respect to the reference medium is

$$n = \sqrt{n_T n_L}/\sqrt{\varepsilon_{ref}}, \tag{2-13}$$

$$\mu_T\mu_L = 1. \tag{2-14}$$

Thus

$$n^2 = \frac{\varepsilon}{\varepsilon_{ref}} = 1/\sqrt{det|\Lambda\Lambda^{\mathrm{T}}|}. \tag{2-15}$$

In this report, we present the first experimental demonstration of a 3D THz cloaking device fabricated using a scalable Projection Microstereolithography process. The cloak operates at a broad frequency range between 0.3 and 0.6 THz, and is placed over an α-lactose monohydrate absorber with rectangular shape. Characterized using angular-resolved reflection THz time-domain spectroscopy (THz-TDS) [22], the results indicate that the THz invisibility cloak has successfully concealed both the geometrical and spectroscopic signatures of the absorber, making it undetectable to the observer.

2.1.2 Transformed Luneburg lenses

Lenses are indispensible optical instruments, but most conventional lenses suffer from aberrations because the focus depends on the direction of incidence and deteriorates off axis. Luneburg lens is an extraordinary optical device with 0 F-number, infinitely wide field of view, and the capability of perfectly focusing electromagnetic waves from any direction to points on the surface of the lens with no aberrations of any order. The Luneburg lens is a sphere composed of an isotropic medium with spherically symmetric gradient refractive index functional form [21]

$$n_L(r) = \sqrt{2 - \frac{r^2}{R^2}}. \tag{2-16}$$

where R is the radius of the sphere lens. The index is 1 on the surface of the sphere lens boundary, and $\sqrt{2}$ at its center. The gradient refractive index is shown in Fig. 2-3(a). The Luneburg lens can focus parallel rays from any direction to a point on the opposite side of the sphere as shown in Fig. 2-3(b).

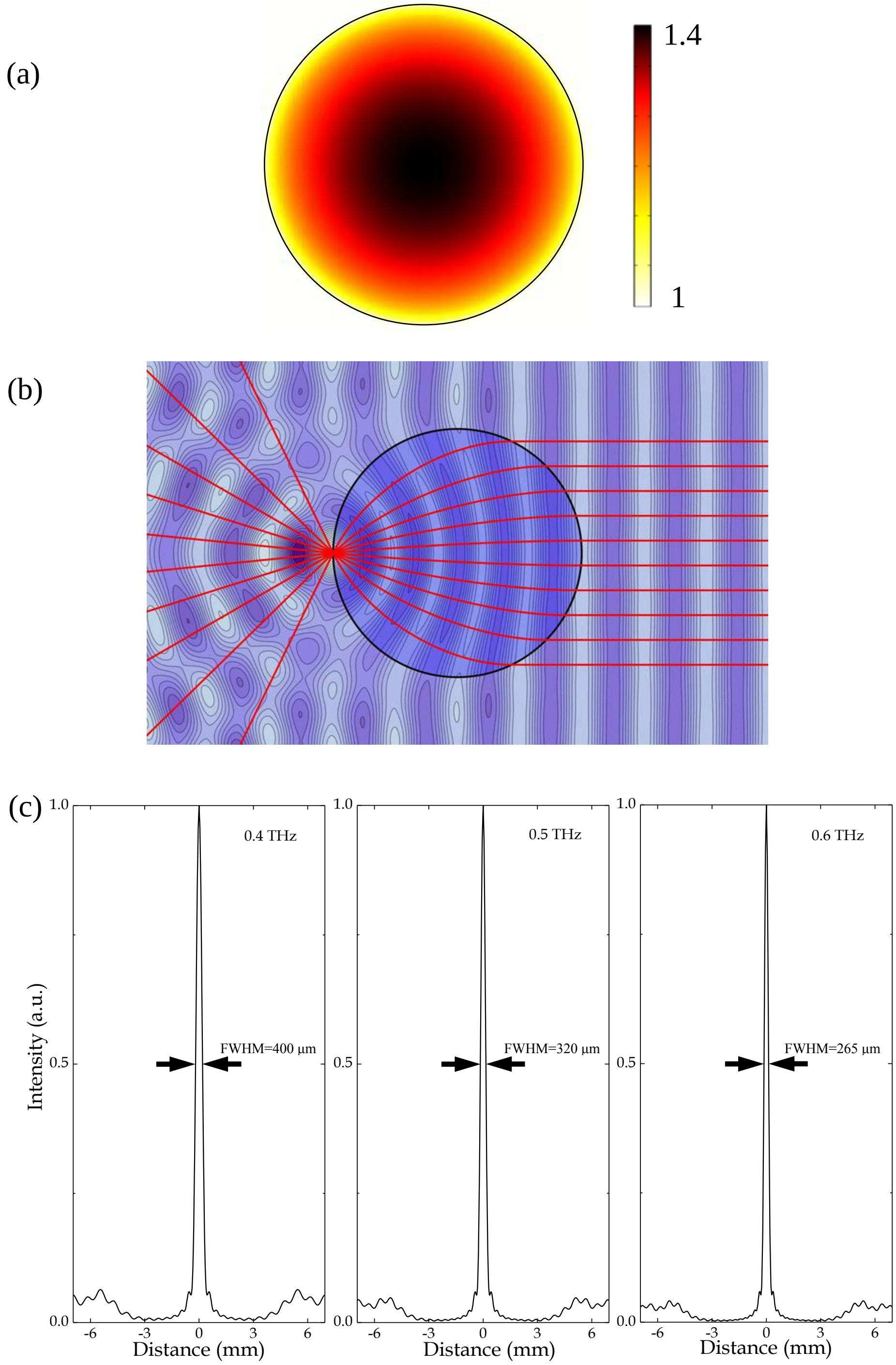

Figure 2-3. (a) Gradient refractive index distribution of Luneburg lens. (b) The Luneburg lens focuses all light rays (red curves) propagating in one direction at the point on its surface [23]. (c) Simulated diameters of the focal spot at different frequencies.

As the lens is rotationally symmetric it focuses light from all directions equally well. As a result, the Luneburg lens is an ideal lens free from optical aberrations. In figure 2-3(b), one can see that the focal spot is about half a wavelength wide. Its focus size is dependent on the wavelength of the light, being larger for longer wavelengths. In Fig. 2-3(c), the simulated (FWHM) diameters of the focal spots are about 265 μm at 0.6 THz (wavelength of 500 μm), 320 μm at 0.5 THz (wavelength of 600 μm), and 400 μm at 0.4 THz (wavelength of 750 μm).

Despite these remarkable and nearly ideal focusing properties, the Luneburg lens is rarely used. There are two reasons for this. One is that the focal plane is spherical, requiring a spherical focal-plane detector-array [21]. It is inconvenience in many applications. The second is the need for precise control of the spatially varying refractive index profile. The idea of the transformed Luneburg lens is to transform the Luneburg lens' spherical focal plane into a planar one with keeping its imaging properties. There is a simple example to transform a spherical image surface of Luneburg lens to a flattened plane,

$$x' = x, \tag{2-17a}$$

$$y' = \frac{1}{2}\left(y + \sqrt{R^2 - x^2}\right), \tag{2-17b}$$

$$z' = z. \tag{2-17c}$$

These transformation equations apply on the domain in which $\sqrt{x^2 + y^2} < R$, where R is the radius of the sphere.

In this case, the transformation lies within the *x*-*y* plane, the Jacobian matrix can be of the form:

$$\Lambda = \begin{pmatrix} \frac{\partial x\prime}{\partial x} & \frac{\partial x\prime}{\partial y} & 0 \\ \frac{\partial y\prime}{\partial x} & \frac{\partial y\prime}{\partial y} & 0 \\ 0 & 0 & 1 \end{pmatrix}. \qquad (2\text{-}18)$$

The coordinate transformation matrix of Eq. 2-17 can be obtained as:

$$\Lambda = \begin{pmatrix} 1 & 0 & 0 \\ -\frac{x}{2\sqrt{R^2-x^2}} & \frac{1}{2} & 0 \\ 0 & 0 & 1 \end{pmatrix}. \qquad (2\text{-}19)$$

The constitutive tensor for the permittivity becomes

$$\varepsilon = \begin{pmatrix} 2 & -\frac{x}{\sqrt{R^2-x^2}} & 0 \\ -\frac{x}{\sqrt{R^2-x^2}} & \frac{1}{2}(1+\frac{x^2}{R^2-x^2}) & 0 \\ 0 & 0 & 2 \end{pmatrix}. \qquad (2\text{-}20)$$

Thus a spherical image surface of Luneburg lens is transformed to a flattened plane with a 180 ° field-of-view, which is equivalent to an infinite object. The flattened plane is a finite area equal to or less than the diameter of the Luneburg lens. An infinite object is impossible to map into a finite area without distortion. Thus, the field of view should be restricted. If the field of view is set as θ, a transformation is as follows:

$$x' = x, \qquad (2\text{-}21a)$$

$$y' = \frac{1}{2}(y + \frac{Rcos\frac{\theta}{2}y}{\sqrt{R^2-x^2}} + \sqrt{R^2-x^2} + Rcos\frac{\theta}{2}), \qquad (2\text{-}21b)$$

$$z' = z. \qquad (2\text{-}21c)$$

The transformation defined by Eq. 2-21, is represented by the mesh grids presented in Fig. 2-4, which applies on the domain where $x < Rcos\frac{\theta}{2}$, a field-of-view equal to 82.9 °

in our flattened Luneburg lens design. In the meshing grids of transformed domain with tiny cells of size $\delta \times \delta$, a smaller area of the transformed cell $\sqrt{det|\Lambda\Lambda^{\mathrm{T}}|}\delta^2$ means a larger refractive index n.

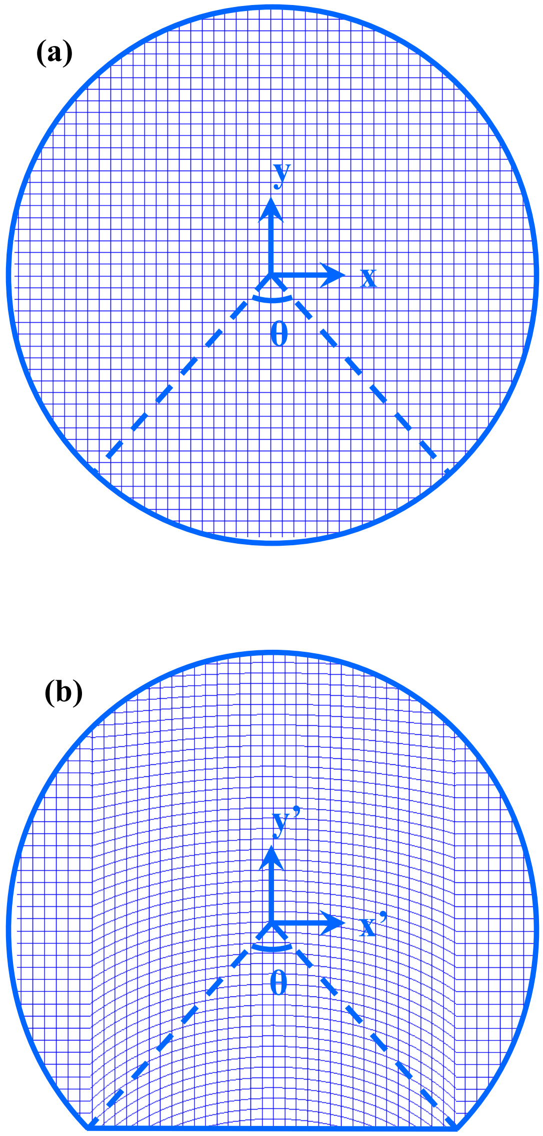

Figure 2-4. The mesh grids of the coordinate transformation for (a) the spherical Luneburg lens and (b) the flattened Luneburg lens with a θ field-of-view in x'-y' plane.

2.2 Background of metamaterial induced transparency

2.2.1 Electromagnetically induced transparency

Electromagnetically induced transparency (EIT) is a quantum effect caused by interference between coherences excited in the atoms by electromagnetic fields. A three-level atomic system coupled to two laser fields usually exhibits interference effects between probability amplitudes at a resonance transition frequency that may either lead to an enhancement or cancellation of absorption. This interference is analogous to constructive and destructive interference observed in the classical waves. It is known that EIT-like effects are in general not restricted to systems supporting quantum mechanical states and can in principal be observed in classical systems as well. A typical physical analogy in mechanical model is shown in Fig. 2-5(a) [24].

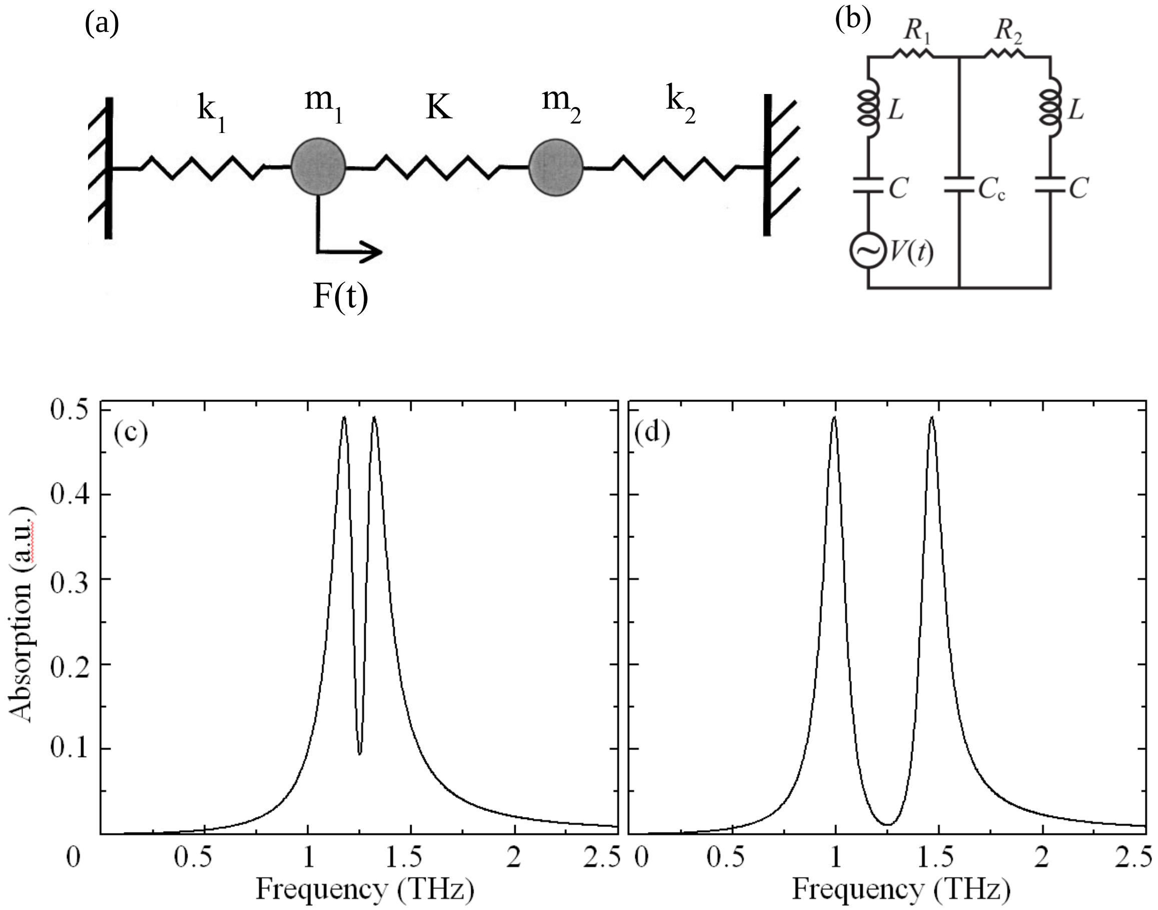

Figure 2-5. Typical physical analogy in a mechanical and an electrical model. (a) An EIT-like effect analogy in a mechanical system. (b) Equivalent circuit for electrical analogue. (c) and (d) The frequency dependence of the absorption spectra for the different coupling.

2.2.2 EIT analogy in mechanical and electrical models

The EIT-like effect can be modeled as a simple harmonic oscillator, consisting of particle 1 with mass m_1 attached to two springs with spring constants k_1 and K. The spring with constant k_1 is attached to a wall, while the other spring is attached to a second particle of mass m_2 and initially kept immobile at a fixed position. Particle 1 is also subject to a harmonic force $\mathcal{F}_s = Fe^{-i(\omega_s t+\phi_s)}$. If particle 2 is allowed to move, and subject only to the forces from the spring of constant K and a third spring of constant k_2 attached to a wall, the absorption profile is similar to EIT-like effect. For simplicity, consider the case $k_1 = k_2 = k$ and $m_1 = m_2 = m$. Atom is modeled as particle 1 with resonance frequency ω_1. The pump field is simulated by the coupling of particle 1 to the second particle via the spring of constant K. The probe field is then modeled by the harmonic force acting on the particle 1. The motion of particle 1 and 2 in terms of the displacements x_1 and x_2 from their respective equilibrium positions can be expressed [24]

$$\ddot{x}_1(t) + \gamma_1\dot{x}_1(t) + \omega^2 x_1(t) - \Omega_r^2 x_2(t) = \frac{F}{m} e^{-i\omega_s t}, \tag{2-22a}$$

$$\ddot{x}_2(t) + \gamma_2\dot{x}_2(t) + \omega^2 x_2(t) - \Omega_r^2 x_1(t) = 0. \tag{2-22b}$$

Consider $\phi_s = 0$ for the probe force without loss of generality. Set $\Omega_\mathrm{r}^2 = K/m$, the frequency associated with the coherent coupling; γ_1 and γ_2 are the losses on particle 1 and 2, respectively, $\gamma_2 \ll \gamma_1$.

Suppose $x_1(t)$ is as follows

$$x_1(t) = Ne^{-i\omega_s t}, \tag{2-23}$$

where *N* is a constant. After assuming a similar expression for $x_2(t)$ and substituting in Eq. (2-22),

$$x_1(t) = \frac{(\omega^2-\omega_s^2-i\gamma_2\omega_s)Fe^{-i\omega_s t}}{m[(\omega^2-\omega_s^2-i\gamma_1\omega_s)(\omega^2-\omega_s^2-i\gamma_2\omega_s)-\Omega_r^4]}. \tag{2-24}$$

Consider the mechanical power *P*(*t*) dissipated in particle 1 has the form

$$P(t) = Fe^{-i\omega_s t}\dot{x}_1(t). \tag{2-25}$$

Thus, the energy dissipation as a function of frequency is obtained as follows [24]

$$P_s(\omega_s) = -\frac{2\pi iF^2\omega_s(\omega^2-\omega_s^2-i\gamma_2\omega_s)}{m[(\omega^2-\omega_s^2-i\gamma_1\omega_s)(\omega^2-\omega_s^2-i\gamma_2\omega_s)-\Omega_r^4]}. \tag{2-26}$$

It is worth mention that the dissipation rate γ_2, associated with the energy loss of the pumping oscillator, must be much smaller than γ_1 in order to coherently drive the oscillation of particle 1. Figure 2-5(c,d) show the frequency dependence of the absorption for the different coupling.

The above mechanical model can be also converted to an equivalent electrical circuit to achieve EIT-like effect, shown in Fig. 2-5(b) [25]. A double resistive-inductive-capacitive (RLC) circuit with inductance *L* and capacitance *C* coupled by a shared capacitor C_c. The two circuits have a different resistance R_1 and R_2, respectively. The power delivered by the applied voltage source of magnitude *V* to the circuit equals [25]

$$P(\omega) = Re\frac{i\omega\frac{V^2}{2}(L\omega^2-iR_2\omega-\frac{1}{C_\parallel})}{\frac{1}{C_c^2}-(L\omega^2-iR_2\omega-\frac{1}{C_\parallel})(L\omega^2-iR_1\omega-\frac{1}{C_\parallel})}, \tag{2-27}$$

where $C_{\parallel} = (\frac{1}{C} + 1/C_c)^{-1}$. The dissipation minimum, which occurs approximately at the resonance frequency, can be approximated by $p \approx (C_c^2/C_{\parallel}L)(R_2V^2/2)$ if it is assumed that the losses are small $(R_1R_2 < LC_{\parallel}/C_c^2)$. It will achieve the right side current loop with low enough resistance to obtain a pronounced dissipation minimum in the power spectrum of the circuit. A certain coupling frequency corresponds to a pronounced EIT-like effect, where the strong dispersion occurs. This very steep dispersion is responsible for the extremely slow group velocity [24, 26]. The frequency dependence of the absorption for the different coupling is shown in Fig. 2-5(c,d).

Group velocity gives a reasonable measure of the speed at which a pulse travels [27]. A pulse of electromagnetic waves is a wave packet that is composed of an infinite number of monochromatic component waves, where constructive and destructive interference among the waves defines the shape and location of the pulse envelope in space and time. When the pulse propagates through a material system, each monochromatic component wave travels at a different speed because of the frequency dependence of refractive index, resulting in a shift (relative to vacuum propagation) of the regions of constructive and destructive interference.

To recall the concept of group velocity, consider a wave packet as a function of position x and time t, wave function $\Psi(x,t)$ as a summation of individual Fourier components, each of whose amplitudes is given by the value of $\Phi(k)$ at that particular k. One can extend each of the Fourier terms into a plane wave corresponding to that value of k, by introducing the frequency term via [28]

$$\Psi(x,t) = \frac{1}{\sqrt{2\pi}} \int_{-\infty}^{\infty} \phi(k) e^{i(kx-\omega t)} dx, \tag{2-28}$$

where ω is implicitly a function of k. If the main frequency corresponds to the peak of the momentum wave function, then the frequency can be expressed as

$$\omega(k) = \omega(k_0) + (k - k_0)\frac{\partial \omega}{\partial k}|_{k=k_0} + \cdots. \quad (2\text{-}29)$$

The equation above defines the dispersion across the wave packet, as it gives the gradual change in frequency for different components of the wave packet. To understand how the dispersion affects the propagation of the wave functions, we insert Eq. (2-29) into Eq. (2-28), and define the difference variable $u = k - k_0$. Then, [28]

$$\Psi(x,t) = \frac{1}{\sqrt{2\pi}} e^{i(k_0 x - \omega_0 t)} \int_{-\infty}^{\infty} \phi(u + k_0) e^{i(ux - \omega\prime ut)} du, \quad (2\text{-}30)$$

where $\omega_0 = \omega(k_0)$ and $\omega_0{}' = \frac{\partial \omega}{\partial k}|_{k=k_0}$. The higher-order terms of Eq. (2-29) are neglected, as the first two terms are the most significant. Then, after some algebra

$$\Psi(x,t) = e^{-i(\omega_0 - \omega\prime k_0)t}\Psi(x - \omega' t, 0). \quad (2\text{-}31)$$

Thus, the average velocity of the wave packet in position space is given by the group velocity

$$\upsilon_{\mathrm{g}} = \omega' = \frac{\partial \omega}{\partial k}|_{k=k_0}. \quad (2\text{-}32)$$

$$\omega = \frac{kc}{n_r}. \quad (2\text{-}33)$$

where n_r is the real part of the refractive index, then substituting Eq. (2-33) into Eq. (2-32) leads to:

$$\upsilon_{\mathrm{g}} = \frac{c}{n_r} - \frac{kc}{n_r{}^2}\frac{\partial n_r}{\partial \omega}\frac{\partial \omega}{\partial k}. \quad (2\text{-}34a)$$

$$\upsilon_g = \frac{c}{n_r + \omega\frac{\partial n_r}{\partial \omega}}. \tag{2-34b}$$

2.2.3 Theoretical calculation of metamaterial analogue of EIT

The metamaterial analogy of EIT can be explained by the coupling of a bright mode and a dark mode. In developing an analogy of EIT a significant difference in the Q-factor of the bright and dark modes is required. The bright mode strongly couples with the radiation field resulting in a low Q-factor while the dark mode weakly couples to the incident field showing a large Q-factor. The near field interaction between the two modes in the EIT metamaterial unit cell introduces a destructive interference leading to a transparency window with strong suppression of loss and a large dispersion at the transparency resonance. In the metamaterial analogy of EIT, in order to explore the physical origin, the widely used coupled Lorentz oscillator model is applied to analyze the interference [29]. The equations are described as follows:

$$\ddot{x}_1 + \gamma_1 \dot{x}_1 + {\omega_0}^2 x_1 + \kappa x_2 = gE, \tag{2-35a}$$

$$\ddot{x}_2 + \gamma_2 \dot{x}_2 + (\omega_0 + \delta)^2 x_2 + \kappa x_1 = 0, \tag{2-35b}$$

where x_1, x_2, γ_1, and γ_2 are the charge oscillations and the damping rates of bright and dark modes, respectively; ω_0 is the resonance frequency of bright model; δ is the detuning of the resonance frequency of dark mode to bright mode; κ denotes the coupling coefficient between the two modes; g is the geometric parameter indicating the coupling strength from the incident electric field to the bright mode; E is the incident electric field. The effective susceptibility χ_e of the metamaterial is as function of γ_1, γ_1, δ, and κ. The susceptibility of the metamterial layer with a thickness d is of form as $\chi = \chi_e/d$ [30].

T_{MM} is the Fabry-Perot interference transmission of the metamaterial layer.

$$T_{MM}(\omega) = \frac{t_1 t_2 e^{i\varphi}}{1 - r_1 r_2 e^{2i\delta}}, \tag{2-36}$$

$$t_1 = \frac{2n_0}{n_0 + n_{MM}}, t_2 = \frac{2n_{MM}}{n_{MM} + n_{sub}}, \tag{2-37}$$

$$r_1 = \frac{n_0 - n_{MM}}{n_0 + n_{MM}}, r_2 = \frac{n_{sub} - n_{MM}}{n_{sub} + n_{MM}}, \tag{2-38}$$

$$\varphi = \frac{\omega d n_{MM}}{c}. \tag{2-39}$$

The transmission of the material layer can be calculated by substituting Eq. (2-37)-(2-39) into Eq. (2-36).

$$|T_{MM}(\omega)| = |\frac{4 n_0 n_{MM} e^{i\frac{\omega d n_{MM}}{c}}}{(n_{MM} + n_{sub})(n_0 + n_{MM}) - (n_{sub} - n_{MM})(e^{i\frac{2\omega d n_{MM}}{c}})}|, \tag{2-40}$$

where n_0, n_{sub}, and $n_{MM} = \sqrt{1 + \chi_e / d}$ are the refractive index of air, substrate and metamaterial, respectively; t_1 and r_1 are the transmission coefficient and reflection coefficient at the interfaces between air and metamaterial layer, respectively; t_2 and r_2 are the transmission coefficient and reflection coefficient at the interfaces between substrate and metamaterial layer, respectively. φ denotes the phase shift in the metamaterial layer, and d is its thickness. c is the light velocity in vacuum. As the metamaterial layer is fairly thin compared with the wavelength of the THz incident beam, the transmission of the metamterial layer can be approximately as function of the near field susceptibility as,

$$|T_{MM}(\omega)| = |\frac{c(1 + n_{sub})}{c(1 + n_{sub}) - i\omega\chi_e}|, \tag{2-41}$$

In many photonic applications, it is required that metamaterials possess high Q-factor unit resonators. In practice, however, the scattering losses exist, which seriously damp the oscillation life-time of metamateril excitation [31,32]. The Q-factor in symmetric split-ring resonators (SRRs) usually undergoes a strong coupling to free space radiation, resulting in high radiative losses [33,34]. In order to overcome this drawback, the radiative losses can be mostly suppressed by a slight break in symmetry, regarding Fedotov's demonstration that high Q-factor can be fulfilled depending on dark modes [35]. In a pioneering work, Ranjan *et al*. recently demonstrated that metamaterial induced transparency can be evoked in a single THz Fano resonator consisting of a square two-gap SRR array excited at normal incidence by an electric field, which is parallel to the gap containing the arms of the SRR [36,37]. At the same time the Q-factor for such resonator is still not high enough due to the limited resolution of the measurement system. In this report, we experimentally achieve the asymmetric single SRR as unit cells for extraordinary high Q-factor metamaterials by using a 10.5-mm-thick silicon substrate to fulfill a long term measurement in time domain and to achieve high resolution in frequency domain. We experimentally prove that with high resolution, the asymmetric split-ring resonators (ASRs) reach the Q-factor that is approximately three times higher than the ones observed in the previous measurement situation.

Once one of the two gaps is moved off the center of the arm, a super high Q-factor metamaterial induced transparency window turns out. The off center movement of one of the two gaps causes out-of-phase oscillation and a destructive interference due to the coupling between two arms of ASR. The theoretical calculations and measured amplitude transmission spectra are illustrated in Fig. 2-6 (a,b).

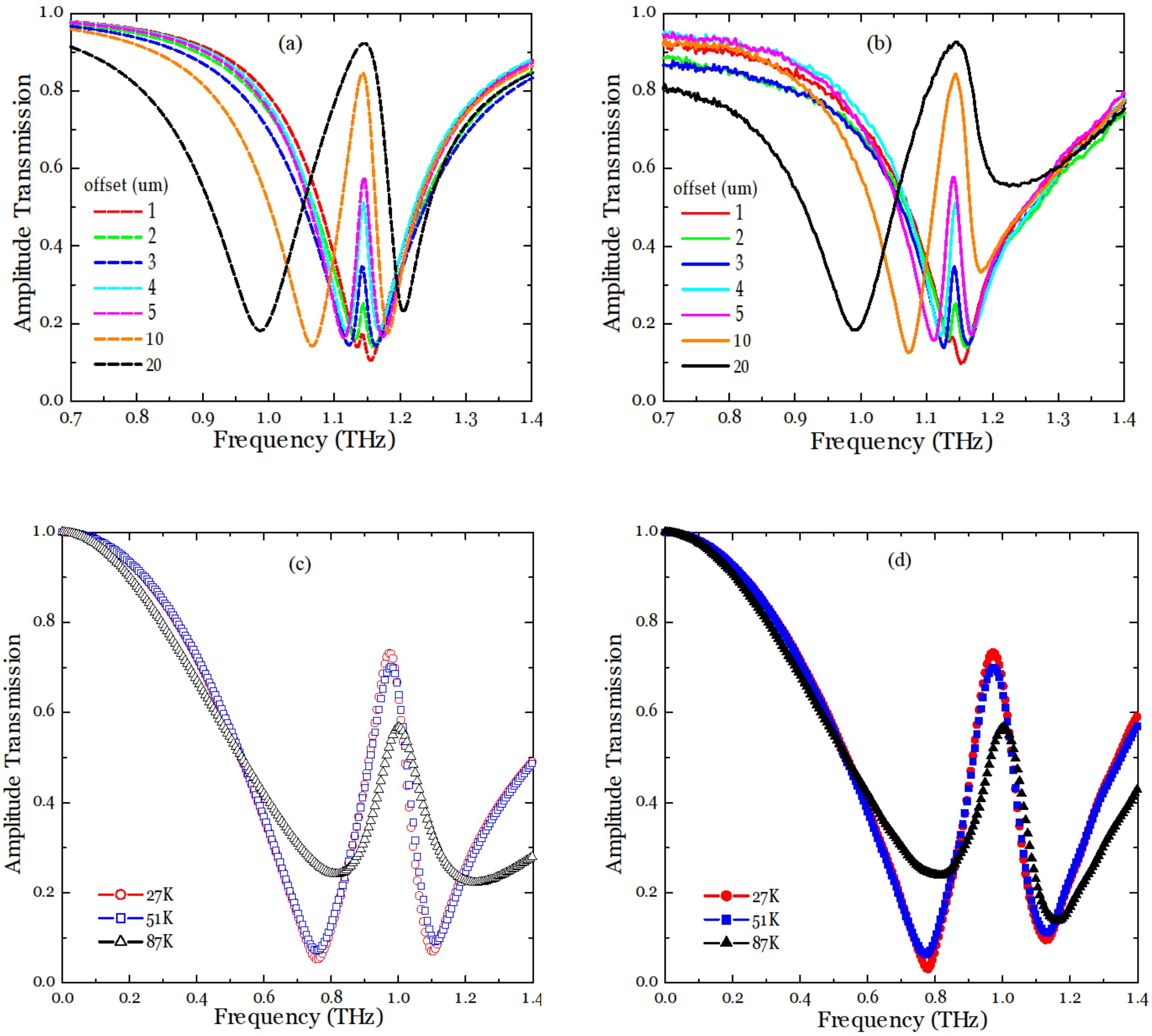

Figure 2-6. Active controls of the transparency window. (a) Theoretical fitting results in terms of Eq. (2-41) under different offsets of symmetry breaking. (b) Corresponding measured normalized amplitude transmission spectra. (c) Theoretical fitting results of the hybrid superconductor-metal metamaterial at different temperatures. (d) Corresponding numerical simulations with different permittivities of the superconductor at different temperature.

Here, we experimentally and numerically demonstrate a thermally active superconductor-metal coupled resonator based hybrid THz metamaterial on a sapphire substrate that shows tunable transparency and slow light behavior as the metamaterial chip is cooled below the high-temperature superconducting phase transition temperature. This metamaterial has the advantage of delivering a thermally active capability of controlling the transparency window and slowing down the THz pulse. Figure 2-6 (c,d) shows the theoretical fitting results and corresponding simulations at different temperatures, respectively.

2.3 Background of surface plasmons

2.3.1 THz plasmonic metamaterials

Surface plasmons (SPs) are known as coherent electron oscillations that exist at the interface between any two materials. Enhanced transmission through subwavelength metallic hole arrays promises a wide range of applications in many important areas. THz plasmonic metamaterial is an exciting and timely new research area. THz radiation, as defined in the frequency range of 0.1-10 THz, has a multitude of desirable attributes. These include a non-ionizing nature, good transmission through many optically opaque materials, and the ability to probe signatures of biochemical molecules and illegal drugs. Thus, THz radiation has extensive applications in a broad range of disciplines, particularly sensing, imaging, and spectroscopy [38-50]. Both electronics and optics are pushing their boundaries into this far-infrared region, thereby offering the promise of future wide-scale development. A difficult hurdle for both approaches is the lack of natural materials that respond favorably to THz radiation. THz plasmonics and metamaterials are promising because they can be specifically designed at will to respond to THz radiation in ways that naturally occurring materials cannot, and could therefore impact broad application areas including civilian and military radar systems, local covert communications, optoelectronics, and THz imaging.

Currently, two challenges in THz plasmonics and metamaterials include: one is finding novel approaches to transition to next-generation THz devices, and the other is overcoming loss mechanisms. The latter presents a fundamental barrier in the available conductivity of metals [51-53]. In terms of the former, remarkable progress has been made in THz generation and detection in the last two decades, but there is a great demand for basic components necessary to manipulate THz waves. THz metamaterial is a timely invention that offers promise here. THz metamaterial based negative index of refraction [54], modulators [55], absorbers [56], invisibility cloaking [57,58], proof-of-concept demonstrations of thin film sensing [59], antennas [60-63], and unique optical activities [64], all herald the development of next-generation THz devices for a broad area of applications, including THz communications, imaging, and spectroscopy. Many of these demonstrations are based on hybrid metamaterial concepts, where tuned electromagnetic properties of the constituents (e.g. silicon) convey additional functionality to the macroscopic metamaterial [65].

2.3.2 Spoof THz plasmons in subwavelength metallic hole array

Subwavelength metallic hole array is a unique way to tailor the wave vector mismatch between the incident photon and SPs by introducing a two-dimensional lattice wave vector. For a regular smooth metallic film the propagation vector of the SP for any direction in plane of the surface is given by [66,67]

$$k_{sp} = k_0 [\frac{\varepsilon_1}{(\varepsilon_{r2}+\varepsilon_1)^2+\varepsilon_{i2}{}^2}]^{1/2} [\frac{\varepsilon_e^2+(\varepsilon_e^4+\varepsilon_1^2\varepsilon_{i2}^2)^{1/2}}{2}]^{1/2}, \tag{2-42}$$

where k_{sp} is the SP wave vector, $k_0=\omega/c=2\pi/\lambda_{\text{resonance}}$ is the free-space wave vector, ε_1 is the dielectric constant of the medium, $\varepsilon_2 = \varepsilon_{r2} + i\varepsilon_{i2}$ is the dielectric constant of the metal, for which ε_{r2} is the real part and ε_{i2} is the imaginary part, and $\varepsilon_e^2 = \varepsilon_{r2}^2 + \varepsilon_{i2}^2 + \varepsilon_1\varepsilon_2$. For example, $\varepsilon_1 = 11.70$ for silicon substrate, or $\varepsilon_1 = 1$ for air free space, for aluminum at 1THz $\varepsilon_{r2} = -3.3 \times 10^4$ and $\varepsilon_{i2} = 6.4 \times 10^5$ [67]. We use a surface Plasmon dispersion appropriate for a smooth film, ignoring in a first approximation the fact that the hole array in the plane may cause both a significant change in the Plasmon dispersion and a large coupling between the front and back surface of the metal film [68]

$$k_{sp} \approx k_0 (\frac{\varepsilon_1\varepsilon_2}{\varepsilon_1+\varepsilon_2})^{1/2}. \tag{2-43}$$

If the values of ε_{r2} and ε_{i2} are very large, the SP wave vector of k_{sp} can be simply approximated by

$$k_{sp} \approx k_0\sqrt{\varepsilon_1}. \tag{2-44}$$

The condition for electromagnetic wave coupling into the SP modes by the array is given by $k_{sp} = k_0 \pm mk_x \pm nk_y$, where k_{sp} is the component of the incident wave vector in the metallic film plane, k_x and k_y are the array momentum wave vectors with $|k_x| = |k_y| = 2\pi/P$, and m and n are integers, P is the hole array periodicity. At normal incidence, $k_0 = 0$, and the free-space wavelengths of the SP modes excited by the array are given by a very good approximation as [67]

$$\lambda_{resonance} = \frac{P}{\sqrt{m^2+n^2}} (\frac{\varepsilon_1\varepsilon_2}{\varepsilon_1+\varepsilon_2})^{1/2}, \tag{2-45a}$$

$$\lambda_{resonance} = \frac{P}{\sqrt{m^2+n^2}}\sqrt{\varepsilon_1}. \qquad (2\text{-}45b)$$

Here, we present that microstructured plasmonic metamaterials combined with nanostructured thin films are designed to explore novel THz devices with unique functionality. The advance in nanofabrication has paved the way to metallic nanostructures with tunable porosity and alignment, which can be integrated into conventional micro-fabrication process. Engineered nanostructures with controlled porosity and morphology could systematically tune the dielectric and polarization properties of metals in the THz regime. The combination of the material control on multiple size scales could be a key enabler. The microscale materials with the nanoscale metallic rod arrays will give us a new opportunity to design and explore novel THz plasmonic devices.

CHAPTER III

BROADBAND TERAHERTZ INVISIBILITY CLOAKING

3.1 Invisibility cloaking strategy

Transformation optics represents the capacity of bending and directing electromagnetic waves in any manner for a certain application. In the pioneering work of J.B. Pendry et al [10,17,18,21], they map the initial configuration of the electromagnetic fields onto a Cartesian mesh, and transform the coordinates of the electromagnetic field to conceal a given object by twisting the Cartesian mesh, namely carpet cloaking. According to this concept, the specification of a ground plane cloak can be determined in the manner described in Ref. 33. A ground plane here means a highly reflective metal surface, which is regarded as a perfect electric conductor. If waves are constrained to a single incidence plane, then the cloak parameters need only to be determined by a two-dimensional plane. The whole configuration is called the physical system with coordinate (x,y) in indexed notation (a rectangle of size $w \times h$). The virtual system is the configuration observer perceives. Its coordinate is labeled by (ξ,η) $(0 \leq \xi \leq w,\ 0 \leq \eta \leq h)$. A coordinate transform between a given rectangle in the virtual system and an arbitrary region in the physical system, as shown in Fig. 3-1.

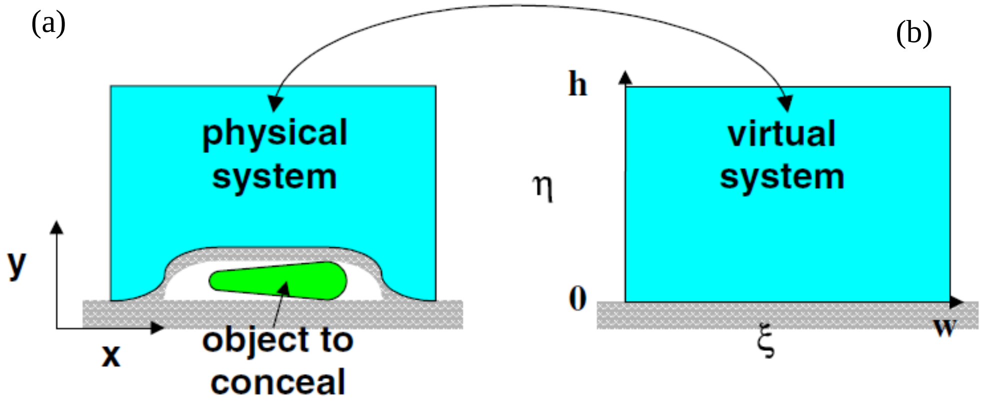

Figure 3-1. The virtual and the physical systems. The regions in cyan are transformed into each other. The regions in grey are the ground planes. The observer perceives the physical system as the virtual one with a flat ground plane [11].

3.2 3D lithographic fabrication of THz cloaks

The permittivity variation of the designed cloak pattern is realized by fabricating effective media consisting of high aspect-ratio subwavelength holes inside a polymer host. Although the pixels on the dynamic mask are presented in the discrete form, the grayscale of individual pixels can be adjusted, as a result the hole's size can be tuned with a sub-pixel level of precision. As illustrated in Fig. 3-2(a), in order to fabricate a square hole with width *d*, the grayscale of each individual pixel can be calculated as grayscale = $p \cdot 256$, where p represents the fraction of area occupied by the polymer for each pixel. Herein, grayscale levels of 0 and 255 correspond to minimum and maximum intensity of each pixel, respectively. Before the cloak fabrication, to confirm real fabricated hole exactly matching with the designed size, a series of holes with various dimensions are designed and fabricated, and then the difference between the mask value and the fabrication value is compared, as shown in Fig. 3-2(b). It is noted that the fabricated size has a larger error when the hole is small. This is due to the diffusion of radicals into the hole region. The resulting dark polymerization results in the reduction in the hole dimension. Such a non-linear relation in the design and fabricated hole dimension are thus calibrated experimentally. By incorporating the calibration into the mask design, Fig. 3-2(c) illustrates that the fabricated hole dimension matches precisely with the designed. The designed grayscale mask of the cloaking and control samples are illustrated in Fig. 3-2(d) and 3-2e, respectively. Inset shows the magnified view of the grayscale mask near the bump.

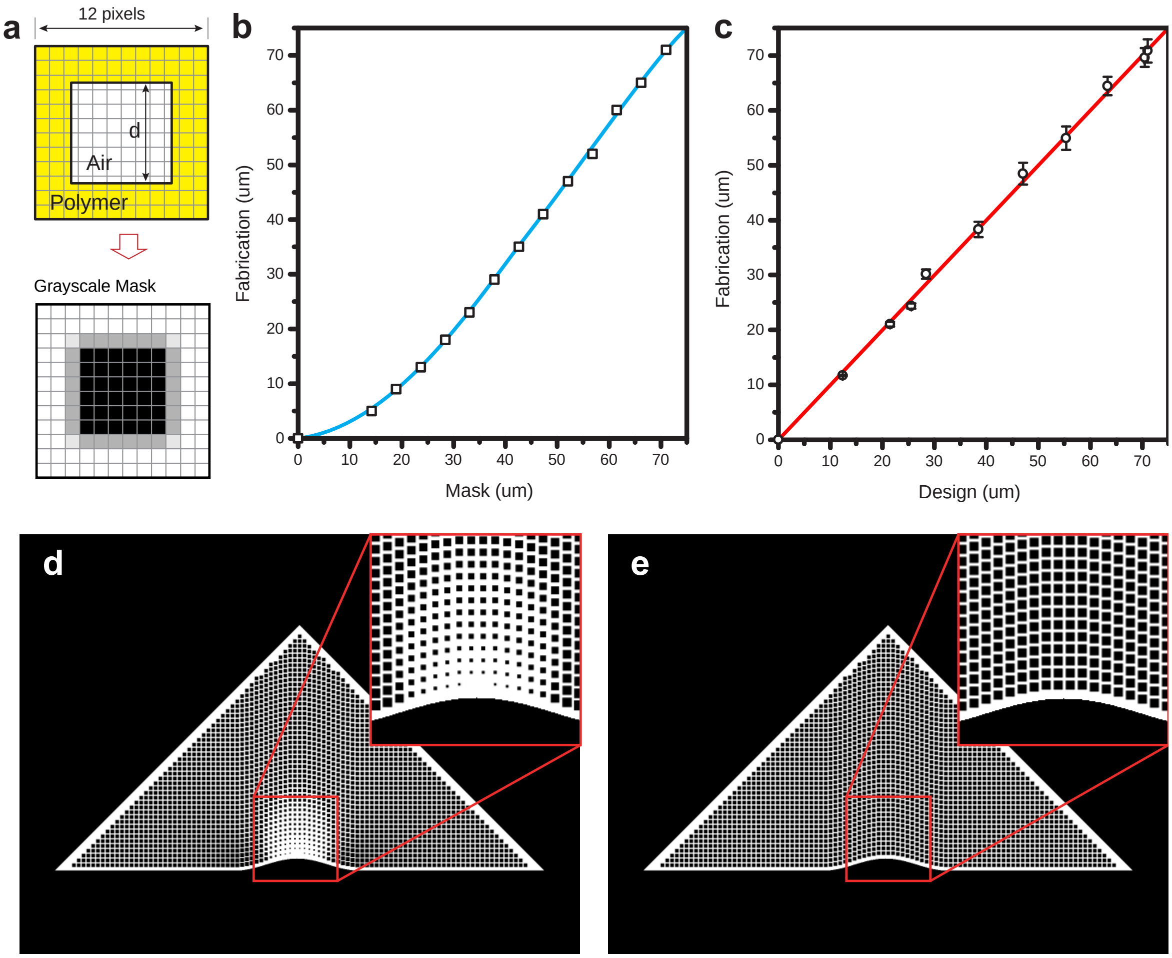

Figure 3-2. (a) the grayscale of individual pixels can be adjusted so the holes can be fabricated with sub-pixel precision; (b) the mask-fabrication relationship before calibration; (c) the design-fabrication relationship after calibration; (d) designed grayscale mask for fabricating cloaked bump structure; (e) grayscale mask for fabricating the uncloaked bump structure.

After the fabrication, the sample is rinsed in isopropyl alcohol for 48 hours to remove the unpolymerized resin inside the holes. It is confirmed by the cross-sectional image of broken sample shown in Fig. 3-3(a). The high-aspect-ratio holes with well-defined geometry can be clearly observed. Furthermore, a special test sample with exposed vertical holes is fabricated to exam the geometry along the vertical direction shown in Fig. 3-3(b). It is clear to see that the hole size changes gradually near the bump and the channel width stays uniform along the vertical direction.

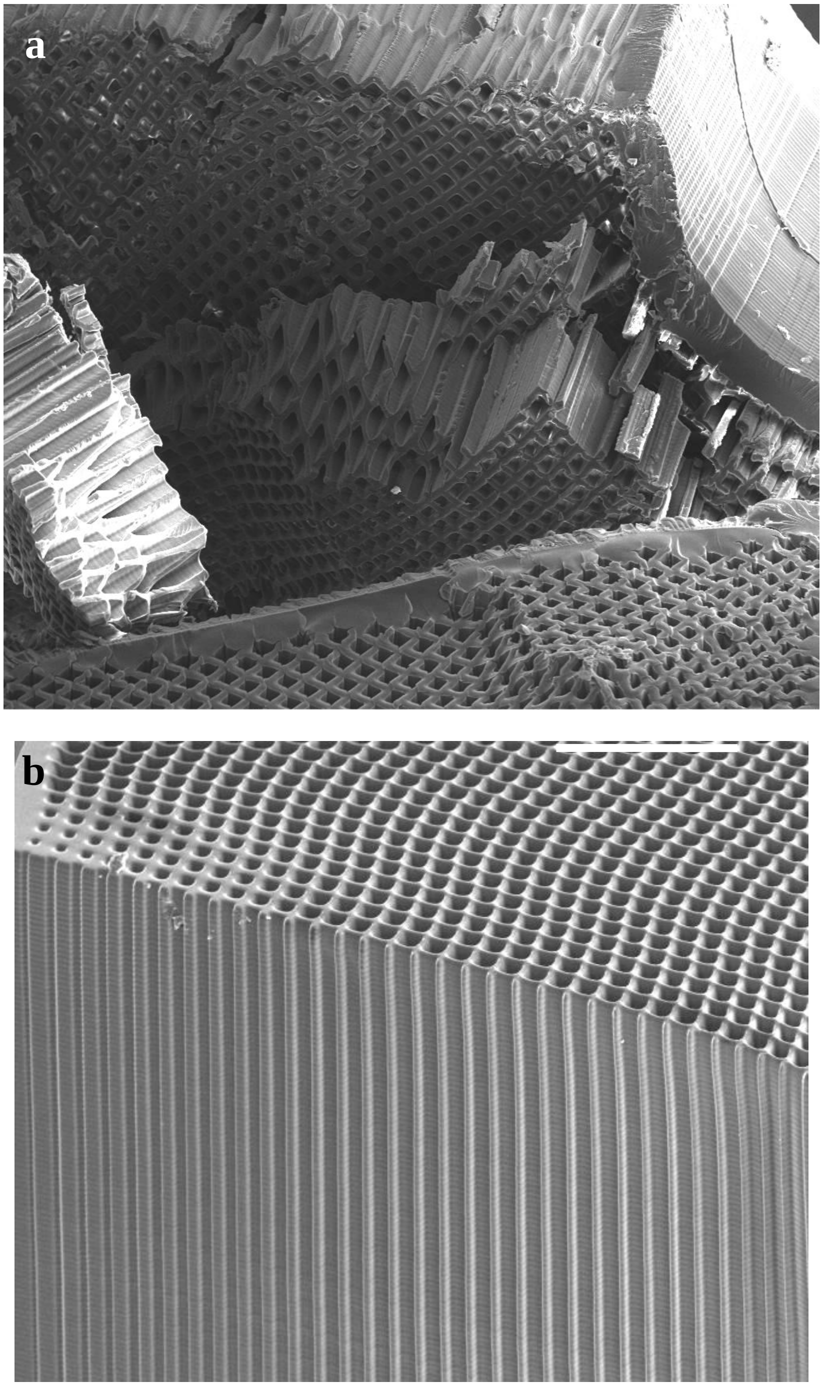

Figure 3-3. (a) Characterization of interior structures of the cloak; (b) Cross-section view of the cloak; bar: 500 μm.

3.3 Fiber-based THz-TDS for characterization of 3D cloaks

A fiber-based THz-TDS, (Fig. 3-4) is employed to assess the performance of the cloaking sample [23,69]. The photoconductive switch-based THz-TDS system is optically gated by 30 fs, 800 nm optical pulses generated from a self-mode-locked Ti:sapphire laser. The THz radiation emitted from a GaAs transmitter is spatially gathered by a hyperhemispherical silicon lens and then collimated into a parallel beam before entering the cloaking sample at a 45 ° incident angle. The reflected THz signal through the sample is then detected by a mobile silicon-on-sapphire (SOS) receiver optically excited with fiber-coupled femtosecond pulses [69].

A 1 mm slit is attached to the SOS detector in order to improve the spatial resolution of the measurements. The detector is placed 50 mm away from the output interface of the sample and horizontally scanned to measure the spatial distribution of the THz wave front. Along the horizontal axis, 51 sets of time-domain signals are measured with a scan step of 0.5 mm. The frequency-dependent THz amplitudes at each spatial position are retrieved by Fourier transform of the measured time-domain signals.

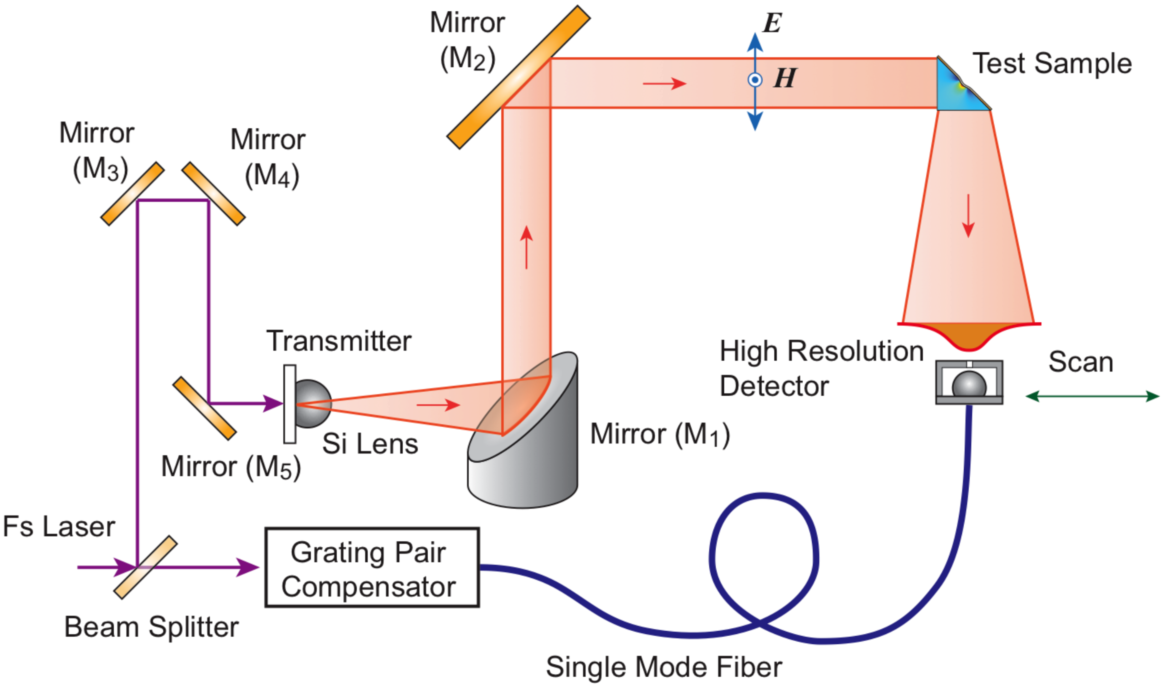

Figure 3-4. Schematic illustration of angular resolved reflection terahertz time-domain spectroscopy system.

3.4 Sample design and simulations

The visual appearance of objects is determined by the extent to which they modify light due to geometric scattering and material absorption. Thus, in order to hide an object from being detected, the invisibility cloak must conceal the changes to the light in both geometry and spectrum. The introduction of transformation optics provides a generalized approach to design the distributions of material constitutive parameters that utilizes the form invariance of Maxwell's equations [9,12].

The initial designs of the cylindrical cloak rely on strong materials dispersion to provide the necessary dielectric singularity without violating physical laws. Thus, the cloaking devices all exhibit high loss and could only be effective at a single wavelength, making them incapable of cloaking in the spectrum domain. To overcome this constraint, the quasiconformal mapping (QCM) technique is used to eliminate the need for the dielectric singularity [13,70] and significantly mitigate the anisotropy of the material, allowing the realization of a broadband invisibility cloak using only isotropic dielectrics. Particularly, a carpet cloak using QCM is proposed to transform one curved reflective surface into a flat sheet, which requires only a moderate variation of the permittivity and permeability. The cloaking region formed underneath the curved surface would be perceived as not even exist. Manually assembling a series of non-resonant elements would be the simplest way to build up such a cloak. Liu et al. first demonstrated the carpet cloak at microwave frequency in 2D form. Thereafter, based on a similar method, Ma et al. designed a 3D cloak operating at microwave wavelengths that was realized by piling up multilayered plates with mechanically drilled inhomogeneous holes with millimeter scale [18].

However, with the scaling down of the working wavelength, such a manual working strategy becomes inapplicable due to the significant reduction of the element size. Thanks to nanofabrication techniques, the carpet cloak successfully decreases in size and is subsequently applied in several experiments at infrared frequencies [15,16]. But these cloaking devices are fabricated using conventional top-down nanofabrication techniques, such as e-beam lithography and focused ion beam milling, which critically constrain the cloak structure in the third dimension. Thus, these cloaking devices are only realized in the 2D waveguide mode. Ergin et al. fabricated the first 3D cloak by direct writing wood pile structures using a commercial system [17], but this point-by-point fabrication process is very time-consuming and costly. Also, strong surface tension forces at such a small scale may easily result in the deformation of 3D structures during the development process. As a result, this 3D carpet cloak is fabricated with fairly small thickness (10 μm) and would be impractical to make on a larger scale. It should also be noted that between the optical and microwave domains, the spectroscopically important THz gap has yet to be explored. Within the THz domain, the specific vibrational, rotational, and translational responses of materials carry unique molecular signatures that are generally absent in optical, microwave, and X-ray frequencies [20,45].

The lack of methods to manipulate the THz waves is a great impediment for the development of functional THz-based elements such as lenses, modulators, reflectors, and beam shifters, which have potential use in quality control, biomedical imaging, disease detection, sensing, and communications. By applying transformation optics, it is possible to explore new functional devices to manipulate the propagation of THz beams at will and examine its spectroscopic properties with high efficiency, low cost, and low complexity. Among them, cloaking of realistic objects under THz is a representative example and is inspiring rapidly increasing interest. However, the requirement of high aspect ratio microscale features in a macroscopic structure proves to be a challenge. For this cloak fabrication, the UV curable resin consists of 1,6-Hexanediol diacrylate (HDDA) as the low viscosity monomer and Irgacure 819 as the photoinitiator. Moreover, a critical amount of UV absorber has been mixed with the UV curable resin to control the curing depth. After the fabrication, the sample is rinsed in isopropyl alcohol for 48 hours to remove the remaining polymer inside the holes.

In this chapter, we present an experimental demonstration of a broadband THz cloaking device that can be placed over a realistic 3D object to conceal its geometrical and spectroscopic features. The refractive index distribution in the *x*-*y* triangle-shaped plane is obtained using QCM for transverse magnetic (TM) waves [70]. A series of discrete elements is used to approximate the continuous refractive index profile under the effective media theory. A triangle-shaped carpet cloak is designed with a width of 8,520 μm and height of 4,260 μm. The bump located at the bottom side is defined by a cosine function with a height of 213 μm and a width of 4,260 μm, $y = 106.5cos2\pi[(x - 2130)/4260] + 106.5$. After conformal mapping, the permittivity of the ground-plane cloak is found in the range of 1.02 to 2.86 with a corresponding background of permittivity $\varepsilon_{\mathrm{ref}}$=1.47 ($n_{\mathrm{ref}}$=1.21). The calculated anisotropic parameter is 1.04, thus the cloak pattern can be treated as an isotropic medium. Under effective media approximation, the permittivity distribution can be realized by creating sub-wavelength holes of variable sizes inside the polymer host. For TM waves, the filling ratio of air holes f can be calculated using the effective media theory:

$$f = \frac{e_d/e_{eff}-1}{e_d/e_{air}-1}, \tag{3-7}$$

where $\varepsilon_{\mathrm{eff}}$ is the effective permittivity of the cloak pattern, $\varepsilon_{\mathrm{air}}$ and ε_{d} are the permittivity of air and the host polymer materials, respectively. Using a unit cell size of 85.2 μm (12 pixels), the corresponding hole size ranges from 10 μm to 71 μm. The design is extruded along the *z* axis to form the 3D cloaking structure as shown in Fig. 3-5(a). The characteristic of such a cloak design consisting of microscopic hole structures is evaluated using numerical simulation for a bumped surface without and with a cloak, as shown in Fig. 3-5(b) and 3-5(c), respectively. The simulation shows the magnetic field component in the z direction at 0.6 THz. The THz wave reflected from the uncloaked bump exhibits two distinct peaks and one minor peak in between. In contrast, the reflection from the cloaked bump shows the expected flat wavefront, as if the bump does not exist. Thus, the object placed underneath the reflective bump can be cloaked.

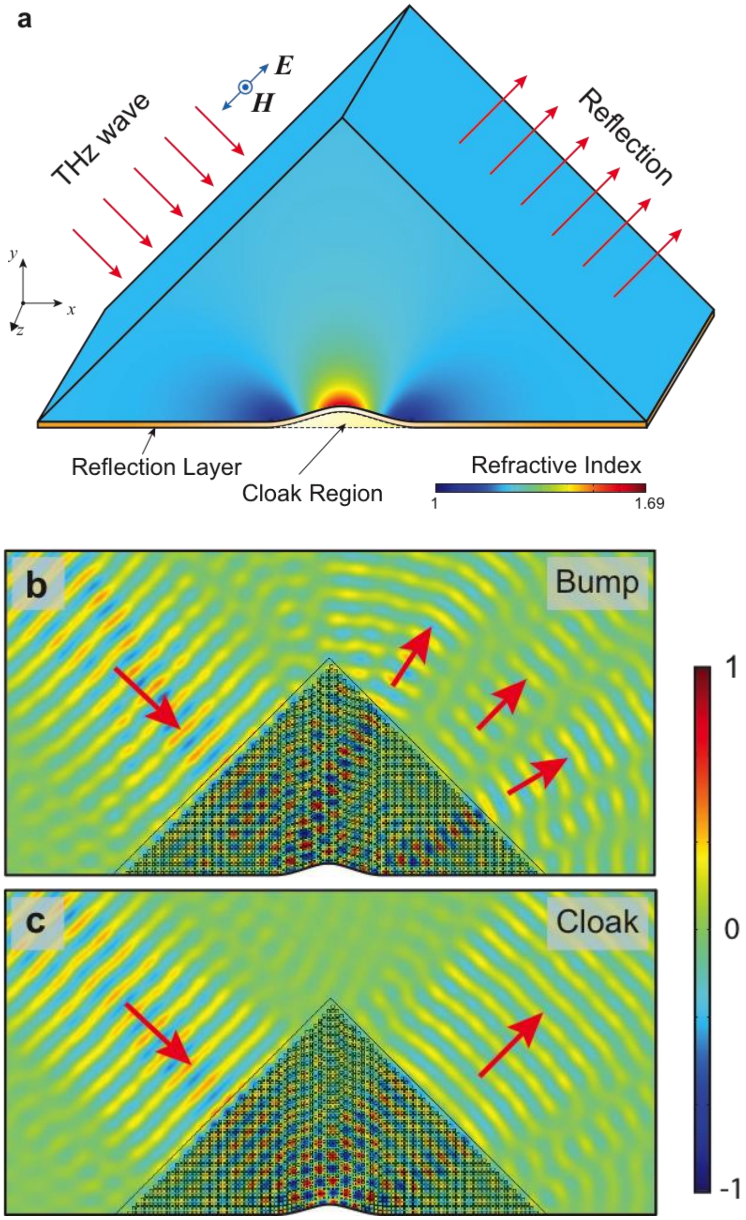

Figure 3-5. Design and simulations of 3D THz cloak. (a) The triangle-shaped cloak structure is obtained by extruding the refractive index profile in the *x*-*y* plane along the *z*-axis. (b) Numerical simulation using commercial software (COMSOL Multiphysics) confirms the splitting of the wave into three waves for the bump structure with uniform refractive index. (c) The cloak structure preserves the original shape of the incoming wave. The simulation results show the normalized magnetic field component in the *z* direction at 0.6 THz.

A highly scalable and parallel 3D microfabrication technique is employed, named projection micro-stereo-lithography (PμSL), for fabrication of the 3D cloaking device [71]. In contrast to fabricating the 3D structure in a point-by-point scanning fashion, PμSL uses a high resolution dynamic mask containing 1,470,000 (1,400 ×1,050) pixels, to fabricate a whole 2D pattern in a single exposure as shown in Fig. 3-6(a). The desired permittivity profile is obtained by using sub-wavelength unit cells containing cylindrical holes with varying dimension under effective media approximation. In this work, the unit cell has a width of 85.2 μm (~12 pixels) in the *x*-*y* plane and 20 μm in the *z* direction, which is much smaller than the vacuum wavelength of 500 μm at 0.6 THz. Although the pixels on the dynamic mask are presented in the discrete form, tuning the intensity of individual pixels at 256 grayscale levels allows the fabrication of holes with sub-pixel scale dimensional accuracy. It is then possible to create the desired refractive index distribution with smoother transitions in space to minimize the scattering of the THz wave. The designed mask pattern in a digitized form is used for constructing the 3D cloaking structure in a layer-by-layer fashion. In analog to the natural crystals formed by the 3D assembly of atoms, the cloaking structure is constructed from bottom up to form the assembly of unit cells in 3D with varying effective permittivity. As shown in Fig. 3-6(b), the fabricated triangular cloaking structure has a total thickness of 4.4 mm, comprised of 220 layers of 20 μm thickness. The distribution of the varying hole geometry can be clearly identified in the scanning electron microscope (SEM) images shown in Fig. 3-6(b). Finally, a 200 nm-thick gold layer is deposited on the bottom to form a reflective surface. The space underneath the bump is designated as the cloaked region.

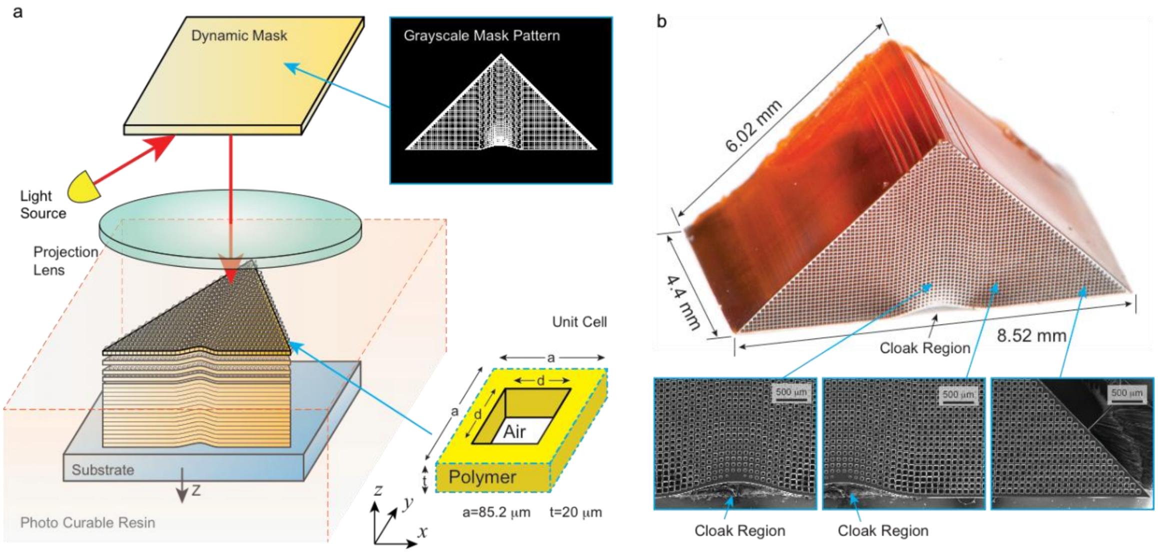

Figure 3-6. Fabrication and characterization of 3D THz cloak. (a) Schematic diagram illustrating projection micro-stereolithography system being used to fabricate 3D cloaking device. The grayscale of individual pixels within each 85.2 x 85.2 μm unit cell can be adjusted so the holes can be fabricated with sub-pixel precision. (b) Optical and SEM images of the fabricated cloaking device. The surface of the device is metalized to enhance the contrast for better representation of the fine features in the images. The gradual change in hole size near the bump can be clearly observed.

3.5 THz-TDS experimental measurements

The THz absorption coefficient of α-lactose monohydrate (Sigma-Aldrich) is measured using a transmission THz-TDS system. 2 mm-thick pure α-lactose monohydrate powder is sandwiched between two 640 μm thick silicon slabs. A silicon-air-silicon stack with 2 mm air gap was used as a reference. $E_{reference}(\omega)$ and $E_{sample}(\omega)$ represent the Fourier-transformed spectra of the transmitted terahertz pulses through the reference and the sample, respectively. The absorption coefficient of the sample powder is extracted based on the transmitted pulses. The complex transmission spectra of the reference $E_{reference}(\omega)$ and the sample $E_{sample}(\omega)$ are given by

$$E_{reference}(\omega) = E_{incidence(\omega)} t_{Si-air} t_{air-Si} \exp(ik_0 d), \tag{3-8}$$

$$E_{sample}(\omega) = E_{in}(\omega) t_{Si-sample} t_{sample-Si} \exp(ikd) \exp(-\alpha d/2), \tag{3-9}$$

where $E_{incident}(\omega)$ is the incident pulse spectrum, $k_0 = 2\pi/\lambda_0$ and $k = 2\pi n_{sample}/\lambda_0$ are the wave vectors for air and sample, respectively; n_{sample} is the refractive index of the sample, d is the sample thickness, λ_0 is the free-space wavelength, and α is the absorption coefficient of the sample; t_{Si-air}, t_{air-Si}, $t_{Si-sample}$, and $t_{sample-Si}$ are the Fresnel transmission coefficients of the THz pulses propagating through silicon-air, air-silicon, silicon-sample, and sample-silicon interfaces, respectively, which are given by $t_{Si-air} = 2n_{Si}/(1+n_{Si})$, $t_{air-Si} = 2/(1+n_{Si})$, $t_{Si-sample} = 2n_{Si}/(n_{Si}+n_{Sample})$, and $t_{sample-Si} = 2n_{sample}/(n_{sample}+n_{Si})$. The $t_{Si-sample}$, and $t_{sample-Si}$ are the complex, frequency-dependent coefficients related to this powder layer sample. The measured absorption coefficient is shown in Fig. 3-7. Strong absorption peaks at 0.53 THz and 1.37 THz are observed, which is in good agreement with literature [72].

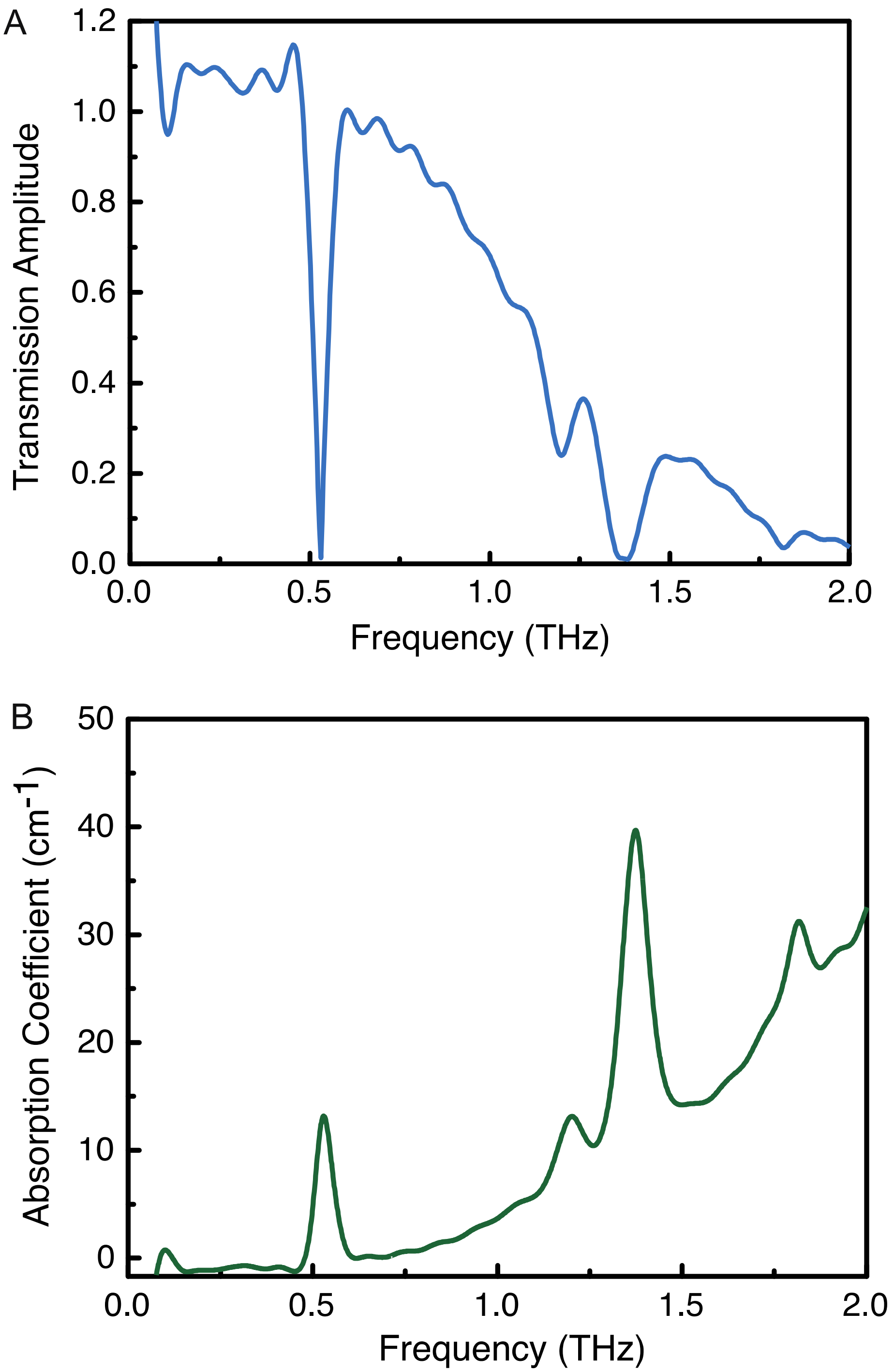

Figure 3-7. Measured power absorption coefficient of the α-lactose monohydrate powder

In this experiment, the test sample is made of α-lactose monohydrate, which exhibits a resonant attenuation signature at 0.53 THz due to the presence of collective vibrational transition modes [72]. The α-lactose monohydrate powder (Sigma-Aldrich) is pressed into a thin rectangular shape (1 mm × 0.12 mm × 4 mm) on a reflective substrate, such that it can fit under the bump. The measurement of the reflected THz wave is performed over a broad frequency range of 0.3-0.6 THz on a set of four cases shown in Fig. 3-8: (a) flat reflective surface, (b) exposed lactose on reflective surface, (c) control structure with reflective bump placed on top of the lactose, and (d) the cloaking structure placed on top of the lactose.

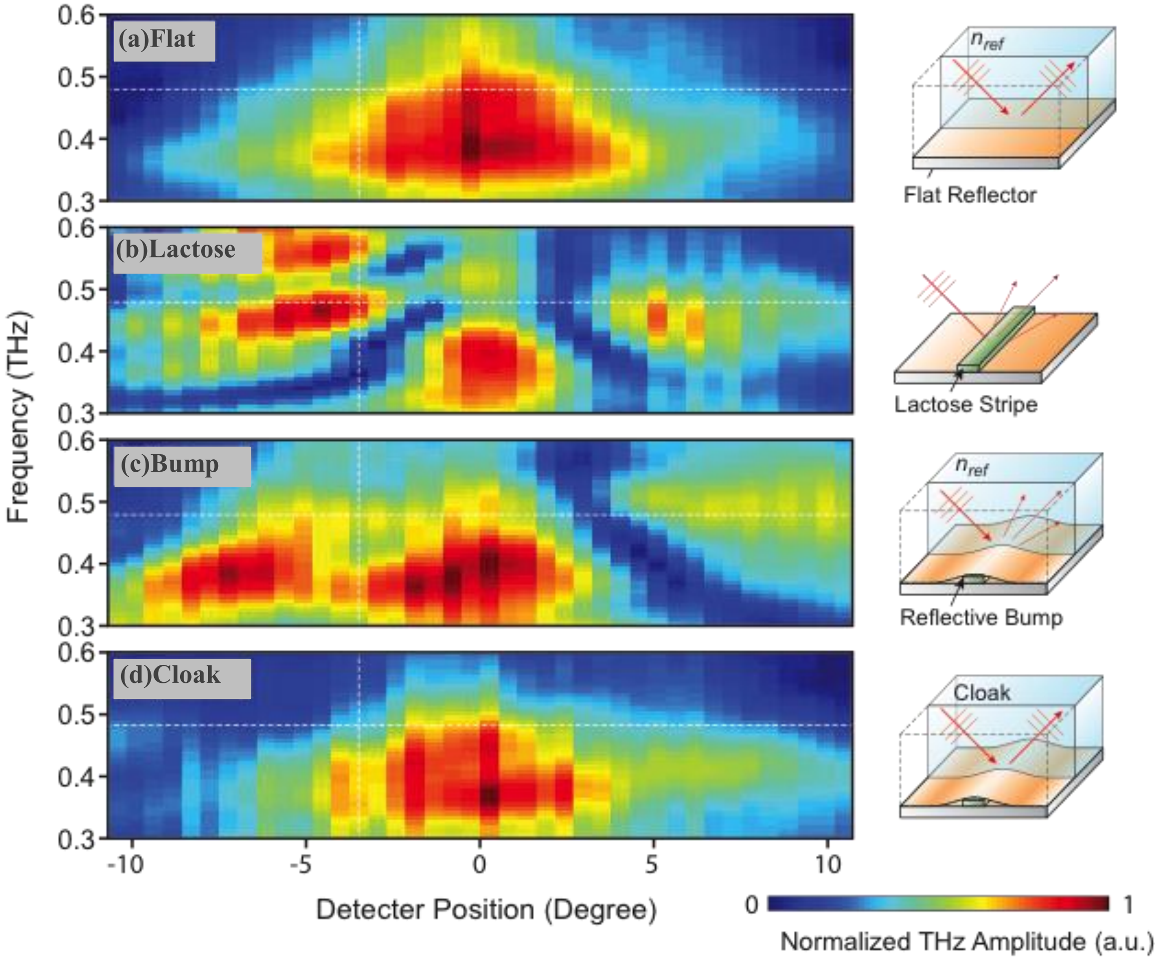

Figure 3-8. Spectra maps of four experimental cases. (a) reflective flat, (b) exposed α-lactose monohydrate, (c) reflective bump, and (d) cloak, are measured using reflection terahertz time-domain spectroscopy. The lactose (b) shows both a scattering effect and absorption. The reflective bump (c) avoids the absorption effect, but is still split into three peaks. The measured spot position of the cloak (d) and the reflective flat (a) match reasonably well with each other.

As shown in Fig. 3-8, the horizontal and vertical axes represent angular positions and frequency, respectively, while the color represents the normalized amplitude of the THz wave. In case (a), the THz wave incident at 45 ° is reflected from the gold-coated flat surface. The half-space above the reflective bump has an effective refractive index n_{ref}. The measured reflected beam is clearly confined in both frequency and space, as the characteristic of a collimated THz beam. In case (b), the reflected beam is split into three peaks due to the geometrical scattering caused by the lactose. In addition, a narrow dip is observed at 0.53 THz, which is coincident with the absorption signature unique to α-lactose monohydrate. To prevent the lactose from being detected, it is possible to hide it under a reflective bump, as shown in case (c). Shielding the lactose from the THz wave causes the spectroscopic signature at 0.53 THz to disappear. However, the reflected THz wave exhibits three peaks, indicating unsuccessful cloaking due to the effect of geometric scattering off the bump. In contrast, the THz cloak shown in case (d) conceals both the geometric and spectroscopic features of the lactose, which closely resembles the case (a) as a flat reflective surface. In order to better illustrate the differences, the measured THz amplitude at 0.48 THz for the aforementioned four cases is shown in Fig. 3-9(a). The cloak and flat surface plots resemble each other very closely with a single central peak, whereas the graphs for the exposed lactose and reflective bump exhibit two additional side peaks (red and green arrows). Figure 3-9(b) plots the amplitude as a function of frequency at a detector position of -3 degrees. The 0.53 THz absorption dip (red arrow) observed in the exposed lactose case is not present in the cloak case, which again is similar to the flat reflective surface. These results demonstrate that the fabricated THz invisibility cloak has successfully concealed both the geometrical features and spectroscopic signatures of the α-lactose monohydrate structure.

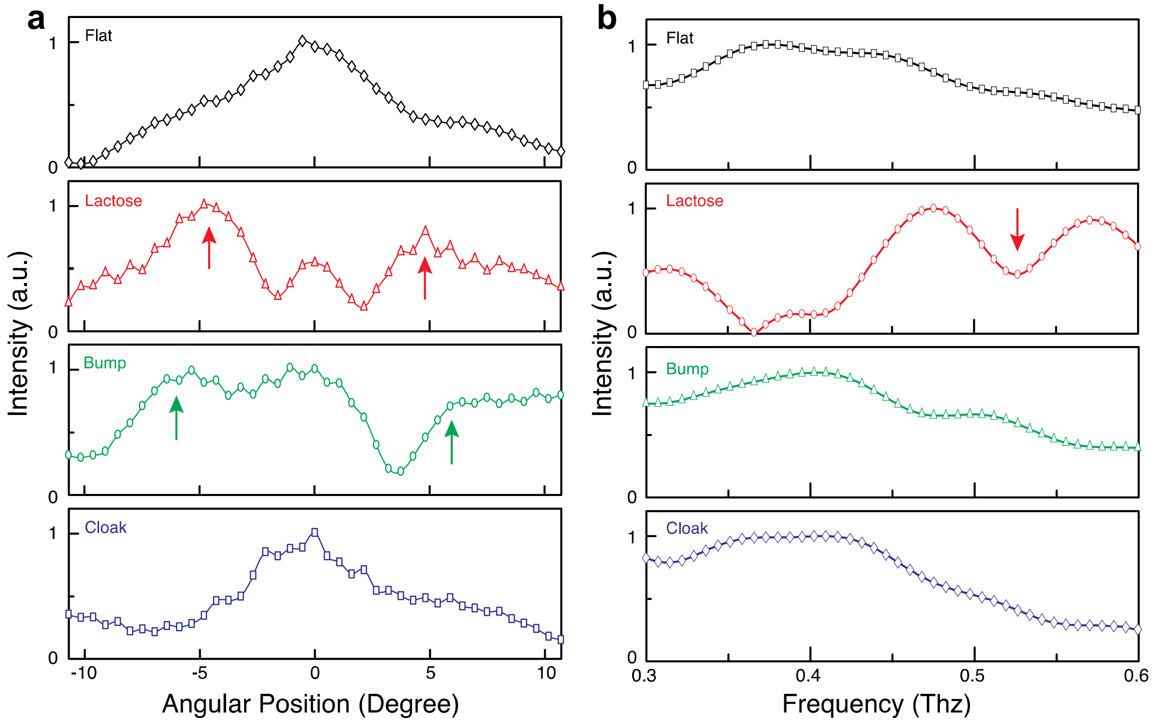

Figure 3-9. Cross-sectional plots of experimental results (a) Intensity as function of detector position for four cases at 0.48 THz. The cloak and reflective flat have one similar peak, whereas the lactose and reflective bump exhibit two extra peaks (red and green arrows). (b) Intensity as function of frequency for four cases at -3 degrees (angle). Obvious absorption occurs at 0.53 THz for the exposed lactose (red arrow).

3.6 Summary

The cloak is designed as a 3D solid model. By slicing of the 3D solid model, each 2D slice is displayed on the dynamic mask as a bitmap image. The carpet cloak works for the incident angle within the half space of a plane. However, the carpet cloak does not require extreme values for the transformed material properties. The anisotropy of the cloak material can be significantly mitigated by applying the QCM technique. Consequently, it allows only isotropic dielectrics to construct the carpet cloak, realizing a broadband invisibility cloak and practically scalable to operate in THz regime. This work not only reports the experimental demonstration of hiding a realistic 3D object from THz waves, but more importantly, metamaterials offer a technical feasible solution for designing and fabricating THz invisibility cloak using isotropic dielectric materials by drilling inhomogeneous holes. In contrast to the conventional optical methods, the ability to manipulate THz wave propagation using transformational optics will undoubtedly initiate new possibilities for a variety of intriguing THz applications with unprecedented functionalities.

CHAPTER IV

TRANSFORMED LUNEBURG LENS FOR TERAHERTZ IMAGING

4.1 Introduction

Nowadays, the needs of high quality imaging impose ever-increasing demands on efficient manipulation of light in order to enable superior resolving power without introducing aberration [73-77]. With a single objective lens capable of delivering aberration-free imaging, it could move away from aberration compensation methods of complex optical assemblies, which are pervasive in optics technology from classic microscopes to emerging THz imaging, and towards truly eliminating image distortion with single lens systems [78,79]. In general, the difficulty optical designers have had in accomplishing aberration-free imaging has been with the need to maintain superior resolving power, meaning the need to also be able to manipulate the light at large incident angles. Achieving both attributes with a homogeneous lens has been shown not possible due to the lens intrinsic fixed permittivity. The current optics design that relies on finite number of refractive and/or reflective surfaces cannot fully eliminate geometric aberrations without possessing another degree of freedom [80]. From this reasoning, researchers have theorized about ways to introduce this additional design parameter within a lens, which of the most promising is a spatially varying refractive index [81-84].

4.2 Sample design

While many solutions, such as spherical Luneburg lens, have emerged from this idea with respect to perfect point-size imaging, scientists remain left with no practical solution on aberration-free imaging of the most common application, a planar field of view.

The conventional spherical lens with uniform index is surrounded by air. It is noticed that whenever the light incidents normally or obliquely obvious aberrations occur at the focal plane. The spherical Luneburg lens has the index gradient along the radial direction $n(r) = \sqrt{2 - {r^2}/{R^2}}$ and it perfectly focuses light from any direction to points on the surface of the lens. Based on the idea of spherical Luneburg lens, a transformed flattened Luneburg lens is designed for more practical applications. The refractive index distribution and simulation result of three types of lenses are shown in Fig. 4-1.

In Figs. 4-1(h, i), the simulations illustrate that refractive index distribution of flattened Luneburg lens has excellent focusing characteristic since the plane wavefronts coming from any direction propagating through the lens can be perfectly focused to a point on the opposite side of the planar area. Clearly, the simulations prove our design that the flattened Luneburg lens does indeed have a more desirable planar focal plane for imaging application, while preserving the unique aberration-free characteristic of the original Luneburg lens design.

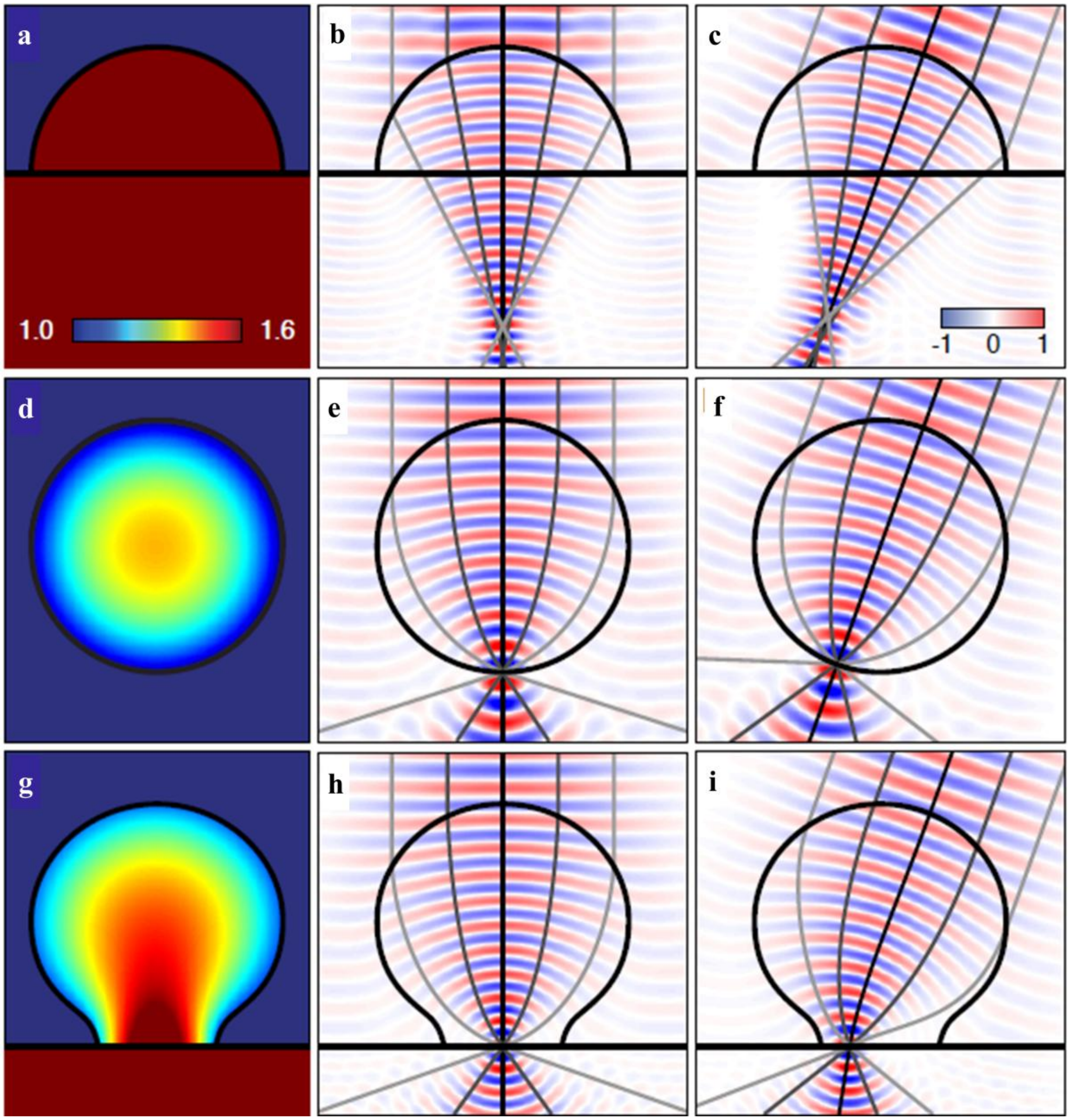

Figure 4-1. The comparison of the conventional spherical lens, spherical Luneburg lens, and flattened Luneburg lens. (a, d, g) The refractive index distribution of the conventional spherical lens, spherical Luneburg lens, and flattened Luneburg lens, respectively. (b-i) Performance of plane wavefronts from different directions propagating through the three lenses.

4.3 Sample fabrication

In order to design the flattened Luneburg lens, starting from the original spherical Luneburg lens, as shown in Fig. 4-2, transformation optics theory is employed to further tailor the light in three dimensions (3D) [85-88]. In this design, the angle θ is set as 82.8 degree. The red bold curve shown in Fig. 4-2 will be transformed into a straight line. The transformation is based on the QCM to transform a portion of the lens spherical focal plane into a flattened one, of which the practicality for a physical lens has been demonstrated as a collimation lens at microwave frequencies [18,89,90]. By performing QCM, the refractive index is ranging from 0.451 to 1.719. The red straight line of 2.645 mm in length represents the flattened focal plane of the transformed Luneburg lens. For the practical consideration of the realistic material properties, the range of the calculated refractive index is truncated with the reduced range between 1.1 and 1.637, as illustrated in Fig. 4-2(b). Figures 4-2(c) and (d) compare the mesh deformation before and after transformation, in which dense grid represents high index region while coarse grid means low index region. With a point source at the focal plane, the transformed Luneburg lens will convert the omnidirectional emission into a collimated beam, or in other words, change the spherical wavefronts to the plane wavefronts.

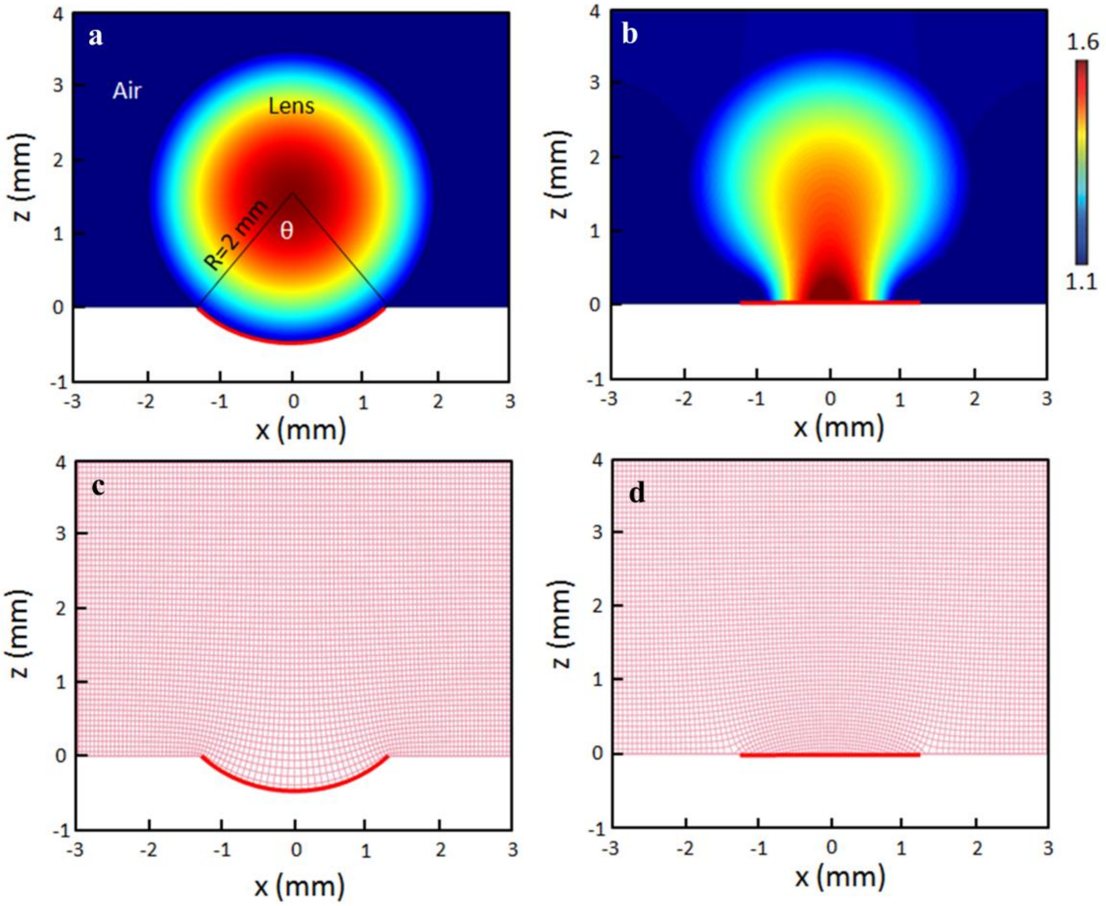

Figure. 4-2. Transformation of 2D flattened Luneburg lens compressing a spherical focal plane into a flat one. The scale bar shows the index range. (a,c) The gradient index distribution of the spherical Luneburg lens and meshing grid, respectively; (b,d) The gradient index distribution of the flattened Luneburg lens and meshing grid, respectively.

To construct the 3D lens, the two-dimensional (2D) refractive index profile is rotated around the *z*-axis shown in Fig. 4-3. The required spatially varying refractive index of the lens is realized by using a polarization-independent unit cell under effective medium approximation. In Fig. 4-3(a), the 3D lens is fabricated out of photopolymer material using PμSL [71]. This fabrication process is favorable since it allows for a high-resolution dynamic mask (1400×1050) to be used in order to construct the 3D lens by means of stacking a series of 2D patterns in a layer-by-layer fashion. The unit cell consists of two orthogonal polymer rods (side length of 85.2 μm and thickness of 42.6 μm), generally referred to as a woodpile structure, whose dimensions are much smaller than the wavelength of 500 μm at 0.6 THz. Thus, such metamaterial geometry leads to nearly isotropic optical. The local refractive index is tuned by subtly varying the polymer high-aspect-ratio of each unit cell, in which the refractive index is 1.637 for the bulk polymer and 1.00 for the air void, respectively. It should be noted that although the dynamic mask used for PμSL fabrication is of discrete pixels, the intensity of the individual pixels can be further tuned within the 256 grayscale range, yielding polymer rods with sub-pixel scale dimensional accuracy. By slicing of the 3D solid model, each 2D slice is displayed on the dynamic mask as a bitmap image. The high-resolution optical image is then projected on the top surface of the photo-curable polymer resin and subsequently solidified, forming a thin polymer layer with the desired shape. Using a computer to synchronize the vertical motion of the sample stage and a slow move of the sequential 2D slices on the dynamic mask, the 3D structure can be rapidly constructed. The exposure time for each layer is a few seconds, allowing fabrication of the 100-layer 3D structure shown in Fig. 4-3(a) in less than an hour. For the sample fabrication, the UV curable resin consists of HDDA as the low viscosity monomer and Irgacure 819 as the photoinitiator. Moreover, a critical amount of UV absorber has been mixed with the UV curable resin to control the curing depth. After the fabrication, the sample was rinsed in isopropyl alcohol for 48 hours to remove the remaining polymer.

Therefore with this fabrication process, it is able to create the desired refractive index distribution with smoother transitions in space in order to minimize the scattering of the THz wave. Here, the result is a transformed Luneburg lens, as shown in Fig. 4-3(a), which has a total thickness of 4.27 mm and is comprised of 100 layers of polymer rod array with uniform thickness. Looking closer with the SEM inset in Fig. 4-3(a), it is clearly observed that the woodpile structure is well defined. Thus with this precise 3D manufacturing, the cross-sectional view illustrates the effective transformation of the spatial variation of polymer high-aspect-ratio to the refractive index distribution in Fig. 4-3(b).

A fiber-based angular-resolved THz-TDS system is employed to quantify the imaging performance of the transformed Luneburg lens. The detector is placed 20 mm away from the output interface of the imaging sample and scanned in two-dimensional space to measure the spatial distribution of the transmitted THz wave front at the far-field, as shown in Fig. 4-3(c). The frequency-dependent THz amplitudes at each spatial position are then retrieved via Fourier transform of the measured time-domain signals.

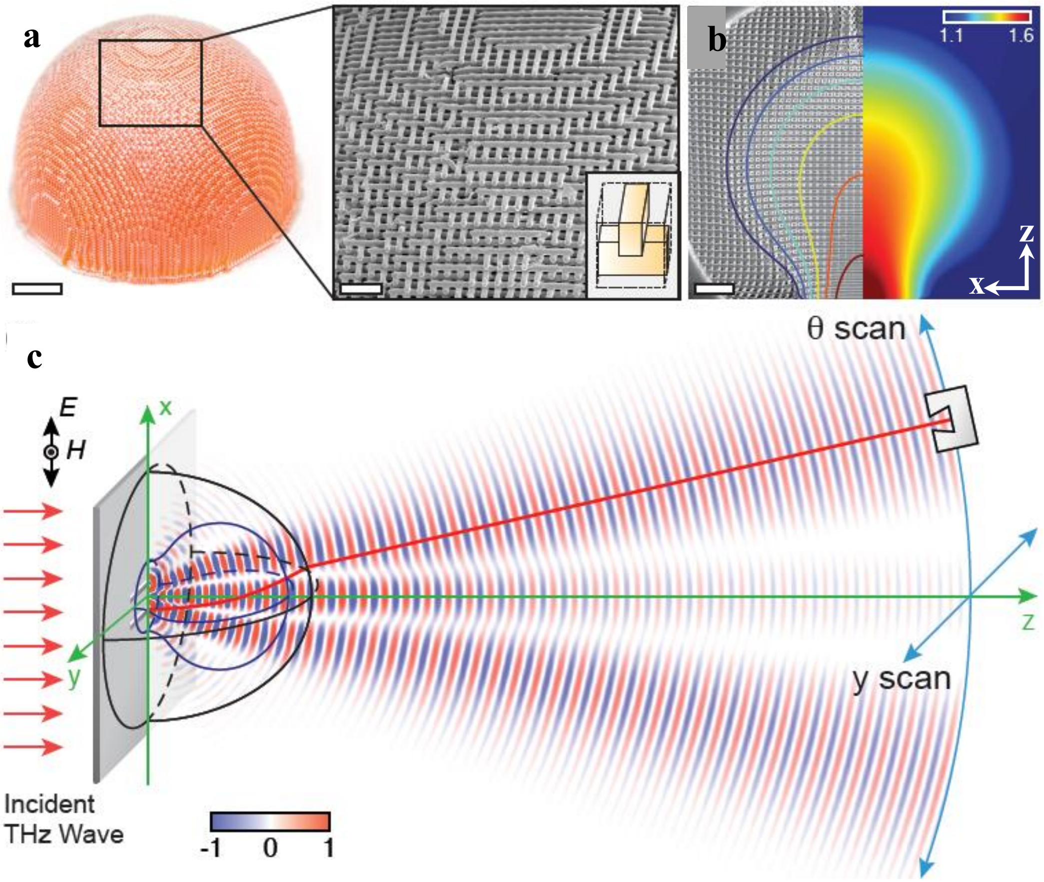

Figure. 4-3. 3D THz transformed Luneburg lens. (a) The fabricated lens is made of 100 layers of polymeric "woodpile" structure. Bar: 1 mm. Each unit cell has a cubic shape with side length of 85.2 μm. It consists two orthogonal polymer bars and each bar is 42.6 μm thick. By changing the width of the polymer bars, one can precisely control the volume ratio of polymer to air in each unit cell, such that the refractive index can be tuned in the desired manner. (b) Cross-section view shows the varied dense of "woodpiles", which well represents the gradually changed index distribution shown in the right half of the figure. Bar: 500 μm. (c) Schematic of imaging double-slit object with a transformed Luneburg lens. At far field, detector moves along the circle in *x*-*z* plane and along straight line in *y*-*z* plane to scan THz signals.

4.4 Measurements and analysis

4.4.1 Evaluation of the bending angle versus the source location

For the first test, the isotropic optical properties of the fabricated transformed Luneburg lens is evaluated by examining the coupling beam bending angle versus the source location at the focal plane. A single slit with width of 200 μm is placed at the focal plane of the transformed Luneburg lens to form a line source. By gradually shifting the slit to different off-center locations ranging from 0 to 50 μm, the transmitted wave can be detected at corresponding angular distributions. The bending angle is defined as the deviation of the THz wavefront relative to the bottom center of the transformed Luneburg lens. Figure 4-4 shows the comparison of experimental results with simulations at the representative frequency of 0.5 THz for five cases at different locations. The horizontal and vertical axes represent angular positions and frequencies, respectively, while the color represents the normalized amplitude of the THz wave. When the line source is placed at the center of the focal plane shown in Fig. 4-4(a), the measurement result illustrates that the THz wave propagates through the transformed Luneburg lens without bending and shows a nearly planar wave front at the far field, with a broadband frequency ranging from 0.4 to 0.6 THz. The bending angle increases nearly linearly as the line source deviates from the center. When the line source moves as far as 500 μm away from the center in Fig. 4-4(f), the bending angle reaches approximately 21.2 degrees. The widths at the half height of the each measured peak, which represent the width of line source, are all approximately 10 degrees. The shift of bending beam is in well agreement with the simulation results (solid white lines) and shows a nearly linear behavior with respect to the off-center location. Moreover, Fig. 4-4 (g-i) indicate that the THz beams bend with an exactly same angle in a broadband from 0.4 to 0.6 THz as the line source locates at an arbitrary position on the focal plane. Consequently, these demonstrate the fabricated transformed Luneburg lens could be used as a high-performance imaging lens without aberration as our expectation.

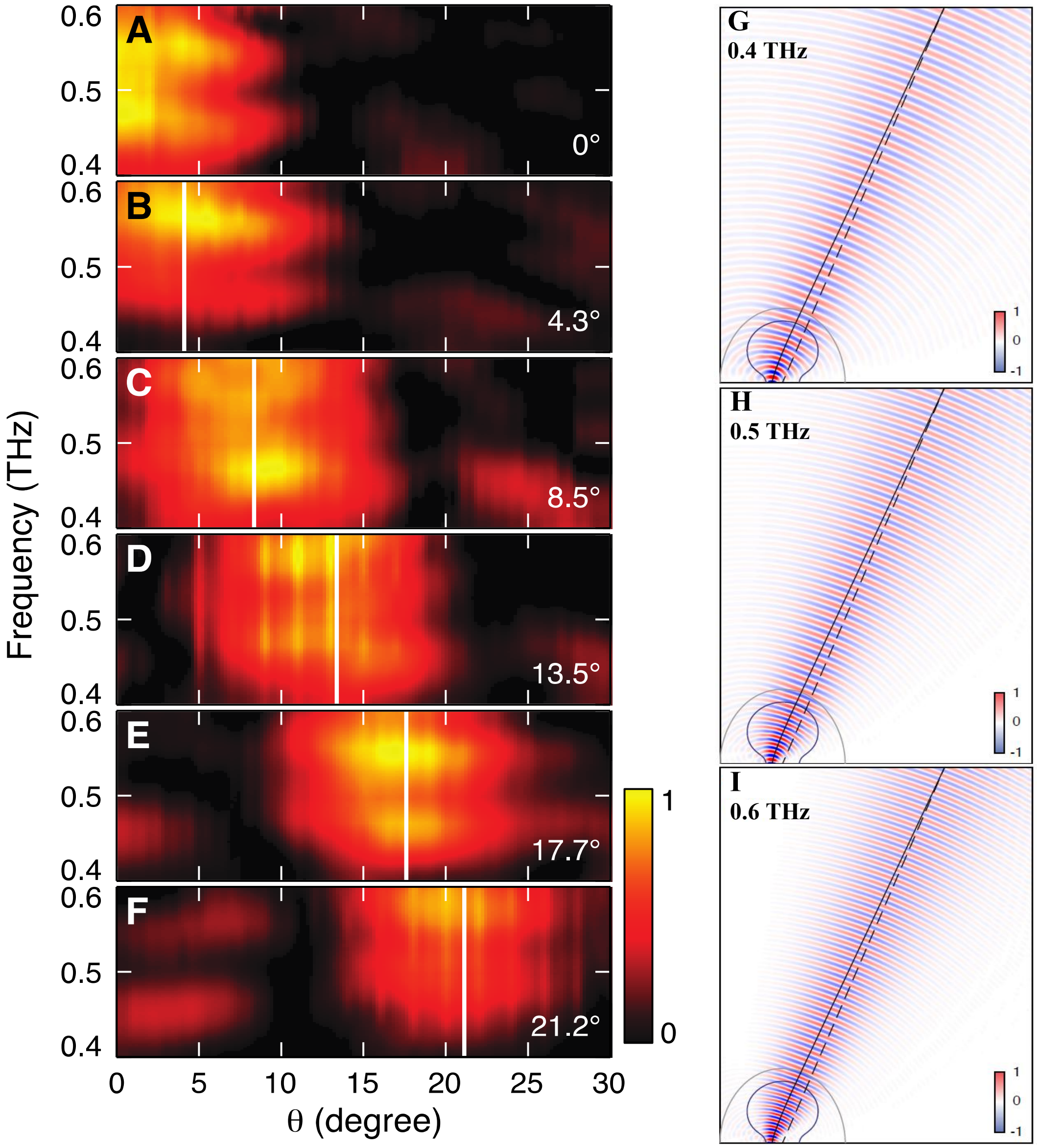

Figure 4-4. Performance tests of transformed Luneburg lens. (a-f) Experimental spectra maps were measured when a line source positioned from the center to 100, 200, 300, 400 and 500 μm off the center, respectively. White lines indicate simulated peak positions of the transmitted THz wave at 0.5 THz and their bending degrees are marked on the right for clarity. Note that the transmitted THz wave was bended from 0 to 21.2 degrees when the line source moved from the center to 500 μm off the center. (g-i) Simulations of Thz beams bending with the same angle in a broadband from 0.4 to 0.6 THz.

4.4.2 Evaluation of resolution using a double-slit object

Next, the minimum imaging resolution and aberration of the transformed Luneburg lens is evaluated using a double-slit object with a width of 200 μm and an edge-to-edge distance of 300 μm. Both simulated and experimental results, as shown in Figs. 4-5(a) and (b), respectively, indicate that the double-slit feature is well resolved over the same broadband THz spectrum of 0.4 to 0.6 THz. In Fig. 4-5(b), white circles are included to represent the peak position obtained from numerical simulations, thus showing good agreement between simulations and measurements. One should note that at 0.4 THz, the resolved feature size is very close to the diffraction limit resolution of 279 μm, which is estimated using the highest index of the transformed lens. To contrast these results, in the control case of a spherical lens made of homogenous dielectric material (n = 1.6), the simulation results shown in Fig. 4-5(c) indicate that the double-slit feature is no longer observable at any frequency below 0.5 THz due to lens intrinsic spherical aberration. In order to better illustrate the difference, the simulated and measured THz amplitudes at 0.5 THz for the aforementioned three cases is shown in Fig. 4-5(d). Plots of experimental measurement (red circles) and simulation (black curve) with transformed Luneburg lens resemble each other very closely, clearly showing two obvious separated peaks and demonstrating the double-slit resolved. Whereas the curve of imaging with uniform spherical lens (blue curve) only exhibits two minor peaks that are hardly to resolve, what is more, the peaks are completely not resolved at frequencies below 0.5 THz. These results demonstrate that the transformed Luneburg lens significantly improves the resolution limitation due to effective reduction of optical aberration.

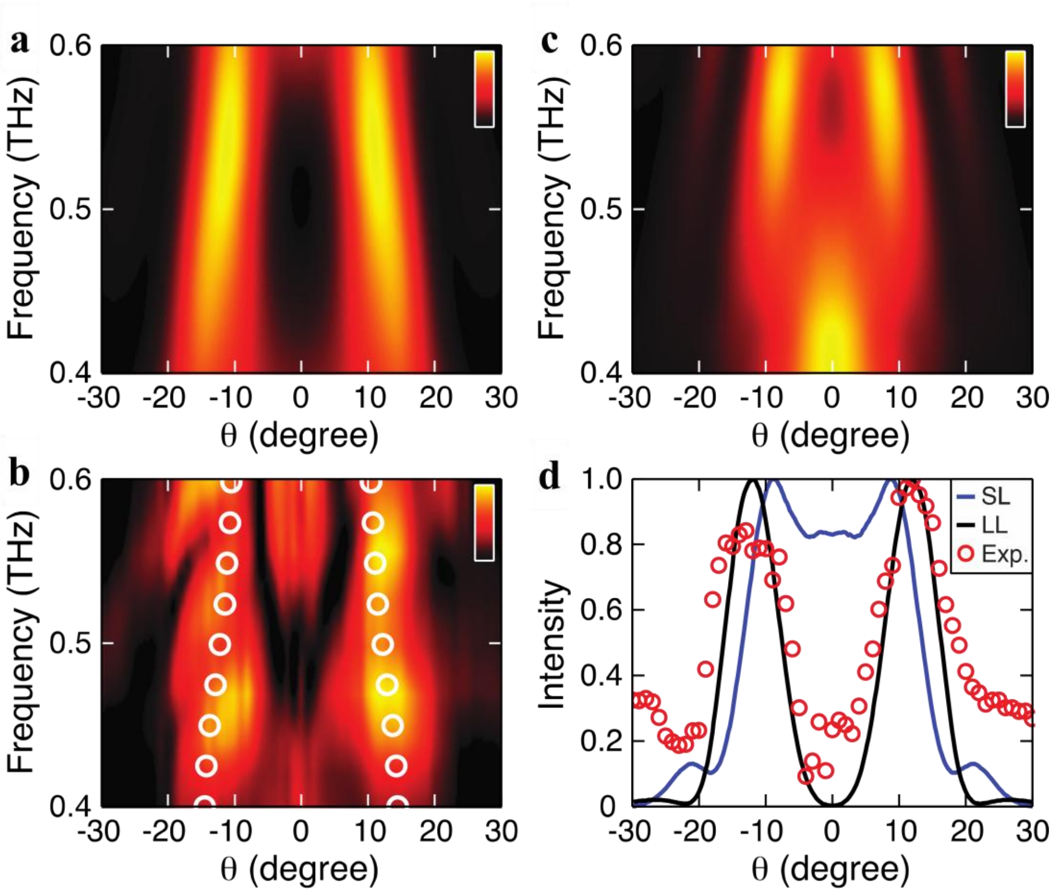

Figure 4-5. A 300 μm edge-to-edge spaced double-slit object is imaged by transformed Luneburg lens. (a) The simulation spectra show the double-slit feature can be clearly resolved over a broadband from 0.4 to 0.6 THz by using the transformed Luneburg lens. (b) The experimental results exhibit two obvious spatial maxima, which match very well with the simulated values (white circles) extracted from (a). (c) The simulation result shows a uniform spherical lens (n = 1.6) can only resolved the double-slit feature above 0.5 THz due to the existence of geometrical aberration. (d) Intensity as function of detector position for above three cases at 0.5 THz. Experimental and simulated results of imaging with transformed Luneburg lens have similar intensity distribution, which are distinct from the simulation result of imaging with uniform spherical lens, showing excellent imaging performance due to low aberration.

4.4.3 Demonstration of 2D imaging capability

Taking advantage of its polarization independent characteristics, the transformed Luneburg lens is capable of imaging any arbitrary object without aberration. Here, an N-shaped mask is used to demonstrate the 2D imaging capability of the transformed Luneburg lens. The letter “N” has dimension of approximate 950 μm × 950 μm, with line width of 200 μm, as shown in Fig. 4-6(a). Simulation results of imaging the letter “N” with the transformed Luneburg lens and the spherical lens are shown in Figs. 4-6(b) and (c), respectively. Clearly, the transformed Luneburg lens is able to image the letter “N” with fine features, which are barely resolved with the spherical lens. The recorded image at 0.6 THz of the letter “N” in Fig. 4-6(d) demonstrates the fabricated transformed Luneburg lens has relatively good agreement with the ideal one. The imaging resolution of 300 μm is achieved at the wavelength of 500 μm. The weak signal appearing at the upper and lower portion of the image “N” is likely due to the angular dependent sensitivity of the mobile detector scanning along the vertical direction. To further improve the ultimate quality of transformed Luneburg lens in this proof-of-concept experiment, circle scanning rails needs to be integrated in both axes and more dense scanning points needs to be recorded, at the expense of a more complicated optical system and longer scanning time.

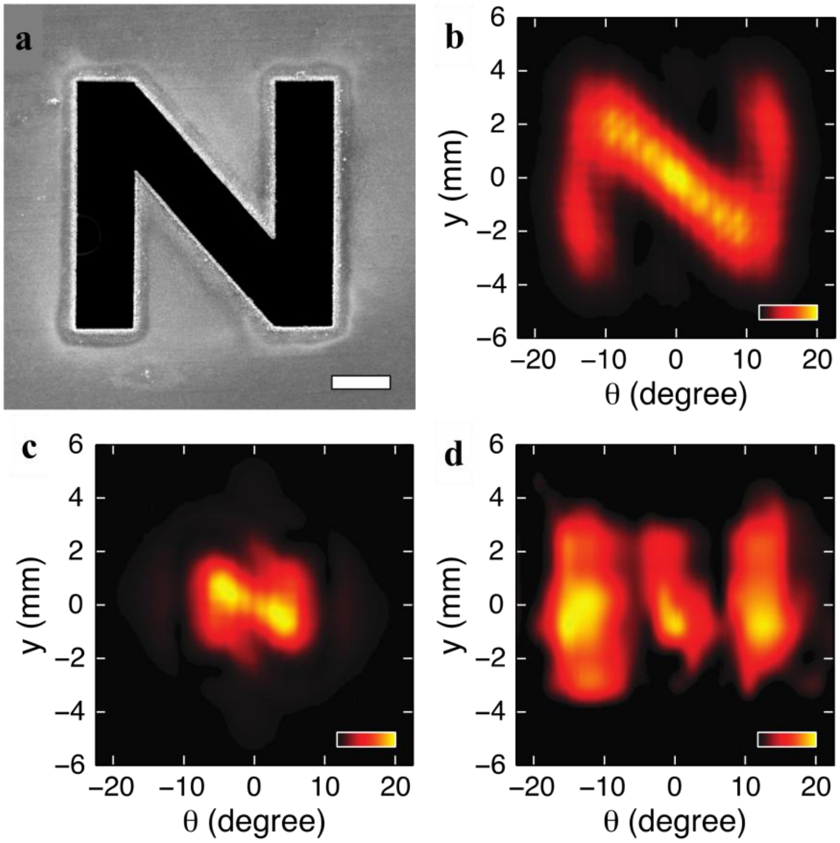

Figure 4-6. 2D imaging of an arbitrary object “N”. (a) SEM image of the “N” mask. Bar: 200 µm. (b) and (c) Simulated results of the letter “N” imaged by a transformed Luneburg lens and a conventional spherical lens, respectively. (d) Experimental measurement of “N” imaged at 0.6 THz.

4.5 Summary

Design, realization and measurements of novel THz Luneburg lens based on transformation optics are demonstrated. This is the first 3D lens functioning at THz frequencies. Polarization independent woodpile structures are used to build the lens and thus the lens can work with both TM and TE polarization. Both simulated and experimental results indicate the successful demonstration of aberration-free imaging using transformed Luneburg lens. Such a single gradient index lens is capable of delivering superior image quality with the resolution very close to the diffraction limit. The object can also include spectral signatures, which can be characterized by the intensity variation at a certain frequency on the imaging plane. The combination of transformation optics, metamaterials, and the scalable 3D fabrication process set the stage to the further development of advanced optical system with superior performance.

CHAPTER V

HIGH Q-FACTOR METAMATERIAL INDUCED TRANSPARENCY

5.1 Electromagnetically induced transparency

Nowadays, a strong interest has emerged in metamaterial research. Scientists are seeking to realize sharp, low-loss resonances and strongly dispersive behavior in planar, two-dimensional structures of sub-wavelength thickness by using interference effects that suppress radiation leakage [91].

The key role in this area offers an intriguing analogy with the well-known quantum phenomenon of EIT [92]. Recent studies show that planar metamaterials of certain patterns can lead to the EIT like effect through mimicking the EIT quantum phenomenon.

Typical three-level atomic system is used to demonstrate EIT [92]. As shown in Fig. 5-1(a), the absorption occurs, when the ground state is coupled to the excited state. In contrast, a pump beam couples the meta-stable state to the excited state, while there is not allowed to transit between the ground and the meta-stable state. When the probe and the pump beams simultaneously radiate, as illustrated in Fig. 5-1(b), the resulting destructive interference between the two transitions suppresses the probability of electrons existing in excited state and leads to a narrow transparency window at certain frequency in the spectrum of the otherwise opaque atomic medium in Fig. 5-2. As a result, the probe beam can propagate without losses.

There is a typical method to produce EIT like spectral features, which is so called Fano resonances appearing due to the two resonances at the close frequencies to each other as breaking symmetry occurs [93-100]. When the symmetry is broken, the anti-symmetric currents are established due to the coupling of the two resonators. The scattered wave destructively interferes and the loss is minimized. Consequently, the resonance mode has a long life term and there is an EIT like transparency window in spectral characteristic.

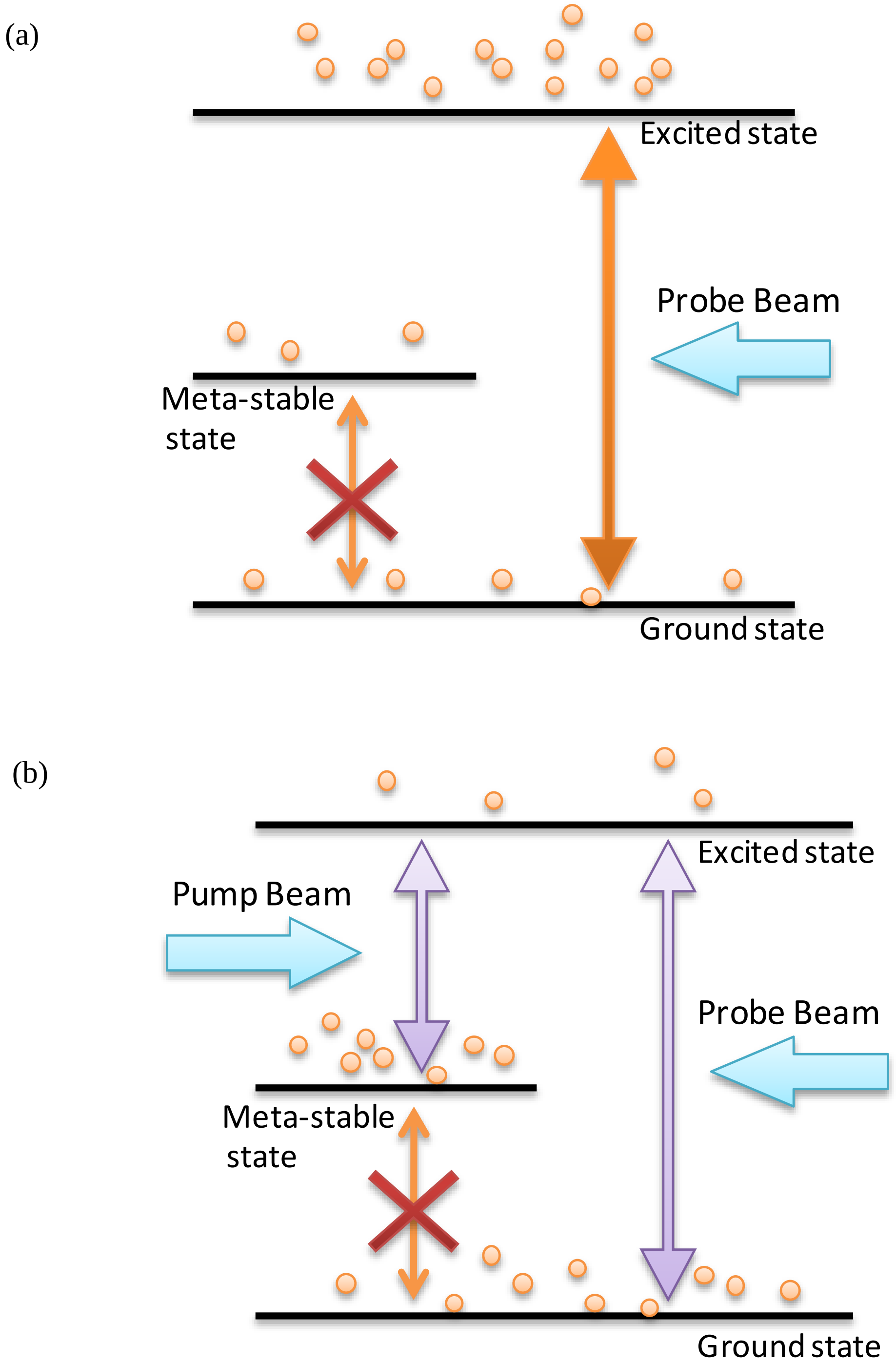

Figure 5-1. Three-level atomic system analogue of electromagnetically induced transparency. (a) Absorption of the probe is defined by the transition from the ground state to the excited state. (b) The transparency window opens due to the destructive interference as the pump is applied.

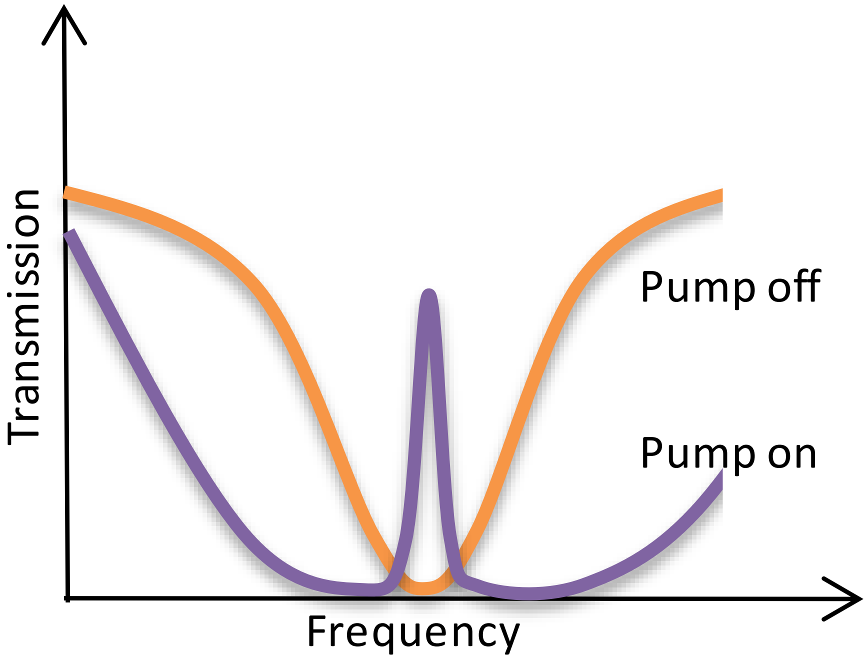

Figure 5-2. The absorption line experiences as the pump is absent. The obvious transparency window opens in the absorption line when the pump is applied.

5.2 Sample fabrication

All samples prepared are metal arrays of subwavelength asymmetric split-ring resonators (ASRs) on silicon substrate. The fabrication process consists of typical photolithography and thermal metallization. The ASR samples are fabricated on a 500-μm-thick N-type silicon wafer with resistivity of ρ = 20 Ω cm. A photoresist-adhesive primer HMDS is applied and spun at 3000 rpm for 30 seconds, and then a positive photoresist S-1813 Shipley is spin-coated at 3000 rpm for another 30 seconds, at which the thickness of the photoresist layer is approximately 1.5 μm. Soft–bake is applied at 115 ℃ for 5 minutes in convective oven to evaporate the coating solvent and to densify the photoresist after spin coating. The wafer is sequentially exposed with a contact mode mask aligner using UV light (λ = 436 nm) while under the mask. Toluene is used to improve the sharper outline after which the samples is developed using immersion methods in a solution of 1:7 Developer 351 and DI water. For metallization, 200-nm-thick aluminum layer is thermally evaporated on the patterned photoresist using a thermal evaporator (BOC Edward 306) at the vacuum pressure of 4.0×10^{-5} mB. After the lift-off process in acetone ASRs array with periodicity of 80 μm is formed.

5.3 Broadband 8-F confocal THz-TDS setup

A THz-TDS transmission system as shown in Fig. 5-3 [23] is employed to characterize the resonant properties of the ultra high Q-factor planar metamaterials. The parabolic mirrors are arranged in 8-F confocal geometry which provides excellent beam coupling between the transmitter and receiver. The Gaussian beam of THz pulses is focused to a frequency independent beam waist of diameter 3.5 mm for small sample characterization at the center between parabolic mirrors M_2 and M_3, whose focal length is both 50 mm. The transmitter and receiver are incident with 30 femtosecond pulses, which are of average power 10 mW, wavelength 800 nm, and repetition rate 88 MHz. This 8-F setup is able to characterize broad usable bandwidth from 0.2 to 4.5 THz.

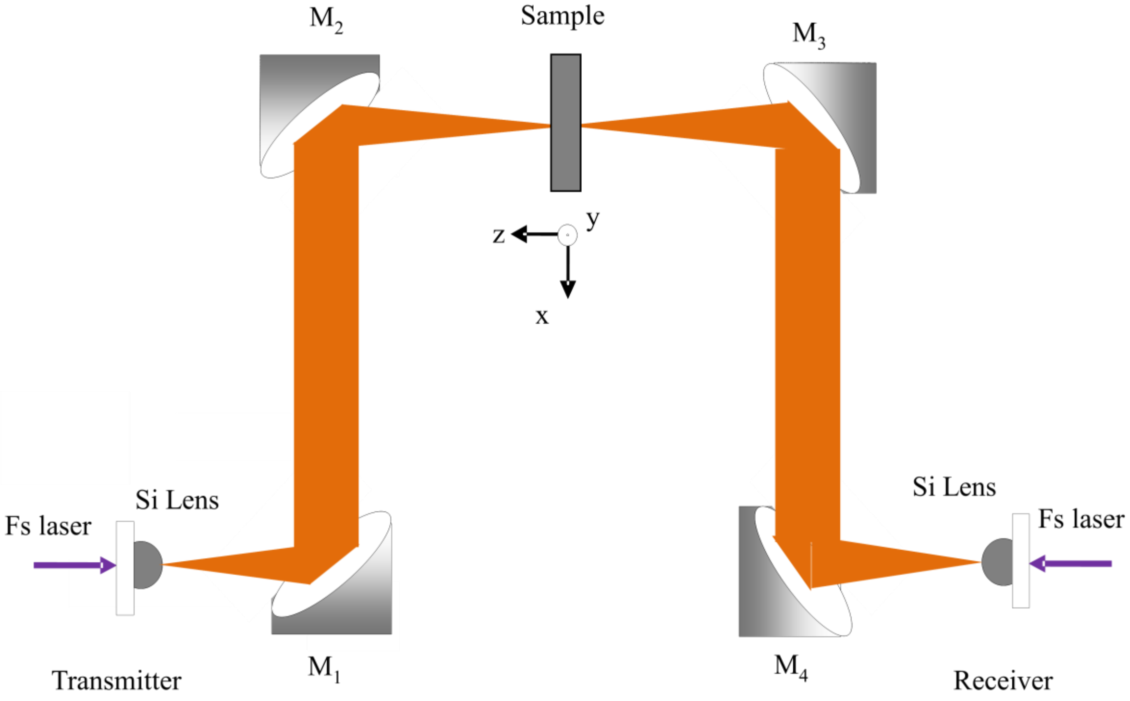

Figure 5-3. Schematic illustration of modified THz-TDS setup with an 8-F confocal geometry. Frequency independent beam waist is obtained between mirrors M_2 and M_3.

5.4 Sample design and simulations

Asymmetry in the ASRs is introduced by displacing the lower gap gradually from the upper center gap, as shown in Fig. 5-4(a) with δ=1, 2, 3, 4, 5, 10, and 20 µm, where δ represents the lower gap displacement parameter. Fig. 5-4(b) shows the microscopic image of an ASR unit cell with dimensions of g= 3 µm, t= 6 µm, l= 60 µm, and the lattice constant P= 80 µm. Each sample size is 10 mm × 10 mm.

In Fig. 5-5, the simulations for all the seven samples are shown. Starting from the asymmetric parameter (δ=1 µm) where the transparency window appears at the frequency 1.13THz. While moving to asymmetric parameter δ from 1 to 10 µm, the transparency windows open up at exactly the same frequency. Just in the δ=20 µm case, it slightly moves to 1.14 THz. And it is important to notice that the Q-factor can reach extremely high of 227.8 while δ=1 µm. When the asymmetry is further shifted, the transparency resonance band widens as well as amplitude transmission increases. Then for δ=20 µm, the transmission of 95% can be achieved.

As the parameter δ gradually µm is increased, a transparency in the spectrum at 1.13 THz becomes more and more obvious as the transparency window band width enlarges and its amplitude transmission shifts to 1. The parameter δ plays a key role to control the linewidth and the amplitude transmission of the EIT resonance in this metamaterial system.

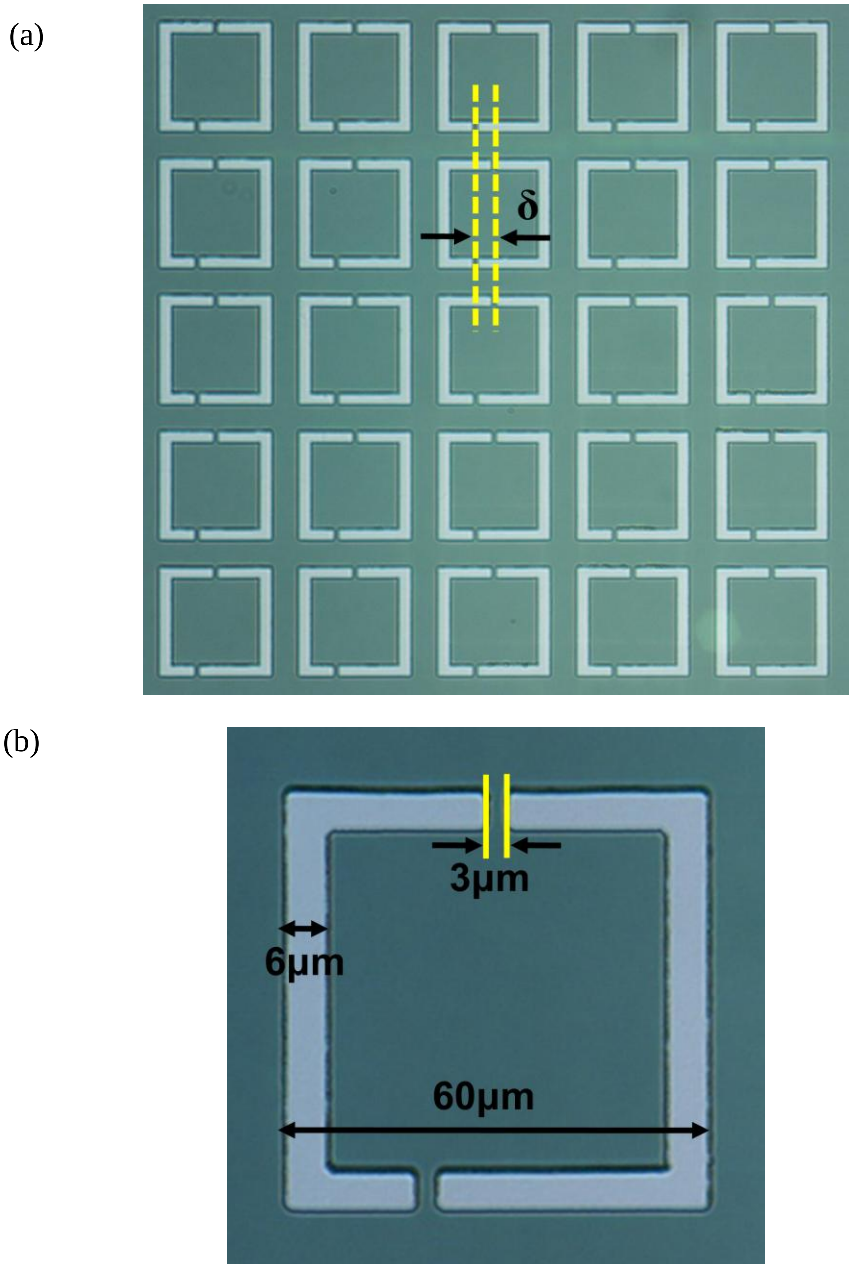

Figure 5-4. Microscope image of asymmetric split rings, (a) the lower gap is shifted with different values of δ from the upper center gap, (b) unit cell with geometry dimensions.

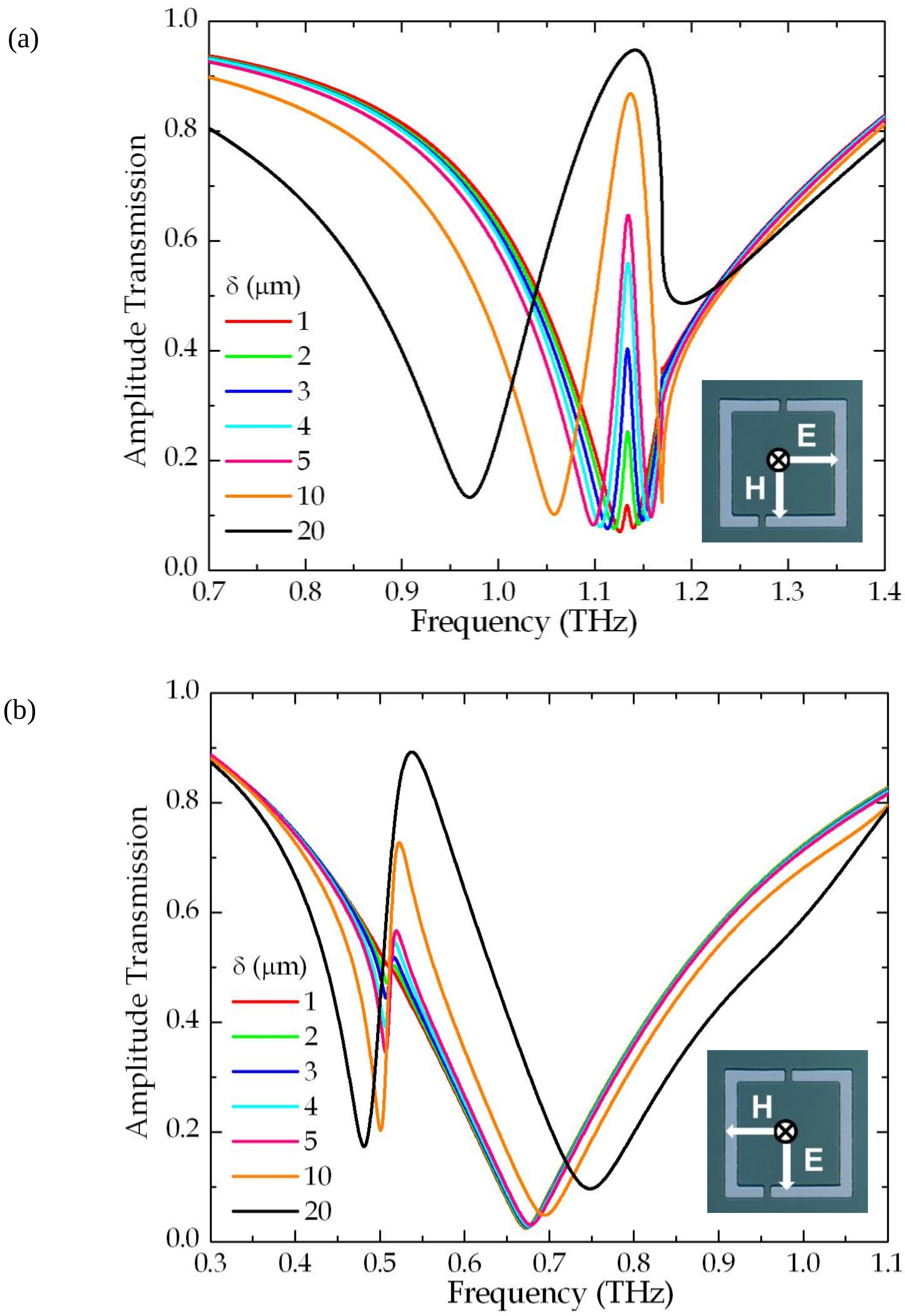

Figure 5-5. Simulated (a) and (b) amplitude transmission spectra of ASRs for an E field orientation parallel and perpendicular to the gaps, respectively. The insets show the E and H field orientation for each case.

5.5 Experimental measurements

A broadband THz-TDS is employed to characterize the ultra high Q-factor planar metamaterials. The photoconductive switch based THz-TDS system consists of four parabolic mirrors configured in an 8-F confocal geometry that can provide excellent beam coupling between the transmitter and receiver. The Gaussian beam of the THz pulse is focused to a frequency independent beam waist of 3.5 mm for small sample characterization. In the THz-TDS measurements, each metamaterial sample is placed midway between the transmitter and receiver in the far-field at the focused beam waist, and the transmitted THz pulses are measured at normal incidence such that the electric (E) and magnetic (H) field of the incident radiation is in the metamaterial plane.

Seven sets of ASR metamaterial samples are fabricated on a high-resistivity (4 kΩ·cm) double-side polished 500 μm thick n-type silicon substrate using conventional photolithography, and then a 200 nm thick aluminum is thermally metallized to form the ASRs. A 10 mm thick, high-resistivity (4 kΩ·cm) silicon plate is placed in optical contact with the backside of the metamaterial substrate, in order to eliminate Fabry-Perot echoes from the metamaterial substrate bottom surface, and allow us achieve a long scan up to 200 ps, thus enabling a frequency resolution of 5 GHz [95].

The time domain data are taken for all the seven matamaterial samples in a sequential order for both orientations of the E field. Fig. 5-6 shows the measured THz pulses transmitted through the ASRs (δ= 5 μm) and the blank silicon slab identical to the ASRs substrate as reference while the E field is vertical to the ASRs gap. A strong oscillation in the pulse is observed at a late time, as shown in the top inset of Fig. 5-6(a), which indicates the strong loss into the free space is effectively suppressed. The Fourier transform of the time-domain pulses is shown is Fig. 5-6(b), which clearly reveals a very sharp bandpass resonance feature with a high Q-factor.

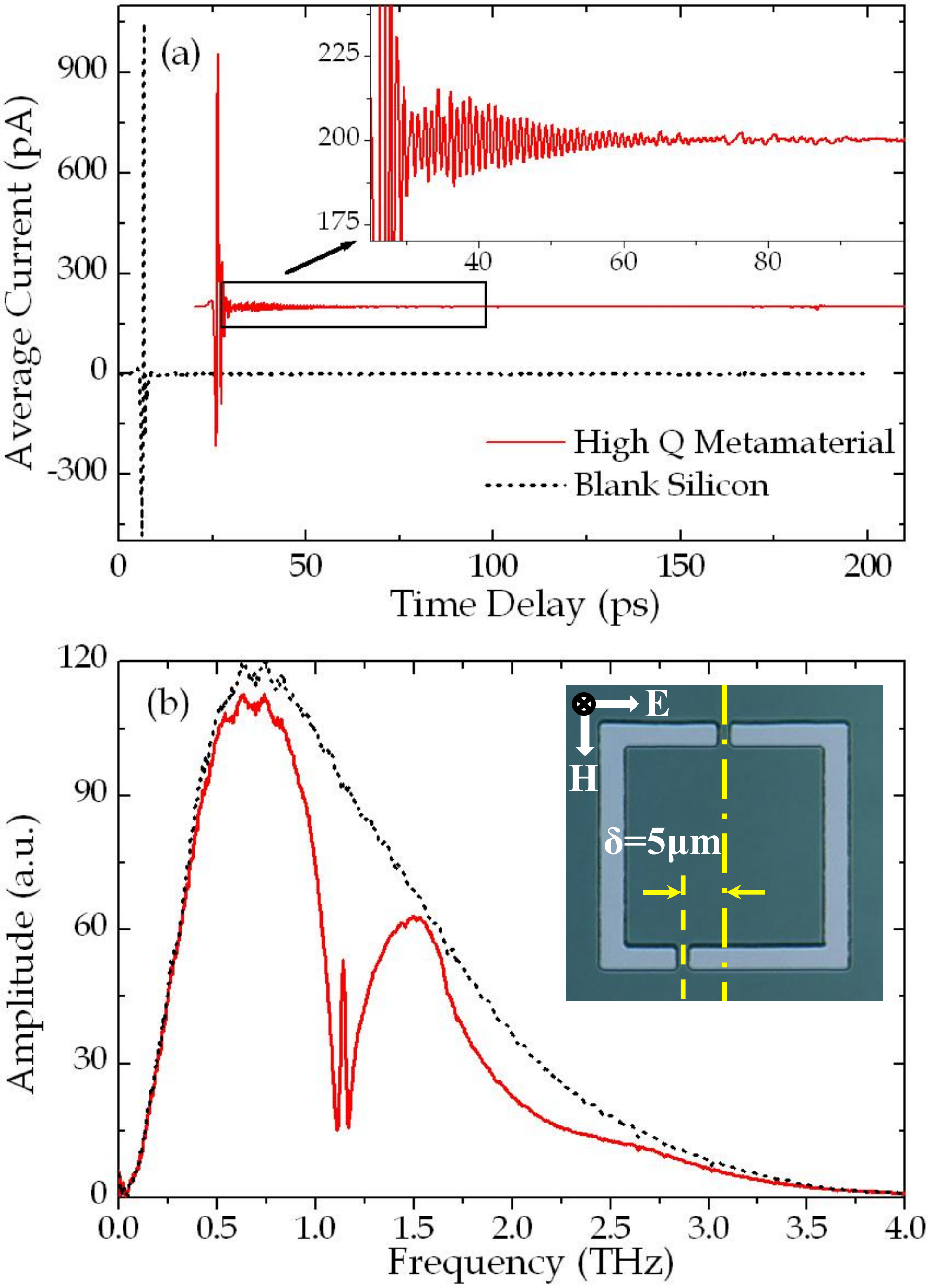

Figure 5-6. Measured time domain terahertz pulse through ASRs metamaterial sample and reference.

The transmission amplitude is derived from the ratio of the Fourier-transformed amplitude spectra of the ASRs sample to the reference, defined as $|E_s(\omega)/E_r(\omega)|$, where $E_s(\omega)$ and $E_r(\omega)$ are Fourier-transformed time traces of the transmitted electric fields of the sample and reference pulses, respectively. Fig. 5-7 shows the measured transmission spectra through all seven samples with varied asymmetry. The electric field in this case is oriented parallel and vertical to the gaps, as indicated in the insets, respectively. As illustrated in Fig. 5-7(a), it is observed that for the asymmetry δ= 20 µm a transparency window locates at 1.14 THz and has a 93% transmittance, which meets the simulation at frequency of 1.13 THz and amplitude transmission of 95% very well, between two resonance dips at 1 THz and 1.23 THz. The transparency window does not shift in frequency while the asymmetry δ alters. The Fig. 5-7(b) shows a transparency window at 0.56 THz with 80% transmittance is observed as the asymmetry δ= 20 µm. The decrease in asymmetry δ from 20 µm to 1 µm gives the transparency window a red shift by 30 GHz in frequency.

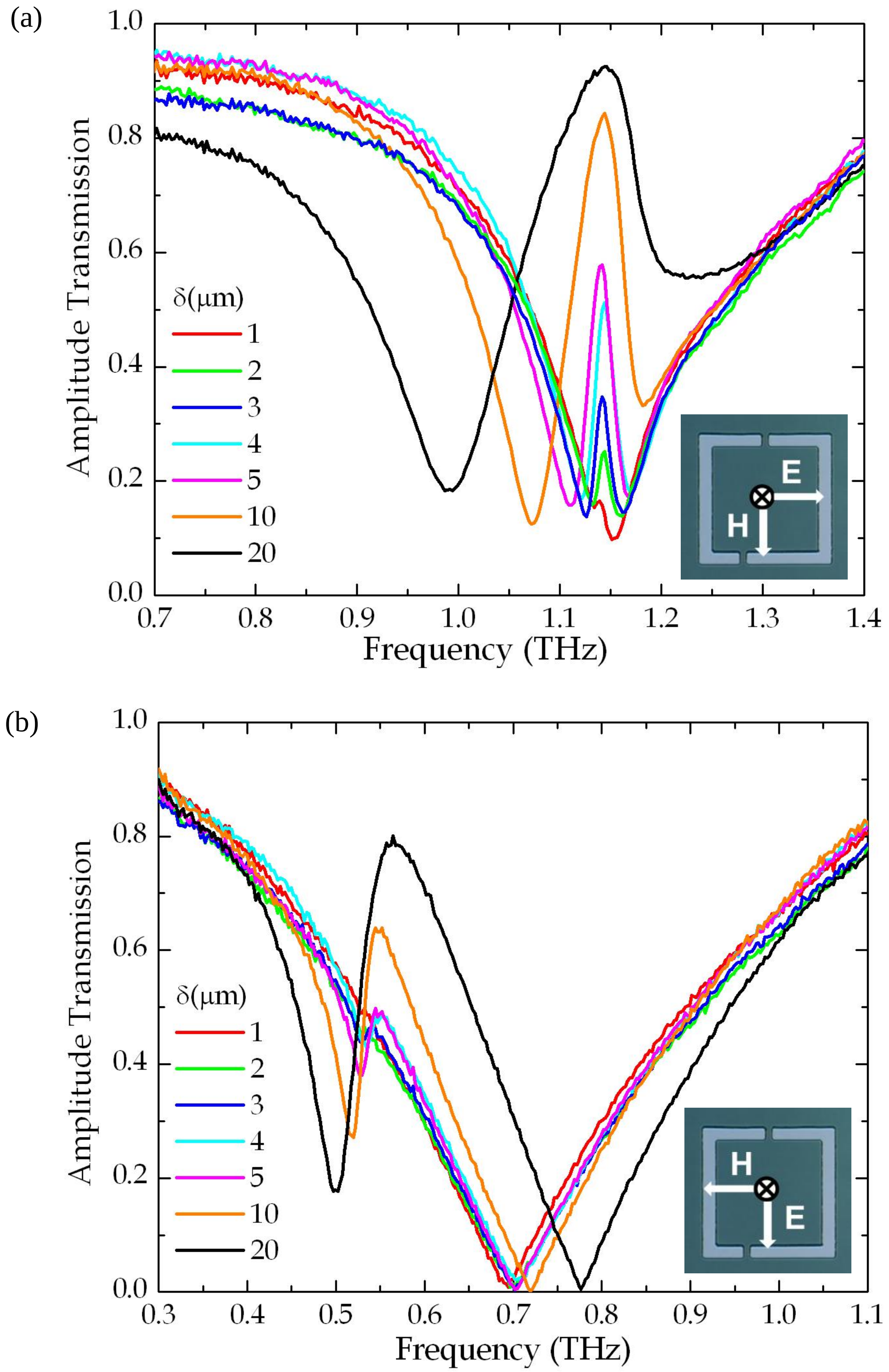

Figure 5-7. Measured (a) and (b) amplitude transmission spectra of ASRs for an E field orientation parallel and perpendicular to the gaps, respectively. The insets show the E and H field orientation for each case.

As can be seen from Fig. 5-7, when we gradually alter displacement of the lower gap, evolution of the transparency window is observed. It can be seen that the strength of the transparency window increases with increasing asymmetry parameter. The same is true for the width of transparency window. The sharpest transparency window is observed for a small asymmetry of δ= 1 μm. In this case, the ultra high Q-factor reaches 227.8 and 43.4 for both E field orientations. Figure 5-8 shows that the Q-factor approximately exponentially decreases as δ is increased from 1 μm to 20 μm, which meet the simulation fairly well, and an ultra high Q-factor of 227.8 has been successfully fulfilled.

We select the highest peak and lowest dip on the resonance curve and define the full width at half maximum (Δf_{FWHM}) as bandwidth. Taking the ratio of the resonance frequency f_0 and Δf_{FWHM} ($f_0/\Delta f_{\mathrm{FWHM}}$), the value of Q-factor is obtained. The best Q-factor of 227.8 is observed for the lowest asymmetry case of δ= 1 μm, though the resonance feature is extremely weak. Beyond that as the bottom gap is moved away from the center, the Q-factor decreases but the transmission gets enhanced. In order to quantize the tradeoff between the Q-factor and the resonant transmission, we define the product of Q and resonance amplitude (A) as the figure of merit (FOM) = Q*A. The FOM of all the structures is plotted in the inset of Fig. 5-8(c) and we obtain the best FOM = 47 for asymmetry δ= 4 μm.

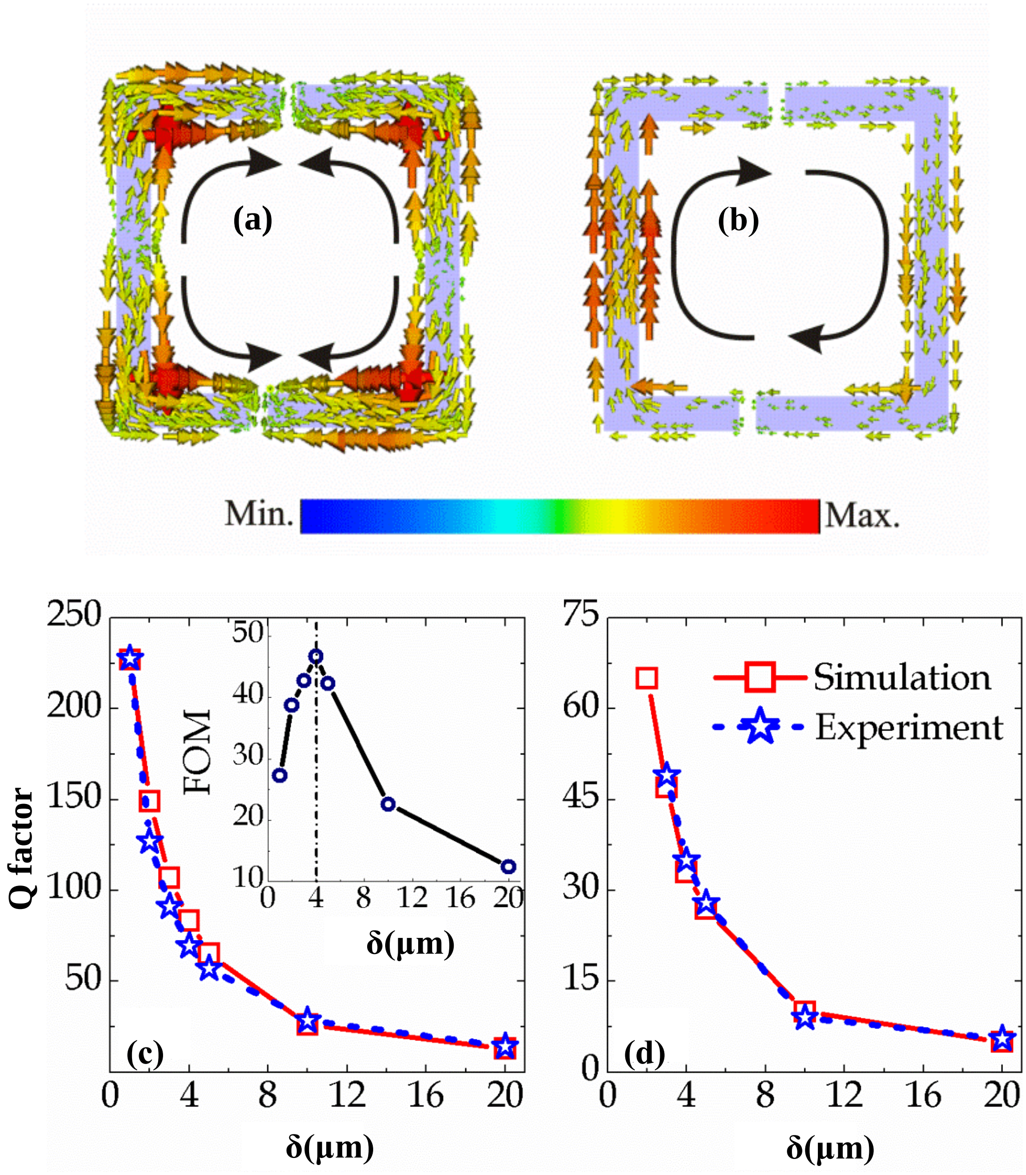

Figure 5-8. Surface current simulations in asymmetry δ= 5 μm (a) transmission resonance peak at 1.14 THz when the E field is along the gap in the *x* direction, (b) transmission resonance dip at 0.5 THz when the E field is perpendicular to the gap in the *y* direction. Q-factors calculated from the measurement and simulations for (c) E field along the gap and (d) E field perpendicular to the gap. The inset of (c) shows the figure of merit.

5.6 Discussion and analysis

In symmetric case, at the symmetric dipole resonance mode frequency, constructive interference comes out resulting in a strong coupling leading to a broad dipole. The upper and lower arms have parallel surface currents, which are strongly radiative in nature. Figure 5-8(a) shows that once the symmetry is gently broken, anti-parallel currents appear, and the destructive interference is stimulated and derived from anti-symmetric currents, which effectively damps the radiative scattering and renders incident THz wave transmit with extremely low loss, and then the metamaterial induced transparency effect occurs. Figure 5-8(b) shows the anti-parallel surface current distribution of a typical subradiant Fano resonance when ASRs are excited with incident E field in the *y* direction.

5.7 Summary

Using high resolution THz-TDS transmission measurements, we experimentally demonstrate a metamaterial induced transparency with extraordinary high Q-factors due to the excitation of Fano resonances. An extremely sharp transparency window appears, while slightly moving one gap of the unit cell away from the center of one arm. By using long-range scanning to obviously improve the resolution of THz-TDS system, the Q-factors are effectively enhanced and the radiation losses are further reduced. This renders the proposed metamaterial an outstanding candidate for the use in slow light devices, THz signal delay and storage, and high-performance sensors.

CHAPTER VI

THERMAL TUNABILITY IN PLASMON INDUCED TRANSPARENCY

6.1 Thermally active metamaterial for plasmon induced transparency

It is important to realize that EIT is an essential mechanism that leads to slow light. The Kramers–Kronig relations dictate that a change in absorption (or gain) over a narrow spectral range must be accompanied by a change in refractive index over a similarly narrow region. This rapid and positive change in refractive index enables an extremely low group velocity [101].

Hau and co-workers achieved a record in slowing down light group velocity through EIT at cryogenic temperatures in an ultracold atomic gas [101]. Slow light opens the door to a whole new range of exciting avenues such as nonlinear effects arising from the enhanced timescale of light matter interactions. It could also lead to the development of sophisticated all-optical information processing that can store, delay, and switch optical data bits. There is also a strong demand for the design and development of all-optical buffer memories and routers that could provide an active control over the flow of data in the next-generation telecommunication networks, without the requirement to convert optical signals to electronic data. Additionally, slow-light medium is anticipated to have a far-reaching impact on electromagnetic signal processing, radar systems and quantum information science [24].

The classical field interference that mimics the quantum EIT phenomena has been demonstrated as a means for the cancellation of absorption of electromagnetic wave propagating through artificially designed plasmonic metamaterials at a desired frequency which would otherwise be non-transparent [102-121]. This phenomenon has been termed as plasmon-induced transparency (PIT). PIT involves coupling between two distinct resonators in a unit cell of the metamaterial. One of the resonators is highly radiative possessing a broader resonance feature and is called a “bright” resonator, whereas the other resonator is sub-radiant “dark” resonator since it has a much sharper resonance linewidth. The destructive interference between strongly coupled bright and dark resonators results in a well-defined narrow transparency window. Most of the previous schemes consist of coupling between two passive resonators that would not allow the active tuning of the PIT window. In a recent work, active control of the PIT peak was achieved by integrating a photosensitive material in the split gap of the dark resonator and by exciting the metamaterial with an infrared pump laser [122]. Here we present a thermally active superconductor-metal coupled resonator based hybrid terahertz metamaterial that shows thermally tunable transparency and slow light behavior.

6.2 Sample fabrication

The metamaterial unit cell investigated here comprises of a high-temperature superconductor, Yttrium barium copper oxide (YBCO), and close-ring resonator (CRR) that acts as a bright element and a metal split-ring resonator (SRR) as a dark element. The metamaterial unit cell consisting of an aluminum metal SRR enclosed within an outer YBCO CRR is illustrated in Fig. 6-1(a). The metamaterial sample is lithographically fabricated on a commercial (THEVA, Germany) 280-nm-thick YBCO film, which typically has a phase transition temperature, T_c = 85 K and a critical current density of 2.3 MA/cm^2 grown on a 500-μm-thick sapphire substrate. A 3-μm-thick photoresist layer is first patterned with the outer closed rings on the raw YBCO film as an etching protective layer. The sample is then wet etched in 0.04% nitric acid to remove the YBCO from other parts of the wafer that do not have the photoresist protection, forming the closed ring arrays. The 200-nm-thick aluminum SRRs are aligned and fabricated at the center of the outer closed rings by the conventional optical lithography. The microscopic images and geometric parameters are illustrated in Fig. 6-1. The size of the sample array is 10 mm × 10 mm and contains about 40,000 unit cells of hybrid SRR-CRR metal-superconductor structures.

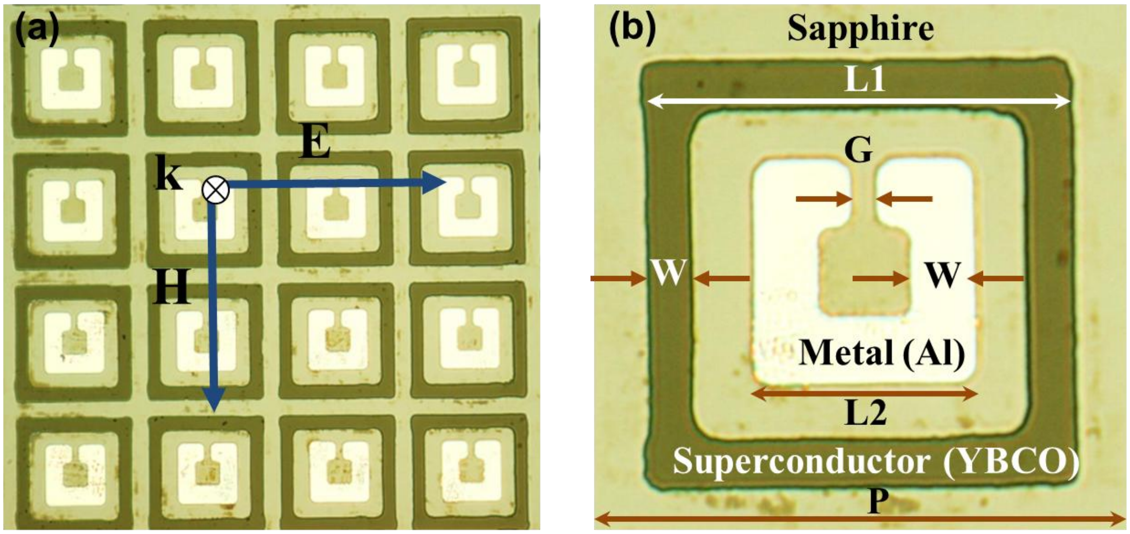

Figure 6-1. Microscopic images of (a) a periodic metamaterial array on a sapphire substrate and (b) a metamaterial unit cell with geometrical parameters: L1 = 45 μm, L2 = 22 μm, W = 6 μm, G = 3 μm and a periodicity of P = 50 μm. The incident direction of radiation is normal to the plane and the E field is parallel to the gap of the inner SRRs.

6.3 Sample design and simulations

While designing the metamaterial structure for fabrication, we perform detailed numerical simulations using CST Microwave Studio^{TM}. We simulate the behavior of metal SRR and superconductor CRR individually and ensure that their resonance frequencies are close by and the Q-factors are highly contrasting. Figure 6-2(a) shows the inductive-capacitive (LC) resonance of inner metallic SRR excited at ~1 THz with a Q-factor of = 7.71. At the LC resonance, the excited surface currents in the SRRs are circular and possess a magnetic moment perpendicular to the plane of the metamaterial [123,124]. The LC resonance in metal SRRs does not show any significant change by increasing the conductivity of the metal at THz frequencies, thus there is no noticeable difference in the response of metal SRRs at room temperature and at liquid helium temperature [125].

Figure 6-2(b) reveals the behavior of a superconducting CRR array at different temperatures. Since CRR is a perfectly symmetrical structure, a plasmonic dipolar resonance is excited by the incident THz field. At room temperature, a dipole resonance appears to be extremely weak due to the poor conductivity of the superconductor. As the temperature is lowered down, a resonance gradually evolves due to the increase in YBCO film conductivity and subsequent excitation of strong dipolar surface currents in CRR. At temperature below T_c, the dipole resonance exhibits a switching effect since resonance amplitude increases dramatically below the superconducting phase transition temperature at which there is formation of Cooper pairs that enhances the imaginary part of the YBCO film conductivity by three orders of magnitude [126,127]. The red shift in the dipolar resonance is due to the kinetic inductance of the superconductor film. A strong dipole resonance can be observed at 51 K and 27 K at 0. 83 THz with a Q-factor of 0.88. One should note an order of magnitude difference in the Q-factors of LC and dipole resonances.

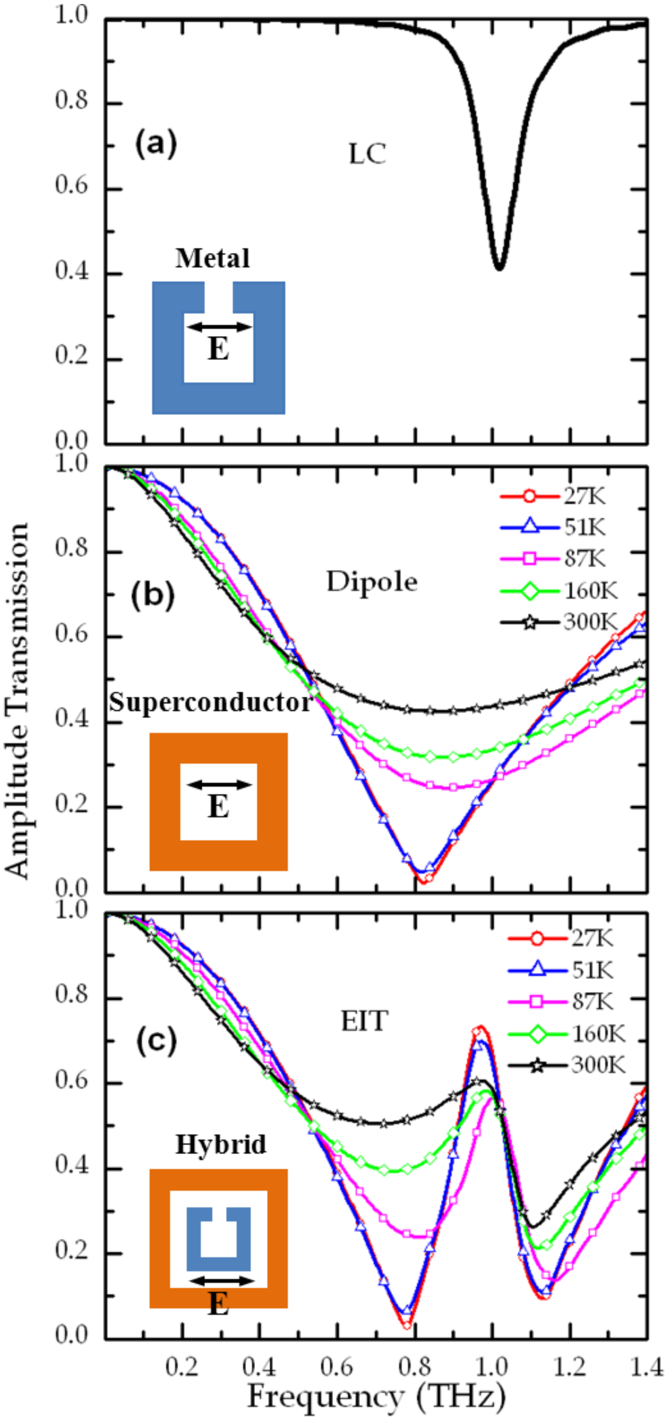

Figure 6-2. Simulated transmission spectra of the isolated resonators and coupled PIT structure. (a) LC resonance of metallic inner SRR, (b) dipole resonance of outer CRR at various temperatures, and (c) EIT resonance peak in hybrid superconductor-metal structure at various temperatures.

After the two resonator arrays, namely, metal SRR and superconductor CRR are simulated individually, we further bring the two resonator structures together in a unit cell with the CRR enclosing the smaller SRR structure with both structures being concentric in order to achieve strong coupling. Figure 6-2(c) shows the transmission spectra of the hybrid CRR-SRR metamaterial structure at different temperatures. The CRR-SRR system can be represented as two coupled damped harmonic oscillators. When significant coupling occurs as the temperature is lower than T_c, normal mode splitting results in two new Lorentzian-like resonances with distinct eigen frequencies and damping rates or resonance line widths. The coupling between the metal SRR and the superconductor CRR is the strongest at the lowest temperature that the metamaterial chip is cooled down to. The coupling occurs due to the strong spatial overlap of near fields of the SRR and the CRR. A temperature tunable transparency resonance band is observed due to the destructive interference between the sub-radiant (dark) metal SRR and the super-radiant (bright) superconducting CRR. The coupling occurs via the near field interaction of the electromagnetic fields at the LC resonance of the metallic SRR and the dipolar resonance of the superconductor CRR [128-131]. The electromagnetic field in the metal resonator remains strong at room temperature as well as at low temperature due to high conductivity of metals at terahertz frequencies. However, the coupling strength between the resonators increases below the superconducting phase transition temperature due to the excitation of strong dipolar currents in the superconductor CRR. The coupling depends on the Q factor of individual resonators since they center around the same resonance frequency in order to achieve the strong coupling.

6.4 Experimental measurements and analysis

The transparency mimics the quantum mechanical EIT phenomena in atomic physics. In order to verify our simulations, we perform transmission measurements through fabricating identical structures of hybrid metamaterial using THz-TDS system, as shown in Fig. 6-3. We observe the tunable sharp PIT resonance band by decreasing the temperature of the metamaterial chip. The amplitude modulation is more dramatic at much lower temperature of 15 K, thus achieving an active switching and modulation behavior of the PIT window around 1 THz.

The attraction of this work lies in the active thermal control of the bright mode superconducting CRR dipole resonance. At room temperature, the superconductor acts as a poor metal and thus cannot support the excitation of a resonance in the CRR, whereas the metallic SRR shows a strong LC resonance. As the metamaterial chip is cooled down to lower temperatures, the superconductor CRR begins to resonate at the same frequency as the metal SRR leading to a tunable coupling between the resonators. The degree of coupling is controlled through the superconductor active resonator. Even though, the thermal control is slow compared to electrical and optical tuning, the advantage of using high temperature superconductor is the observation of a temperature dependent switching effect due to the phase change of the superconductor. The phase change in superconductors is unique to the temperature dependence and the hybrid PIT metamaterial used here inherits this unique behavior in the form of dynamic temperature based switching of the PIT resonance band.

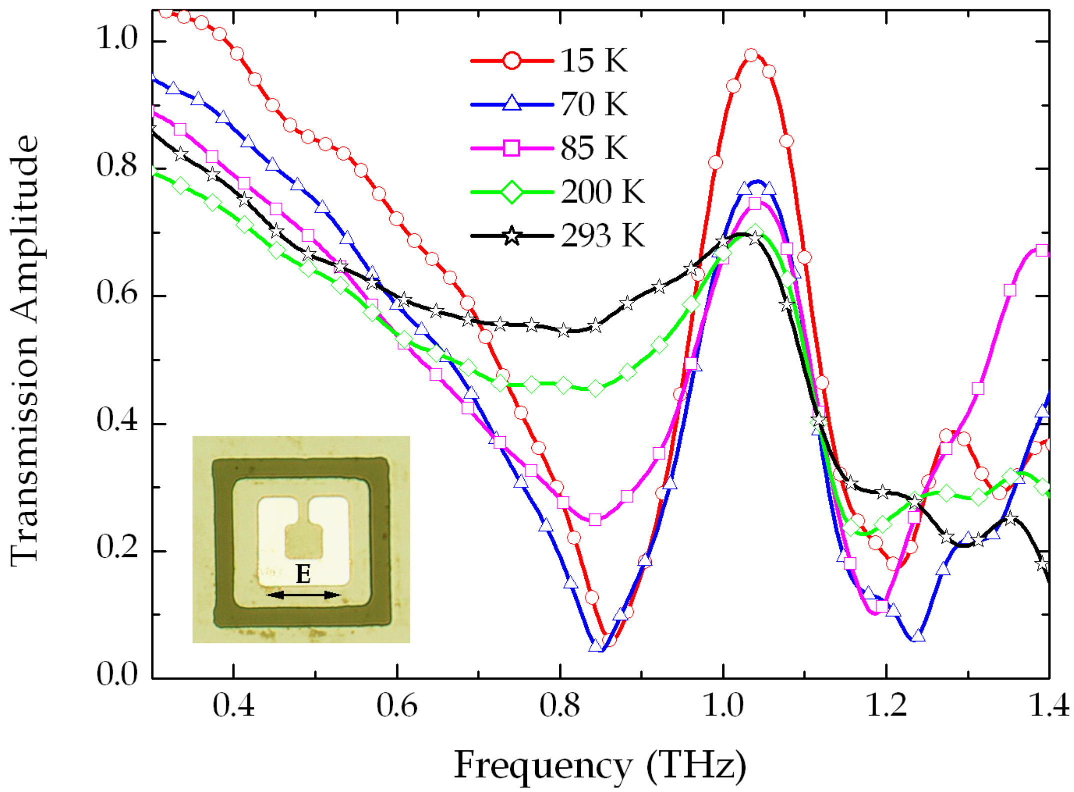

Figure 6-3. Experimental transmission spectra of the superconductor-metal hybrid PIT metamaterial, revealing tunable transparency at different temperatures.

In order to elucidate the nature of these resonances, we numerically simulate the surface current distribution and electric fields at the lowest temperature and at resonance frequencies of two dips (0.77 and 1.13 THz, respectively) and the transparency peak (0.98 THz). At the resonance dips, as shown in Figs. 6-4(a) and (c), the strong currents are excited in the CRR as well as in the SRR indicating a hybridized mode. At the lower frequency resonance (0.77 THz), the currents in both resonators are antiparallel and at the higher frequency dip (1.13 THz), the surface currents are parallel. On the contrary, in Fig. 6-4(b), the surface currents are completely suppressed in the outer CRR due to destructive interference between the two resonators. The excitation at the PIT peak is confined only to the inner SRR, expelling the currents completely from the superconducting CRRs. Looking at the E field simulations, the strongest fields are observed at the PIT peak (0.98 THz) in Fig. 6-4(e) near the SRR gap which conveys that there is inductive transfer of near field energy from the super-radiative CRR to the dark SRR. The electromagnetic field is coupled back and forth between the bright superconducting CRR and dark metal SRR atoms, leading to a destructive interference and thus, the suppression of field in the super-radiative outer CRR. In Figs. 6-4(d) and (f), the fields at the resonance dips of 0.77 THz and 1.13 THz, respectively are seen to be distributed on SRR and CRR due to the coupled modes at these eigen frequencies.

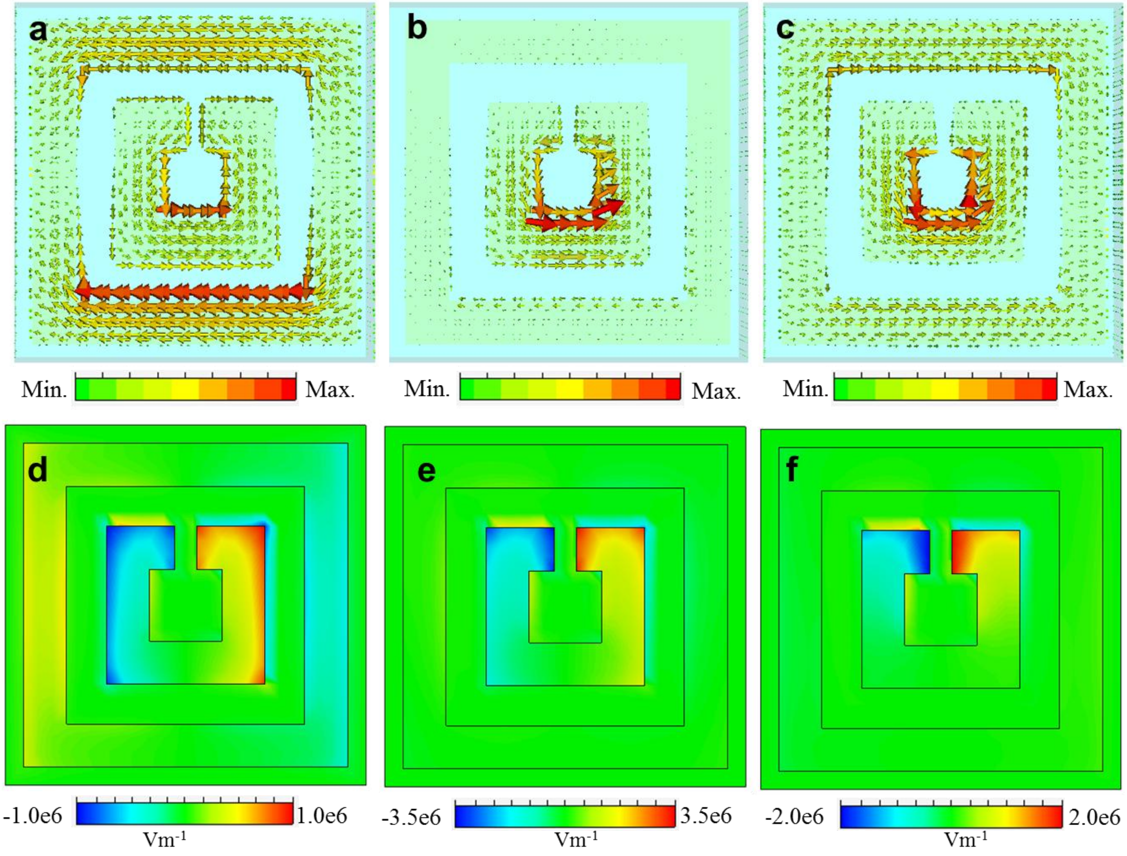

Figure 6-4. Simulated surface currents and E field distributions in the hybrid PIT metamaterial structure at resonance frequencies of (a), (d) 0.77 THz (first dip); (b), (e) 0.98 THz (transparency peak) and; (c), (f) 1.13 THz (second dip) at 27 K.

From the transmission spectra and the PIT resonance band in Fig. 6-3, it can be easily recognized that the strong dispersion leads to a huge group delay that occurs in the transparency window. This indicates that a light pulse with a central frequency situated in the transparency window will be considerably slowed down while propagating through the hybrid metamaterial. Through our measurements, we demonstrate a thermally tunable slow-light effect represented by the group delay (Δt_{g}) of the THz wave packet through the metamaterial sample relative to the sapphire substrate reference. Group delay is defined as the negative derivative of the phase response with respect to the angular frequency,

$$\Delta t_g = -\frac{d\varphi}{d\omega}, \tag{6-1}$$

through a transmission medium, where φ is the total phase shift in radians, and ω is the angular frequency. In our measurements, the sapphire substrate is the reference, EIT metamaterial is the sample, then

$$\Delta t_g = -\frac{d\Delta\varphi}{df}\cdot\frac{1}{2\pi} = -\frac{d(\varphi_{ref}-\varphi_{sam})}{df}\cdot\frac{1}{2\pi}, \tag{6-2}$$

The difference in Δt_{g} through the EIT metamaterial and reference is retrieved from complex transmissions at different temperatures, as shown in Fig. 6-5. We observe that the wave packet with central frequency of 1 THz is delayed by 2.5 ps at 15 K. At temperatures above the superconducting phase transition, the slow-light effect is almost negligible. Notably, the group delay retrieved from the measurements Fig. 6-5(a) and simulations Fig. 6-5(b) match very much.

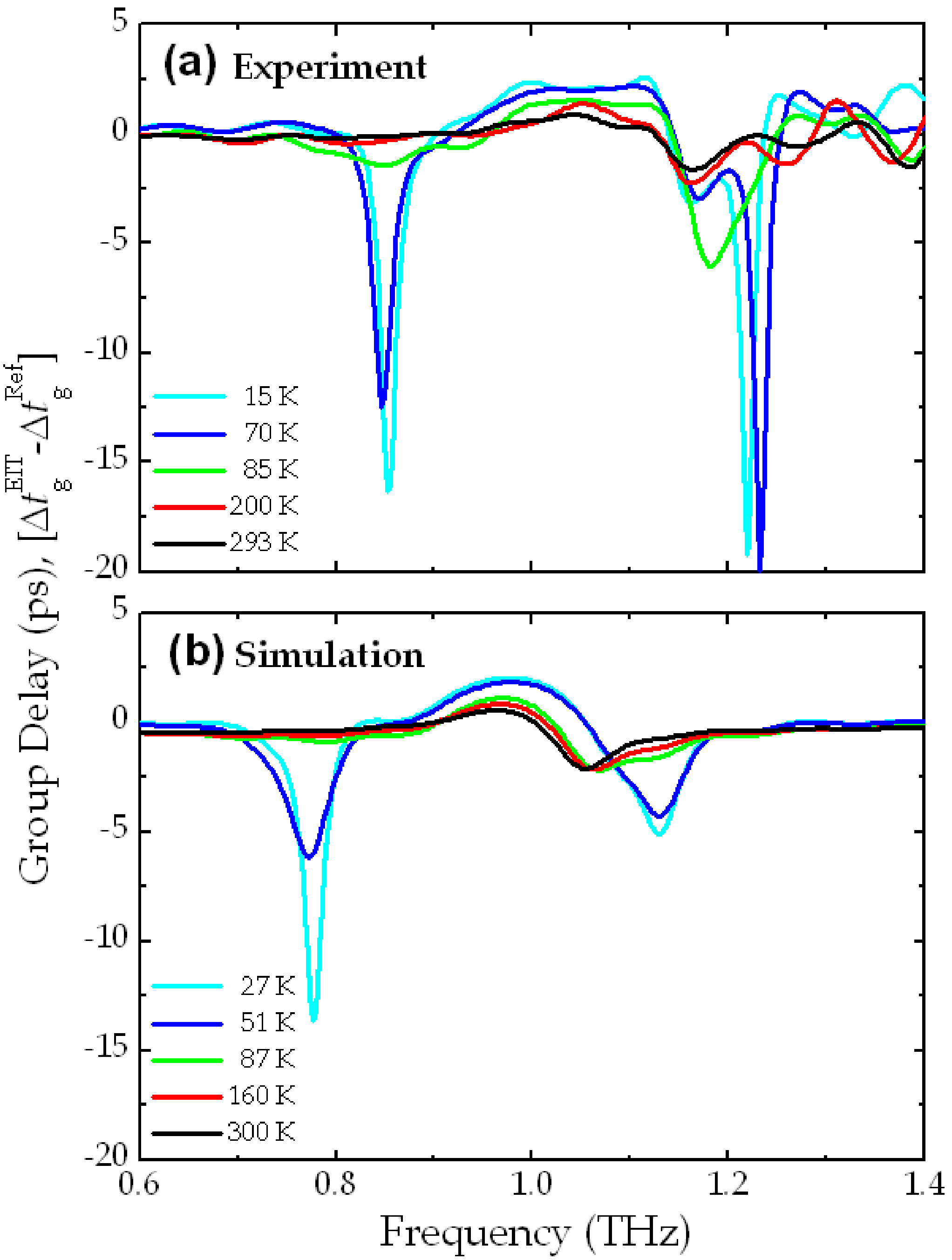

Figure 6-5. Thermally tunable active group delay. (a) Group delays retrieved from measured transmission spectra of the hybrid PIT metamaterial at different temperatures. (b) Group delays extracted from simulated transmission spectra.

6.5 Summary

In conclusion, we demonstrate a thermally tunable hybrid metal superconductor EIT metamaterial and slow-light effects. Strong coupling between dark metal SRR and bright superconducting resonator leads to a destructive interference of the scattered fields giving rise to an EIT phenomenon. The slow-light feature of the PIT phenomena in metamaterials is extremely attractive in strong light-matter interactions and enhanced nonlinear effects. This hybrid metamaterial device would find several applications such as regenerators for THz communication, light storage, and compact tunable THz delay lines. It also offers the opportunity for compressing THz signals in free space paving the path for applications in several THz devices, such as detectors, modulators, quantum cascade lasers, and amplifiers.

CHAPTER VII

TAILORING TERAHERTZ PLASMONS WITH SILVER NANOROD ARRAYS

7.1 Introduction

Recent developments in nanofabrication have opened new opportunities to fabricate metallic nanostructures with tunable porosity and alignment, and can be integrated into conventional micro-fabrication process. Engineered nanostructures with controlled porosity and morphology could systematically tune the dielectric and polarization properties of metals in the THz regime. The combination of the material control on multiple size scales could be a key enabler. Combining nanostructured thin films with microstructured plasmonic metamaterials will give us a new opportunity to design and explore novel THz devices with unique functionality.

We present a study of the THz response of well-aligned silver nanorod array films and a THz SP resonant device that has been lithographically patterned using these silver nanorod films. Our results demonstrate that anisotropic thin metallic nanorod structures can be used to tune the THz response and can be another important strategy to design THz plasmonic metamaterial based devices.

7.2 Sample design and fabrication

Aligned and tilted silver nanorod (AgNR) arrays are fabricated directly on silicon substrates by oblique angle deposition (OAD) method in a custom-designed electron-beam evaporation system [132, 133]. During the deposition, the Ag vapor flux is incident onto the silicon substrates at an angle of 86°, resulting in nanorods of 1 μm in length, 100 nm in diameter, and a tilt angle of 72° with respect to the surface normal [132, 133]. Figure 7-1 (a) shows a representative top view image of the AgNR arrays obtained by a scanning electron microscope (SEM, FEI Inspect F). The length, tilt angle, and porosity of the AgNRs can be controlled by the deposition rate, duration, and vapor incident angle, which result in tunable optical properties [134]. A THz-TDS system is employed to characterize the nanorod samples [23, 135]. Angle dependent transmission measurements are carried out to characterize the polarization properties of the unpatterned AgNRs array. After each time-domain measurement, the sample is rotated with respect to the normal of its surface with an interval of 10°.

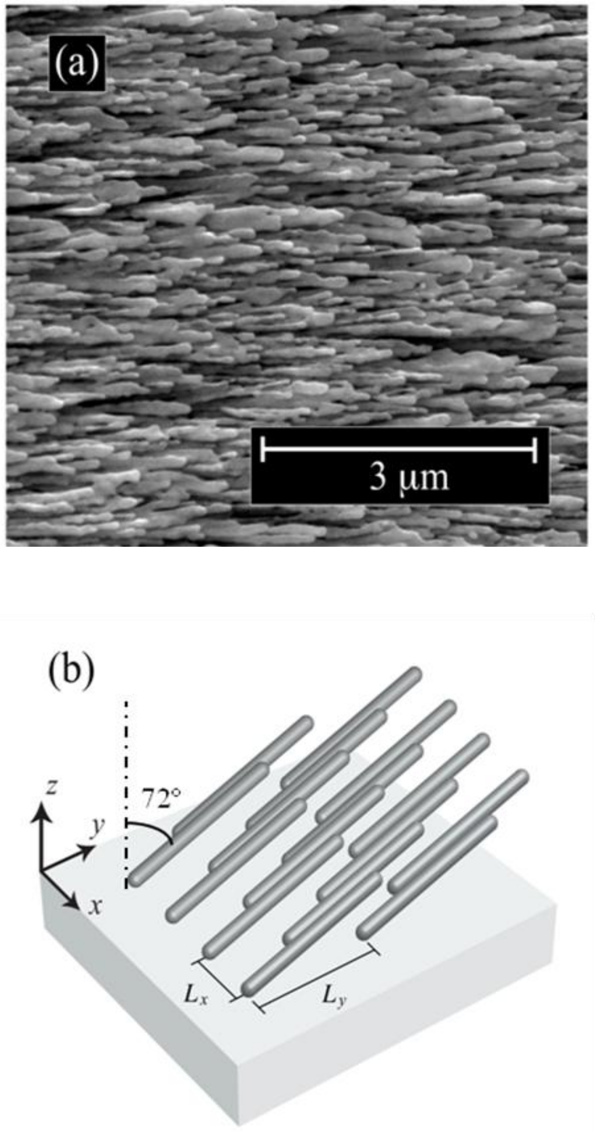

Figure 7-1. Illustration of morphology and dimensions of Ag nanorods. (a) SEM image of the Ag nanorods deposited on a silicon wafer. (b) Staggered base morphology derived from the SEM image. The rods have a diameter 100 nm, length 1 μm, and are oriented at a 72 ° angle with the substrate normal. L_x= 250 nm, L_y= 893 nm.

It is found that the THz properties of the nanorod arrays are tunable; in particular, the anisotropic arrangement of the AgNR arrays induces polarization dependence in the transmission of terahertz waves. Figures 7-2(a) and (b) show the transmitted time-domain pulses and the corresponding Fourier-transformed amplitude spectra of an AgNR array oriented at 0 ° and 90 °, respectively. Here, 0 ° and 90 ° represent the polarization of the THz electric field parallel and perpendicular to the direction of the long axis of the nanorod's projection onto the silicon substrate. As shown in Fig. 7-2(b), the unique anisotropic structure of the AgNR arrays resulted in a 4:1 contrast ratio in the amplitude transmission of THz pulses. Figure 7-2(c) shows a whole set of the polarization angle dependent transmission spectra. As the polarization angle increases from 0 ° to 90 °, the THz amplitude transmission becomes stronger.

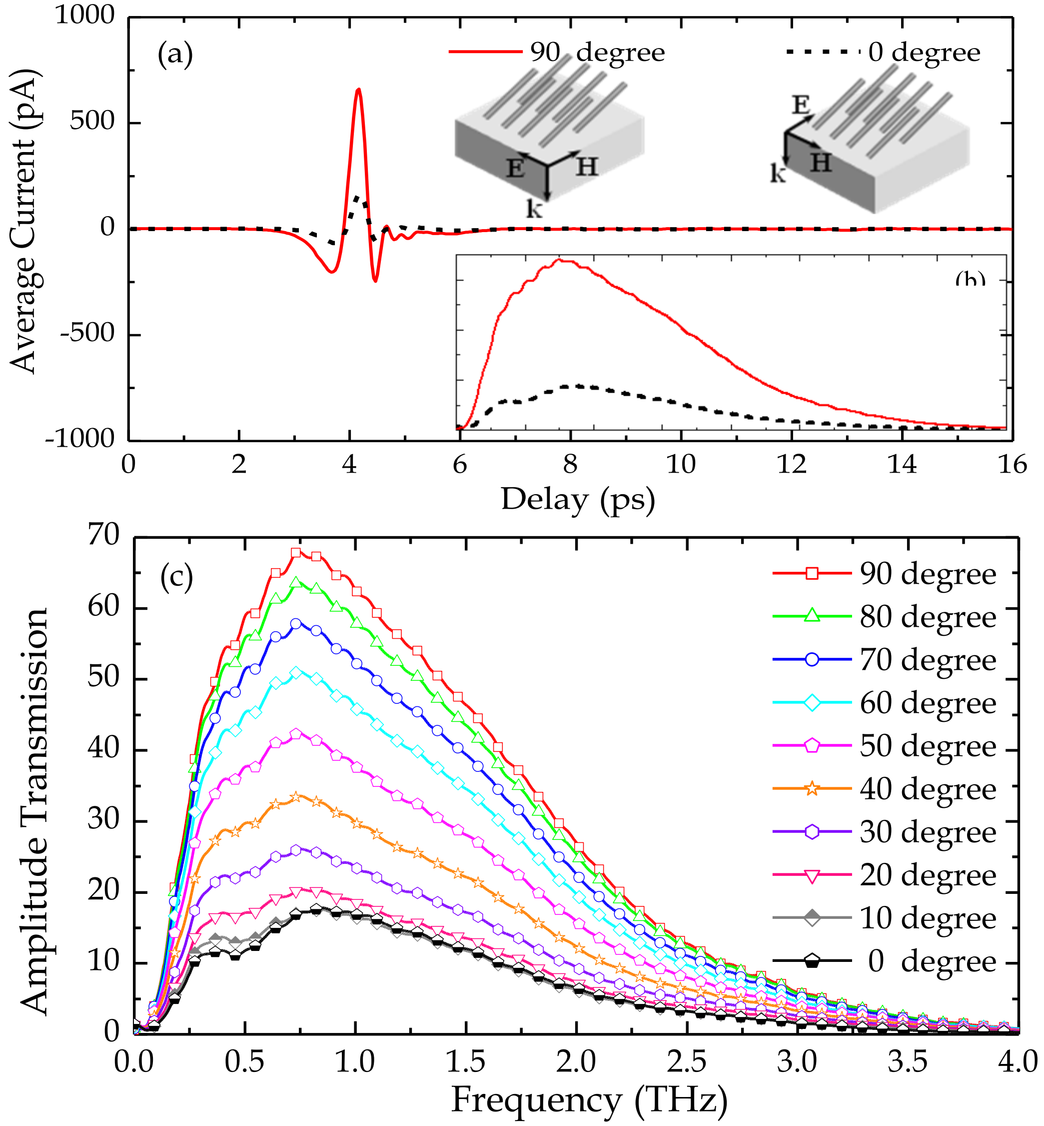

Figure 7-2. THz-TDS measured results of uniform Ag nanorod arrays. (a) Time-domain pulses transmitted through the Ag nanorod array at angles of 0° and 90°, respectively. Inset: corresponding Fourier-transformed spectra. (b) A complete set of THz-TDS spectra with the Ag nanorod array rotated about the normal to its surface at various angles.

7.3 Numerical simulations

Such a trend can be understood using numerical simulation by the finite-difference time-domain (FDTD) method (using the software package XFdtd (Remcom)). Figure 7-1(b) shows the staggered base morphology of AgNRs derived from the SEM image. We treat the AgNR arrays as round-tipped cylinders oriented with a tilt angle of 72 ° with respect to the surface normal and arranged in the plane of the substrate into a 2D rhombic lattice with the lattice dimensions L_x = 250 nm and L_y = 893 nm as defined in Fig. 7-1(b). Clearly this structure is an idealization of general features shown in Fig. 7-1(a). The actual samples have rods connected at various areas and separated to various extents. The connectivity of the nanorods is evidenced by four-point probe measurements of the anisotropic resistance of AgNR sample. The connectivity of the Ag nanorods is confirmed by resistance measurements by a four-point probe as shown in Fig. 7-3(a-c). The resistance depends on the probe orientation with respect to Ag nanorod tilt direction as shown in Fig. 7-3(d), and shows strong anisotropy: when the probe is perpendicular to the nanorod tilt direction, the sample has the maximum resistance; when the probe is parallel to the rod direction, the sample has the minimum resistance.

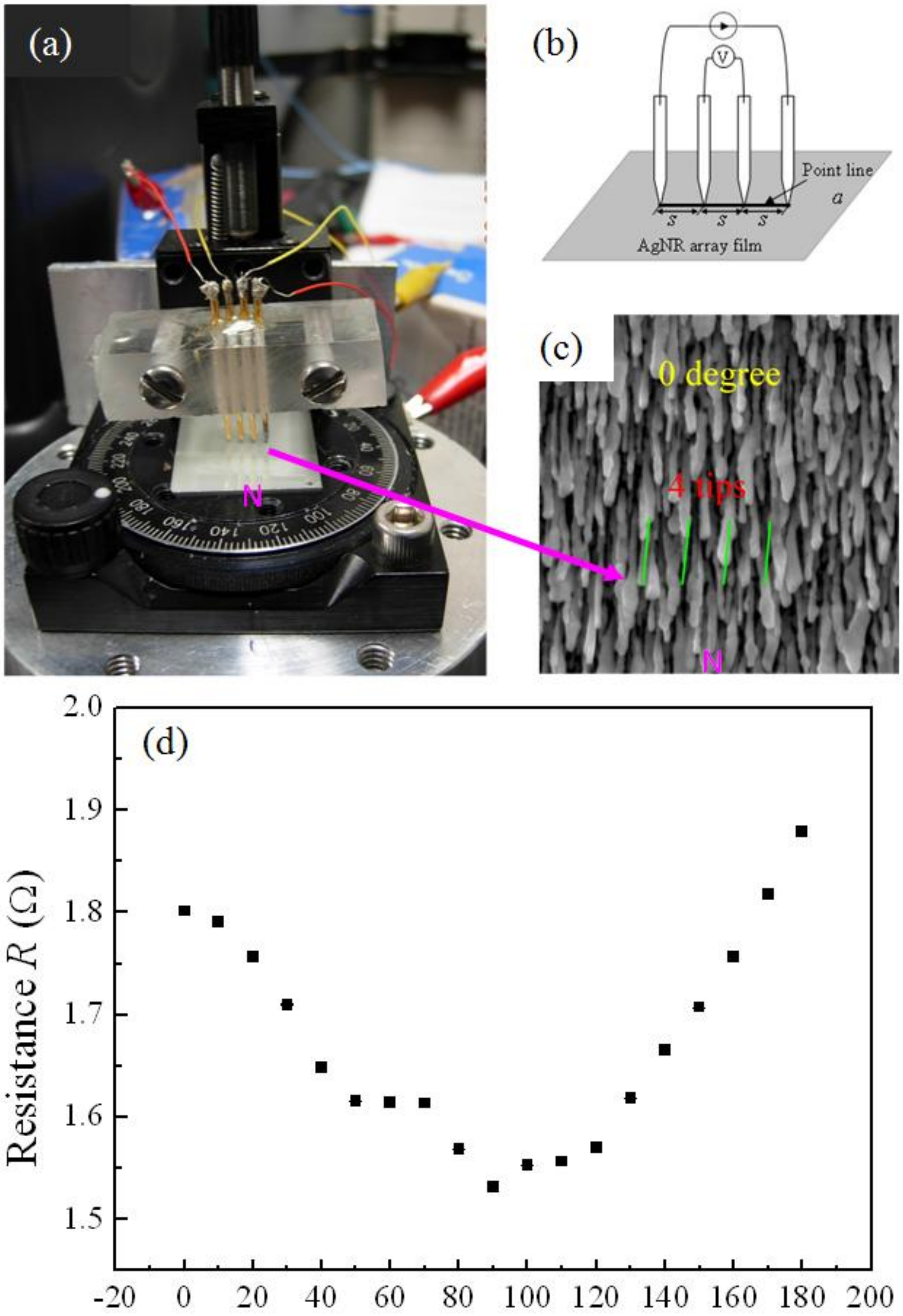

Figure 7-3. AgNR resistance measurements. (a) Experimental setup for resistance measurement, (b) Sketch map of the linear arranged 4-point probe configuration, and (c) the definition of 0° measurement (image not drawn to scale). (d) The measured AgNR resistance as a function of the probe angle with respect to nanorod tilting direction.

Thus, it is reasonable to further hypothesize that the rods are coupled by material connections that may be resistive or capacitive in nature. If the point of contact between rods is significantly smaller than the rod diameter, then the connection is resistive. If protuberances on rods are in very close proximity but not actually in contact, then the coupling is capacitive. Therefore, in the simulation we add resistive and capacitive connections to the 2D unit cell of the base morphology.

The simulations described here use ~1 ps Gaussian pulses centered at ~1 THz. We chose a spatial grid cell size of 8 nm with a mind to resolving the base morphology while maintaining reasonable computational size. This choice results in a staircased spatial meshing of the rods with features that are at most $10^{-4} \times \lambda_{\text{min}}$, where λ_{min} refers to the shortest wavelength contributing to the excitation spectrum. Spurious diffraction from curved material surfaces that are imperfectly realized on the discrete spatial grid may therefore be neglected. The ~0.01 fs time step that results from this choice according to the Courant stability condition ensures numerical stability for all frequencies and materials considered [136]. The size of the computational domain required was reduced by imposing periodic boundary conditions at the edges of the 893 nm × 250 nm unit cell, which corresponds to a physical system that is infinite in the plane of the substrate. Drude behavior in the AgNRs of the base morphology is implemented according to the permittivity [137] $\varepsilon(\omega) = 1 - \frac{\omega_p^2}{\omega(i\gamma+\omega)}$, where where $\omega_p = 1.37 \times 10^{16}$ rad/s is the plasma frequency and $\gamma = 8.20 \times 10^{13}$ rad/s is the scattering frequency [138-140]. For resistive inter-rod coupling in the y-direction, 100 nm diameter cylindrical connectors with scattering frequency γ increased by a factor of 16 are added at the rod tips. For resistive coupling in the x-direction, similar connectors with scattering frequency γ increased by a factor of 3.5 are added at rod bases. An additional rod with a 20 nm thick dielectric spacer with a dielectric constant of 800 is added for capacitive coupling across rod tips in the *x*-direction. If the simplistic form of capacitance in terms of parallel plates of area *A* separated by a dielectric with thickness *d* is assumed, then the higher dielectric constant of the capacitive element can be reduced to correspond to that of air while keeping the capacitance constant if *A/d* is increased by a factor of 800. Taking *A* to be the surface area of one of the rods and d = 1 nm constitutes one set of geometrical parameters that results in the same capacitance with unit dielectric constant. This combination of inter-rod coupling elements produces anisotropic high-pass filter behavior similar to that measured in our experiments.

The resistance measurements show strong anisotropy of the Ag nanorods. In order to model the experimental data, it is hypothesized that the rods are coupled by material connections that may be resistive or capacitive in nature due to the spatially fine details of the morphology. Attempting to accurately resolve these essentially random features, in the face of practical constraints on the memory footprint and computational run time, would be rather crude. Furthermore, the far-field, statistically significant THz transmission properties measured experimentally for the disordered rod arrays should be determined by the properties of some simplified morphology that captures those effects which survive a suitable spatial average. By assuming that the relevant transmission behavior can be captured by adding such connections to the base morphology, we avoid the boundless search of the parameter space of intricate morphologies, and instead gain insight into the inter-rod coupling by varying resistivities and dielectric constants of the added connective elements arranged to model the experimental results as closely as possible. Initially, orthogonal resistive connections are inserted and their scattering frequencies are varied to produce the overall magnitude of the transmission for *x*- and *y*-polarized incident pulses. During these investigations, a very weak high- or low-pass behavior resulted (this data has not been presented). For example, when normalized to the incident spectrum, the *y*-polarized transmittance is seen to decrease slightly with frequency, while the *x*-polarized transmittance increased slightly with frequency. This behavior is augmented by the addition of a capacitive element that leads to high- or low-pass behavior that depends on the polarization of the incident pulse and the arrangement and material parameters of the connective elements. This is analogous to a simple RC circuit that forms a voltage filter that preferentially transmits high or low frequencies depending on whether the output voltage is taken across the resistor or the capacitor. The choice depicted in Fig. 7-4 is the result to replicate the experimental results with minimal deviation from the base morphology, and minimal adjustment of the material parameters of the connections.

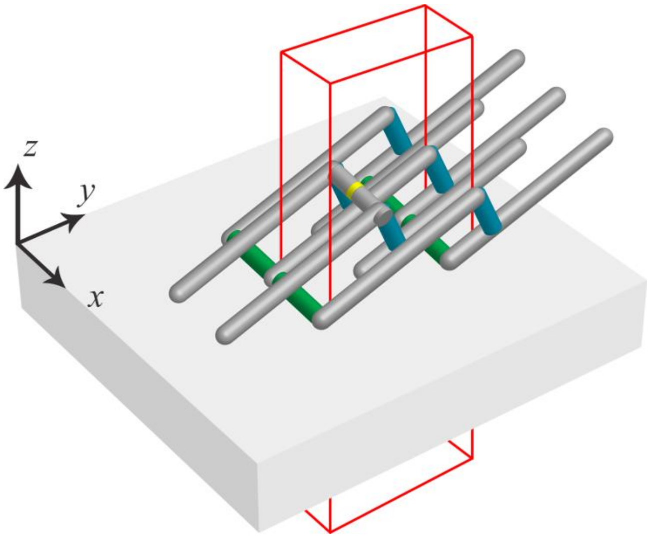

Figure 7-4. Schematic of the final connected morphology. The red box indicates the computational space (its extent in the *z*-direction has been truncated), where periodic boundary conditions are imposed on its *x* and *y* boundaries. Most rods and connective elements outside the unit cell have been removed for clarity. Yellow indicates the capacitive element, and green and blue indicates the distinct resistive elements.

7.4 Measurements and analysis

A THz-TDS system is employed to characterize the nanorod samples. Figure 7-5(b) shows the experimental normalized amplitude transmission spectra of the AgNR array with varied incident polarization under the THz-TDS system. The trends of the measured spectra are in good agreement with the numerical results calculated by the FDTD method, as shown in Fig. 7-5(a). In both experiment and simulation, it is observed that the transmission increases approximately linearly dependent on frequency at angles greater than 30°, although this effect is more pronounced in experiment. At the polarization angles of 0° and 15°, the transmittance remains almost unchanged with frequency. In all cases, transmission decays with decreased polarization angle. The majority of the transmission drop occurs between polarization angles 30° and 75°. We consider the agreement between the simulation and experimental results shown in Fig. 7-5 to be limited by the constraint to morphologies with translational symmetry of such small lattice vectors. In other words, the investigation of connections within the smallest unit cell of the staggered base morphology is computationally convenient, but limits the accessible spatial extent of impedance-matched electrical pathways. With this limitation, the spatial confinement of uniformly damped oscillations in and on Drude materials is limited by the unit cell size. Longer-range impedance-matched electrical pathways are thought to be responsible for the non-monotonicity occurring in the normalized transmission spectra measured in our experiments at intermediate incident polarization angles as shown in Fig. 7-5(b). We conclude that the nanorod shape and orientation produce effective anisotropic bulk conductivity to the THz radiation.

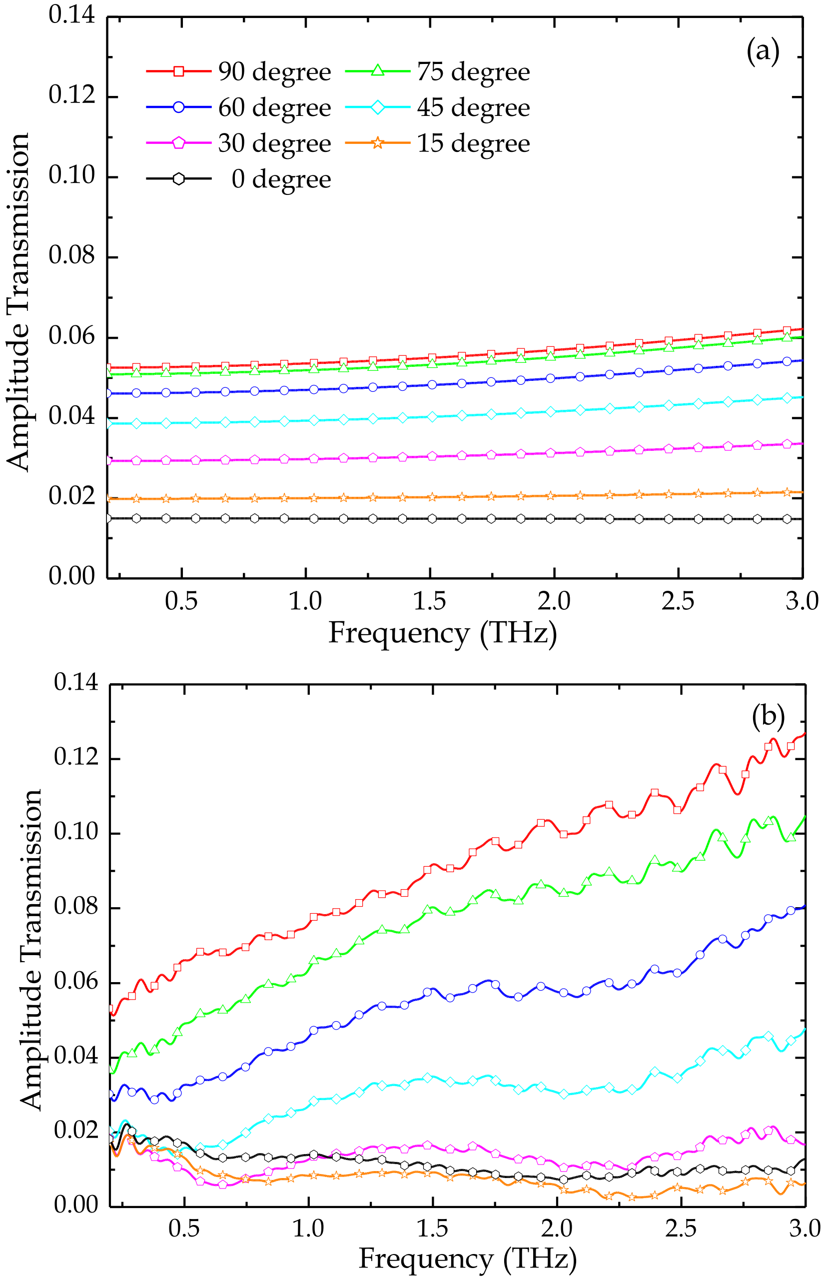

Figure 7-5. Normalized amplitude transmission spectra for various incident polarizations. (a) Simulated transmission spectra of the Ag nanorod array. (b) Experimental transmission spectra.

Such polarization-dependent properties of the AgNRs can be used to design subwavelength plasmonic THz devices [67,141]. The AgNR film is lithographically patterned with a periodic array of subwavelength holes. The inset of Fig. 7-6(a) shows that the dimension of the rectangular holes is 100 µm × 80 µm and the lattice constant is 160 µm in both *x* and *y* directions, thus the holes represent 31.25% of the surface area. The holes are smaller than the free-space resonance wavelength, i.e. 600 µm (0.5 THz) in this case. The remaining surface area is uniformly covered with AgNRs. Two arrays are created with identical aperture dimensions, lattice constant, and thickness, but different nanorod orientations with respect to the rectangular holes. The first hole array, inset in Fig. 7-6(a), has the direction of the nanorods tilted along the shorter 80 µm side (*x*-axis) of the holes. We refer to this array as AgNR1. The second hole array, inset in Fig. 7-6(b), has the axis of nanorods tilted along the longer, 100 µm side (*y*-axis) of the holes. We refer to this array as AgNR2. A linearly polarized THz wave is incident at normal incidence onto each of the structured surfaces, with the electric field either parallel or perpendicular to the shorter axis (*x*-axis) of the holes. These two hybrid micro-/nano-structures show distinct THz response.

Figure 7-6(a) shows the THz transmission spectra obtained from hole array AgNR1. When the THz field is parallel to the long axis of the nanorods and the short axis of the holes in AgNR1, we observe the excitation of the fundamental [0,1] SP resonance mode at the metallic nanorod-silicon interface at 0.5 THz. However, as the array AgNR1 is rotated by 90 degrees such that the THz field is parallel to the long axis of the holes, the SP resonance disappears. Thus, the excitation of the SP resonance in the hole array is strongly linked to the excitation of SPs in the individual nanorods. The electronic excitation in each nanorod becomes possible only when the incident THz field is aligned along the longer axis of the nanorods. In Fig. 7-6(b), we observe a similar behavior in the second hole array AgNR2. The fundamental SP resonance mode is excited at 0.5 THz when the E field is aligned along the longer axis of the nanorods as well as of the holes. As this sample is rotated by 90 degrees, the resonance disappears since the THz waves do not couple to the nanorods and fail to excite the SPs. These unique polarization dependent properties are consistent with the idea of anisotropic effective THz conductivity in the Ag nanorod film, and clearly demonstrate an opportunity for developing new and more functional THz components and devices. The SP wave is excited in each nanorod. Since the nanorods are separated with a distance much smaller than the wavelength of the incident electromagnetic wave, the plasmon modes interact strongly with each other through their near fields giving rise to a collective resonance response. The local E field intensity at the resonance could exceed the intensity of incident field by several orders of magnitude. Such intense fields can be exploited for enhanced spectroscopy, nonlinear processes, lithography, sensing and all related applications.

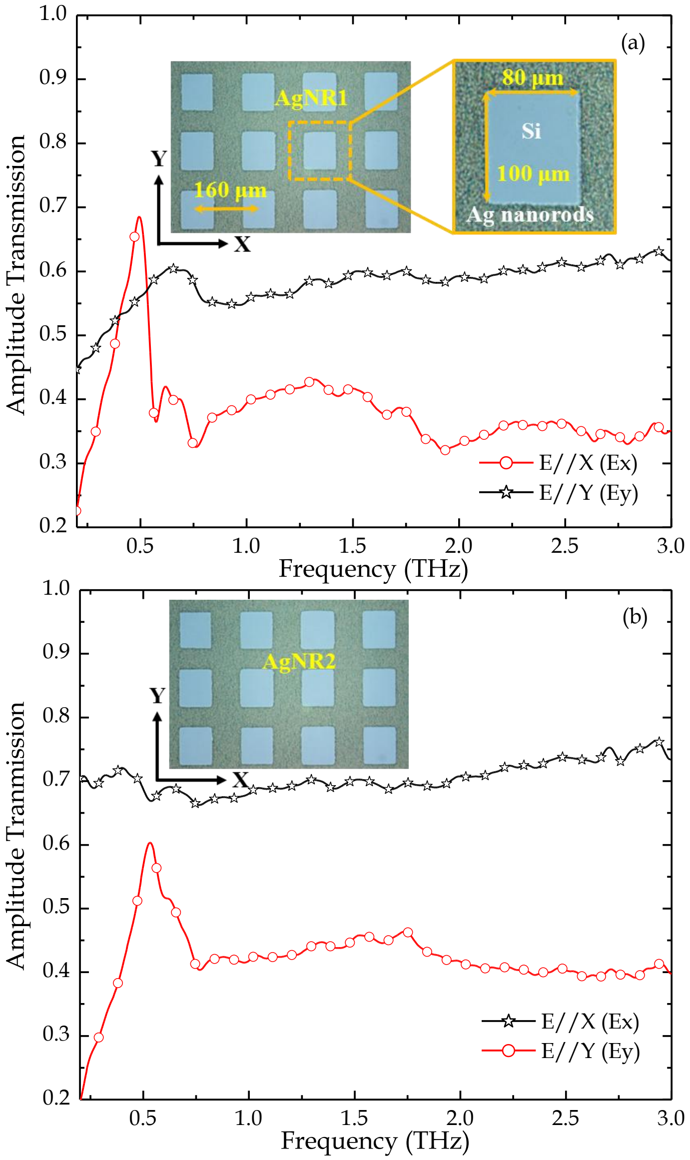

Figure 7-6. Measured transmission through the AgNR arrays patterned with rectangular holes. Spectra of the measured amplitude transmission through both arrays are shown when the E field is polarized either along the short axis or along the long axis of the holes. (a) AgNR1 is patterned with the nanorod projection along the shorter axis of the hole. (b) AgNR2 is patterned with the nanorod projection along the longer axis of the hole. The insets show optical microscope images of the 80 μm × 100 μm rectangular hole arrays in the AgNR films.

7.5 Summary

In summary, the polarization-dependent transmission of THz pulses through Ag nanorod array films is demonstrated both experimentally and numerically by varying the angle between the tilted nanorods and the E field polarization. Resonant extraordinary transmission is measured through Ag nanorod films patterned with periodic arrays of rectangular subwavelength holes on a silicon substrate. The resulting spectroscopy points to the selective excitation of SPs according to the anisotropic conductivity of the nanorod film. Moreover, the results demonstrate that the anisotropic nanoscale surface morphology of the metallic rods gives rise to the material anisotropy observed at THz wavelengths ~3 orders of magnitude longer than the nanorod length scale. These unique material surfaces, used as lithographic substrates onto which subwavelength structures are patterned, provide a means for realizing novel THz polarization filtering, switching, tuning, sensing, and narrowband filtering devices. The nanorod plasmonic device also provides for a much increased surface area and intense fields in the interstitial space between the vertical rods that could be exploited for binding biomolecules that the nanorod hole array device would be able to sense easily.

CHAPTER VIII

CONCLUSION

The object to this research has been to engineer the THz metamaterials for various applications in invisibility cloaking, THz imaging, ultrasensitive THz sensing, tunable slow light effect, and nanorod plasmonic devices. There are several impactful results obtained while probing into the exotic behavior of THz metamaterials.

By taking advantage of transformation optics theory, a study of concealing a realistic 3D object from broadband THz waves was numerically and experimentally performed. Metamaterials offer a technical feasible solution for designing and fabricating THz invisibility cloak using isotropic dielectric materials by drilling inhomogeneous holes. This broadband THz invisibility cloak successfully concealed the geometrical and spectroscopic features of a realistic object, rendering it undetectable from 0.3 to 0.6 THz.

Design, realization and measurements of novel THz Luneburg lens based on transformation optics were demonstrated. Both simulated and experimental results indicated the successful demonstration that the transformed Luneburg lens with gradient refractive index was capable of delivering superior image quality with the resolution very close to the diffraction limit, due to taking advantage of the perfect imaging capability of the aberration-free Luneburg lens. The combination of metamaterials and transformation optics set the stage to the further development of advanced optical system with superior imaging performance.

Using high resolution THz-TDS transmission measurements, we experimentally demonstrated that an extremely sharp metamaterial induced transparency appeared, while slightly moving one gap of the unit cell away from the center of one arm to break the symmetry. By using long-range scanning to obviously improve the resolution of THz-TDS system, the Q-factors were effectively enhanced and the radiation losses were further reduced. The extraordinary high Q-factors up to 227.8 was numerically, theoretically and experimentally demonstrated. The proposed metamaterial with an extremely sharp resonant transparency feature can be an outstanding candidate for the ultrasensitive THz sensors.

A thermally tunable hybrid metal superconductor EIT metamaterial and slow-light effects were demonstrated. The PIT phenomenon was derived from the strong coupling between dark metal SRR and bright superconducting CRR leading to a destructive interference of the scattered fields. The slow-light feature of the PIT phenomena in metamaterials can be extremely attractive for in strong light-matter interactions and enhanced nonlinear effects. This hybrid metamaterial opens up the avenues for designing micro-sized active circuitry with switching, modulation, and capabilities of slowing down THz pulses.

We discovered polarization-dependent transmission of THz pulses through the silver nanorod array film while varying the angle between the tilted nanorods and the electric field polarization. Resonant extraordinary transmission was explored through silver nanorod films patterned with periodic arrays of rectangular subwavelength holes on a silicon substrate. The resulting spectroscopy indicates that the selective excitation of SPs according to the anisotropic conductivity of the nanorod film. Moreover, the results demonstrated that the THz plasmonic metamaterial anisotropic properties were derived from the anisotropic nanoscale surface morphology of the metallic rods. These unique nanorod plasmonic devices, which combine nanostructured thin films with microstructured plasmonic metamterials, provide a means for realizing novel THz polarization filtering, switching, tuning, sensing, and narrowband filtering devices.

REFERENCES

1. S. Linden, C. Enkrich, M. Wegener, J. Zhou, T. Koschny, and C. M. Soukolis, “Magnetic response of metamaterials at 100 terahertz,” Science **306**, 1351 (2004).
2. T. J. Yen, W. J. Padilla, N. Fang, D. C. Vier, D. R. Smith, J. B. Pendry, D. N. Basov, and X. Zhang, “Terahertz magnetic response from artificial materials,” Science **303**, 1494 (2004).
3. A. K. Azad, J. M. Dai, and W. Zhang, “Transmission properties of terahertz pulses through subwavelength double split-ring resonators,” Opt. Lett. **31**, 634 (2006).
4. H. T. Chen, W. J. Padilla, J. M. O. Zide, A. C. Gossard, A. J. Taylor, and R. D. Averitt, “Active terahertz metamaterial devices,” Nature **444**, 597 (2006).
5. H. T. Chen, J. F. O‘Hara, A.K. Azad, A. J. Taylor, R.D. Averitt, D.B. Shrekenhamer and W. J. Padilla, “Experimental demonstration of frequency-agile terahertz metamaterials,” Nat. Photonics **2**, 295 (2008).
6. R. Singh, E. Smirnova, A. J. Taylor, J. F. O‘Hara, and W. Zhang, “Optically thin terahertz metamaterials,” Opt. Express **16**, 6537 (2008).
7. W. J. Padilla, A. J. Taylor, C. Highstrete, M. Lee, and R. D. Averitt, “Dynamical electric and magnetic metamaterial response at terahertz frequencies,” Phys. Rev. Lett. **96**, 107401 (2006).
8. U. Leonhardt, “Optical conformal mapping,” Science **312**, 1777 (2006).

9. J. B. Pendry, D. Schurig, and D. R. Smith, “Controlling electromagnetic fields,” Science **312**, 1780 (2006).
10. W. S. Cai, U. K. Chettiar, A. V. Kildishev, and V. M. Shalaev, “Optical cloaking with metamaterials,” Nat. Photonics **1**, 224 (2007).
11. J. Li, and J. B. Pendry, “Hiding under the carpet: a new strategy for cloaking,” Phys. Rev. Lett. **101**, 203901 (2008).
12. D. Schurig, J. J. Mock, B. J. Justice, S. A. Cummer, J. B. Pendry, A. F. Starr, and D. R. Smith, “Metamaterial electromagnetic cloak at microwave frequencies,” Science **314**, 977 (2006).
13. R. Liu, C. Ji, J. J. Mock, J. Y. Chin, T. J. Cui, and D. R. Smith, “Broadband ground-plane cloak,” Science **323**, 366 (2009).
14. L. H. Gabrielli, J. Cardenas, C. B. Poitras, and M. Lipson, “Silicon nanostructure cloak operating at optical frequencies,” Nat. Photonics **3**, 461 (2009).
15. J. Valentine, J. S. Li, T. Zentgraf, G. Bartal, and X. Zhang, “An optical cloak made of dielectrics,” Nat. Mater. **8**, 568 (2009).
16. T. Ergin, N. Stenger, P. Brenner, J. B. Pendry, and M. Wegener, “Three-dimensional invisibility cloak at optical wavelengths,” Science **328**, 337 (2010).
17. H. F. Ma, and T. J. Cui, “Three-dimensional broadband ground-plane cloak made of metamaterials,” Nat. Commun. **1**, 21 (2010).
18. B. Ferguson, and X. C. Zhang, “Materials for terahertz science and technology,” Nat. Mater. **1**, 26 (2002).
19. P. H. Siegel, “Terahertz technology,” IEEE Microwave Theory Tech. **50**, 910 (2002).

20. D. Schurig, J. B. Pendry, and D. R. Smith, “Calculation of material properties and ray tracing in transformation media,” Opt. Express **14**, 9794 (2006).
21. D. Schurig, “An aberration-free lens with zero F-number,” New J. Phys. **10**, 115034 (2008).
22. D. Grischkowsky, S. Keiding, M. Vanexter, and C. Fattinger, “Far-infrared time-domain spectroscopy with terahertz beams of dielectrics and semiconductors,” J. Opt. Soc. Am. B **7**, 2006 (1990).
23. A. D. Falco, S. C. Kehr, and U. Leonhardt, “Luneburg lens in silicon photonics,” Opt. Express **19**, 5156 (2011).
24. C. L. G. Alzar, M. A. G. Martinez, and P. Nussenzveig, “Classical analog of electromagnetically induced transparency,” Am. J. Phys. **70**, 37 (2002).
25. P. Tassin, L. Zhang, T. Koschny, E. N. Economou, and C. M. Soukoulis, “Low-loss metamaterials based on classical electromagnetically induced transparency,” Phys. Rev. Lett. **102**, 053901 (2009).
26. N. Liu, L. Langguth, T. Weiss, J. Kastel, M. Fleischhauer, T. Pfau, and H. Giessen, “Plasmonic analogue of electromagnetically induced transparency at the Drude damping limit,” Nat. Mater. **8**, 758 (2009).
27. R. W. Boyd and D. J. Gauthier, “Controlling the velocity of light pulses,” Science **326**, 1074 (2009).
28. D. K. Ferry, “Quantum mechanics: an introduction for device physicists and electrical engineers (2nd ed.),” CRC Press, (2001).
29. S. Zhang, D. A. Genov, Y. Wang, M. Liu, and X. Zhang, “Plasmon-induced transparency in metamaterials,” Phys. Rev. Lett. **101**, 047401 (2008).

30. J. Gu, R. Singh, X. Liu, X. Zhang, Y. Ma, S. Zhang, S. A. Maier, Z. Tian, A. K. Azad, H. T. Chen, A. J. Taylor, J. Han, and W. Zhang, “Active control of electromagnetically induced transparency analogue in terahertz metamaterials,” Nat. Commun. **3**, 1151 (2012).

31. R. Singh, I. A. I. Al-Naib, M. Koch, and W. Zhang, “Asymmetric planar terahertz metamaterials,” Opt. Exp. **18**, 13044 (2010).

32. A. A. Yanik, A. E. Cetin, M. Huang, A. Artar, S. H. Mousavi, A. Khanikaev, J. H. Connor, G. Shvets, and H. Altug, “Seeing protein monolayers with naked eye through plasmonic fano resonances,” P.N.A.S. **108**, 11784 (2011).

33. R. Singh, A. K. Azad, J. F. O’Hara, A. J. Taylor, and W. Zhang, “Effect of metal permittivity on resonant properties of terahertz metamaterials,” Opt. Lett. **33**, 1506 (2008).

34. R. Singh, C. Rockstuhl, and W. Zhang, “Strong influence of packing density in THz metamaterials,” Appl. Phys. Lett. **97**, 241108 (2010).

35. V. A. Fedotov, M. Rose, S. L. Prosvirnin, N. Papasimakis, and N. I. Zheludev, “Sharp trapped-mode resonances in planar metamaterials with a broken structural symmetry,” Phys. Rev. Lett. **99**, 147401 (2007).

36. R. Singh, I. A. I. Al-Naib, Y. Yang, D. R. Choudhury, W. Cao, C. Rochstuhl, T. Ozaki, R. Morandotti, and W. Zhang, “Observing metamaterial induced transparency using individual Fano resonators with broken symmetry”, Appl. Phys. Lett. **11**, 10315 (2011).

37. I. A. I. Al-Naib, C. Jansen, and M. Koch, “High Q-factor metasurfaces based on miniaturized asymmetric single split resonators,” Appl. Phys. Lett. **94**, 153505 (2009).
38. J. Gu, R. Singh, A. K. Azad, J. Han, A. J. Taylor, J. F. O’Hara, and W. Zhang, “An active hybrid plasmonic metamateria,” Opt. Mater. Express **1**, 31 (2012).
39. D. H. Auston, K. P. Cheung, J. A. Valdmanis, and D. A. Kleinman, “Cherenkov radiation from femtosecond optical pulses in electro-optic media,” Phys. Rev. Lett. **53**, 1555 (1984).
40. M. B. Ketchen, D. Grischkowsky, T. C. Chen, C.C. Chi, I. N. Dulling, N. J. Halas, J. M. Halbout, J. A. Kash, and G. P. Li, “Generation of subpicosecond electrical pulses on coplanar transmission lines,” Appl. Phys. Lett. **48**, 751 (1986).
41. B. B. Hu, and M. C. Nuss, “Imaging with terahertz waves,” Opt. Lett. **20**, 1716 (1995).
42. Y. J. Ding, “Efficient generation of high-power quasi-single-cycle terahertz pulses from a single infrared beam in a second-order nonlinear medium,” Opt. Lett. **29**, 2650 (2004).
43. B. S. Williams, S. Kumar, Q. Hu, and J. L. Reno, “Operation of terahertz quantum-cascade lasers at 164 K in pulsed mode and at 117 K in continuous-wave mode,” Opt. Express **13**, 3331 (2005).
44. M. Tonouchi, “Cutting-edge terahertz technology,” Nat. Photon. **1**, 97 (2007).
45. B. Ferguson, and X. C. Zhang, “Materials for terahertz science and technology,” Nat. Mater. **1**, 26 (2002).

46. R. Mendis, and D. Grischkowsky, “Undistorted guided-wave propagation of subpicosecond terahertz pulses,” Opt. Lett. **26**, 846 (2001).

47. R. D. Averitt, G. Rodriguez, , J. L. W. Siders, S. A. Trugman, and A. J. Taylor, “Conductivity artifacts in optical-pump THz-probe measurements of $YBa_2Cu_3O_7$,” J. Opt. Soc. Am. B **17**, 327 (2000).

48. J. Shan, F. Wang, E. Knoesel, M. Bonn, and T. F. Heinz, “Measurement of the frequency-dependent conductivity of sapphire,” Phys. Rev. Lett. **90**, 247401 (2003).

49. A. G. Markelz, A. Roitberg, and E. J. Heilweil, “Pulsed terahertz spectroscopy of DNA, bovine serum albumin and collagen between 0.1 and 2.0 THz,” Chem. Phys. Lett. **320**, 42 (2000).

50. M. Nagel, P. H. Bolivar, M. Brucherseifer, H. Kurz, A. Bosserhoff, and R. Büttner, “Integrated THz technology for label-free genetic diagnostics,” App. Phys. Lett. **80**, 154 (2002).

51. S. M. Hanham, A. I. Fernández-Domínguez, J. H. Teng, S. S. Ang, K. P. Lim, S. F. Yoon, C. Y. Ngo, N. Klein, J. B. Pendry, and S. A. Maier, “Broadband terahertz plasmonic response of touching InSb disks,” Adv. Mater. **24**, 226 (2012).

52. A. K. Azad, J. M. Dai, and W. Zhang, “Transmission properties of terahertz pulses through subwavelength double split-ring resonators,” Opt. Lett. **31**, 634 (2006).

53. R. Singh, A. K. Azad, J. F. O'Hara, A. J. Taylor, and W. Zhang, " Effect of metal permittivity on resonant properties of terahertz metamaterials," Opt. Lett. **33**, 1506 (2008).

54. S. Zhang, Y. S. Park, J. Li, X. Lu, W. Zhang, and X. Zhang, "Negative refractive index in chiral metamaterials," Phys. Rev. Lett. **102**, 023901 (2009).

55. H. T. Chen, W. J. Padilla, M. J. Cich, A. K. Azad, R. D. Averitt, and A. J. Taylor, "A metamaterial solid-state terahertz phase modulator," Nat. Photon. **3**, 148 (2009).

56. H. Tao, N. I. Landy, C. M. Bingham, X. Zhang, R. D. Averitt, and W. J. Padilla, "A metamaterial absorber for the terahertz regime: design, fabrication and characterization," Opt. Express **16**, 7181 (2008).

57. F. Zhou, Y. Bao, W. Cao, J. Gu, W. Zhang, and C. Sun, "Hiding a realistic object using a broadband terahertz invisibility cloak," Sci. Rep. **1**, 78 (2011).

58. D. Liang, J. Gu, J. Han, Y. Yang, S. Zhang, and W. Zhang, "Robust large dimension terahertz cloaking," Adv. Mater. **24**, 916 (2012).

59. J. F. O'Hara, R. Singh, I. Brener, E. Smirnova, J. Han, A. J. Taylor, and W. Zhang "Thin-film sensing with planar terahertz metamaterials: sensitivity and limitations," Opt. Express **16**, 1786 (2008).

60. S. Y. Chiam, R. Singh, J. Gu, J. Han, W. Zhang, and A. A. Bettiol, "Increased frequency shifts in high aspect ratio terahertz split ring resonators," Appl. Phys. Lett. **94**, 064102 (2009).

61. C. Debus, and P. H. Bolivar, "Frequency selective surfaces for high sensitivity terahertz sensing," Appl. Phys. Lett. **91**, 184102 (2007).

62. R. Singh, C. Rockstuhl, C. Menzel, T. P. Meyrath, M. He, H. Giessen, F. Lederer, and W. Zhang, "Spiral-type terahertz antennas and the manifestation of the Mushiake principle," Opt. Express **17**, 9971 (2009).
63. P. Biagioni, J. S. Huang, and B. Hecht, "Nanoantennas for visible and infrared radiation," Rep. Prog. Phys. **75**, 024402 (2012).
64. L.a Razzari, A. Toma, M. Shalaby, M. Clerici, R. P. Zaccaria, C. Liberale, S. Marras, I. A. I. Al-Naib, G. Das, F. D. Angelis, M. Peccianti, A. Falqui, T. Ozaki, R. Morandotti, and E. D. Fabrizio, "Extremely large extinction efficiency and field enhancement in terahertz resonant dipole nanoantennas," Opt. Express **19**, 26088 (2011).
65. L. Razzari, A. Toma, M. Clerici, M. Shalaby, G. Das, C. Liberale, M. Chirumamilla, R. P. Zaccaria, F. D. Angelis, M. Peccianti, R. Morandotti, and E. D. Fabrizio, "Terahertz dipole nanoantenna arrays: resonance characteristics," Plasmonics **8**, 133 (2013).
66. F. Yang, J. R. Sambles, and G. W. Bradberry, "Long-range surface modes supported by thin films," Phys. Rev. B, **44**, 5855 (1991).
67. D. Qu, D. Grischkowsky, and W. Zhang, "Terahertz transmission properties of thin subwavelength metallic hole arrays," Opt. Lett., **29**, 896 (2004).
68. H. F. Ghaemi, T. Thio, D. E. Grupp, T. W. Ebbesen, and H. J. Lezec, "Surface plasmons enhance optical transmission through subwavelength holes," Phys. Rev. B **58**, 6779 (1998).

69. M. T. Reiten, S. A. Harmon, and R. A. Cheville, “Terahertz beam propagation measured through three-dimensional amplitude profile determination,” J. Opt. Soc. Am. B **20**, 2215 (2003).
70. N. I. Landy, N. Kundtz, and D. R. Smith, “Designing three-dimensional transformation optical media using quasiconformal coordinate transformations,” Phys. Rev. Lett. **105**, 193902 (2010).
71. C. Sun, N. Fang, D. M. Wu, and X. Zhang, “Projection micro-stereolithography using digital micro-mirror dynamic mask,” Sensor Actuat a-Phys **121**, 113 (2005).
72. E. R. Brown, J. E. Bjarnason, A. M. Fedor, and T. M. Korter, “On the strong and narrow absorption signature in lactose at 0.53 THz,” Appl. Phys. Lett. **90**, 061908 (2007).
73. Z. Liang, D. R. Williams, “Aberrations and retinal image quality of the normal human eye,” J. Opt. Soc. Am. A **14**, 2873 (1997).
74. A. Walther, “Irreducible Aberrations of a Lens Used for a Range of Magnifications,” J. Opt. Soc. Am. A **6**, 415 (1989).
75. G. Schulz, “Primary Aberration-Free Imaging by 3 Refracting Surfaces,” J. Opt. Soc. Am. **70**, 1149 (1980).
76. E. Ben-Eliezer, E. Marom, “Aberration-free superresolution imaging via binary speckle pattern encoding and processing,” J. Opt. Soc. Am. A **24**, 1003 (2007).
77. E. J. Botcherby, C. W. Smith, M. M. Kohl, D. Debarre, M. J. Booth, R. Juskaitis, O. Paulsen, and T. Wilson, “Aberration-free three-dimensional multiphoton imaging of neuronal activity at kHz rates,” P. Natl. Acad. Sci. USA **109**, 2919 (2012).

78. K. J. Siebert, H. Quast, R. Leonhardt, T. Loffler, M. Thosmson, T. Bauer, H. G. Roskos, and S. Czasch, “Continuous-wave all-optoelectronic terahertz imaging,” Appl. Phys. Lett. **80**, 3003 (2002).
79. Y. H. Lo, R. Leonhardt, “Aspheric lenses for terahertz imaging,” Opt. Express **16**, 15991 (2008).
80. M. Lentzen, B. Jahnen, C. L. Jia, A. Thust, K. Tilmann, and K. Urban, “High-resolution imaging with an aberration-corrected transmission electron microscope,” Ultramicroscopy **92**, 233 (2002).
81. H. Lv, B. R. Shi, L. J. Guo, and A. M. Liu, “Fabrication of Maxwell fish-eye spherical lenses and research on distribution profiles of gradient refractive index,” J. Opt. Soc. Am. A **25**, 609 (2008).
82. Y. G. Ma, C. K. Ong, T. Tyc, and U. Leonhardt, “An omnidirectional retroreflector based on the transmutation of dielectric singularities,” Nat. Mater. **8**, 639 (2009).
83. D. R. Smith, Y. Urzhumov, N. B. Kundtz, and N. I. Landy, “Enhancing imaging systems using transformation optics,” Opt. Express **18**, 21238 (2010).
84. J. M. Gordon, “Spherical gradient-index lenses as perfect imaging and maximum power transfer devices,” Appl. Optics **39**, 3825 (2000).
85. Y. J. Bao, C. He, F. Zhou, C. Stuart, and C. Sun, “A realistic design of three-dimensional full cloak at terahertz frequencies,” Appl. Phys. Lett. **101**, 031910 (2012).
86. Y. M. Liu, and X. Zhang, “Recent advances in transformation optics,” Nanoscale **4**, 5277 (2012).

87. H. F. Ma, and T. J. Cui, “Three-dimensional broadband and broad-angle transformation-optics lens,” Nat. commun. **1**, 124 (2010).
88. F. Zhou, W. Cao, B. Dong, T. Reissman, C. He, W. Zhang, and C. Sun, “A transformed aberration-free Luneburg lens for terahertz imaging,” To be published.
89. N. Kundtz, and D. R. Smith, “Extreme-angle broadband metamaterial lens,” Nat. mater. **9**, 129 (2010).
90. H. F. Ma, ans T. J. Cui, “Three-dimensional broadband and broad-angle transformation-optics lens,” Nat. Commun. **1**, 124 (2010).
91. N. Papasimakis and N. I. Zheludev, “Metamaterial-Induced Transparency Sharp Fano Resonance and Slow Light,” Optics and Photonics News **20**, 22 (2009).
92. S. E. Harris, “Electromagnetically Induced transparency,” Physics Today, **50**, 36 (1997).
93. N. Verellen, Y. Sonnefraud, H. Sobhani, F. Hao, V. V. Moshchalkov, P. V. Dorpe, P. Nordlander, and S. A. Maier, “Fano Resonances in Individual Coherent Plasmonic Nanocavities,” Nano Lett. **9**, 1663 (2009).
94. R. Singh, I. A. I. Al-Naib, Y. Yang, D. R. Chowdhury, W. Cao, C. Rockstuhl, T. Ozaki, R. Morandotti, and W. Zhang, “Observing metamaterial induced transparency in individual Fano resonators with broken symmetry,” Appl. Phys. Lett. **99**, 201107 (2011).
95. W. Cao, R. Singh, I. A. AL-Naib, M. He, A. J. Taylor, and W. Zhang, “Low-loss ultra-high-Q dark mode plasmonic Fano metamaterials,” Opt. Lett. **37**, 16, 3366 (2012).

96. C. Wu, A. B. Khanikaev, and G. Shvets, “Broadband slow light metamaterial based on a double-continuum Fano resonance,” Phys. Rev. Lett. **106**, 107403 (2011).
97. B. Luk’yanchuk, N. I. Zheludev, S. A. Maier, N. J. Halas, P. Nordlander, H. Giessen, and C. T. Chong, “The Fano resonance in plasmonic nanostructures and metamaterials,” Nat. Mater. **9**, 707 (2010).
98. Y. Francescato, V. Giannini, and S.A. Maier, “Plasmonic systems unveiled by Fano resonances,” ACS Nano **6**, 1830 (2012).
99. R. Singh, I. A. I. Al-Naib, M. Koch, and W. Zhang, “Sharp Fano resonances in THz metamaterials,” Opt. Express **19**, 6312 (2011).
100. Y. Ma, Z. Li, Y. Yang, R. Huang, R. Singh, S. Zhang, J. Gu, Z. Tian, J. Han, and W. Zhang, “Plasmon-induced transparency in twisted Fano terahertz metamaterials,” Opt. Mater. Express **1**, 391 (2011).
101. L.V. Hau, S. E. Harris, Z. Dutton, and C. H. Behrooz, “Light speed reduction to 17 metres per second in an ultracold atomic gas,” Nature **397**, 594 (1999).
102. N. Papasimakis, V. A. Fedotov, and N. I. Zheludev, “Metamaterial analog of electromagnetically induced transparency,” Phys. Rev. Lett. **101**, 253903 (2008).
103. Q. Xu, S. Sandhu, M. L. Povinelli, J. Shakya, S. Fan, and M. Lipson, “Experimental Realization of an On-Chip All-Optical Analogue to Electromagnetically Induced Transparency,” Phys. Rev. Lett. **96**, 123901 (2006).
104. R. Singh, C. Rockstuhl, F. Lederer, and W. Zhang, “Coupling between a dark and a bright eigenmode in a terahertz metamaterial,” Phys. Rev. B **79**, 085111 (2009).

105. S. Y. Chiam, R. Singh, C. Rockstuhl, F. Lederer, W. Zhang, and A. A. Bettiol, "Analogue of electromagnetically induced transparency in a terahertz metamaterial," Phys. Rev. B **80**, 153103 (2009).
106. R. D. Kekatpure, E. S. Barnard, W. Cai, and M. L. Brongersma, "Phase-coupled plasmon-induced transparency," Phys. Rev. Lett. **104**, 243902 (2010).
107. J. Gu, R. Singh, X. Liu, X. Zhang, Y. Ma, S. Zhang, S. A. Maier, Z. Tian, A. K. Azad, H. T. Chen, A. J. Taylor, J. Han, and W. Zhang, "Active control of electromagnetically induced transparency analogue in terahertz metamaterials," Nat. Commun. **3**, 1151 (2012).
108. L. Zhang, P. Tassin, T. Koschny, C. Kurter, S. M. Anlage, and C. M. Soukoulis, "Large group delay in a microwave metamaterial analog of electromagnetically induced transparency," Appl. Phys. Lett. **97**, 241904 (2010).
109. J. Zhang, S. Xiao, C. Jeppesen, A. Kristensen, and N. A. Mortensen, "Electromagnetically induced transparency in metamaterials at near-infrared frequency," Opt. Express **18**, 17187 (2010).
110. N. Liu, M. Hentschel, T. Weiss, A. P. Alivisatos, and H. Giessen, "Three-dimensional plasmon rulers," Science **332**, 1407 (2011).
111. R. Taubert, M. Hentschel, J. Kästel, and H. Giessen, "Classical analog of electromagnetically induced absorption in plasmonics," Nano Lett. **12**, 1367 (2012).
112. C. Y. Chen, I. W. Un, N. H. Tai, and T. J. Yen, "Asymmetric coupling between subradiant and superradiant plasmonic resonances and its enhanced sensing performance," Opt. Express **17**, 15372 (2009).

113. Z. G. Dong, H. Liu, J. X. Cao, T. Li, S. M. Wang, S. N. Zhu, and X. Zhang, "Enhanced sensing performance by the plasmonic analog of electromagnetically induced transparency in active metamaterials," Appl. Phys. Lett. **97**, 114101 (2010).

114. X. Liu, J. Gu, R. Singh, Y. Ma, J. Zhu, Z. Tian, M. He, J. Han, and W. Zhang, "Electromagnetically induced transparency in terahertz plasmonic metamaterials via dual excitation pathways of the dark mode," Appl. Phys. Lett. **100**, 131101 (2012).

115. Z. Li, Y. Ma, R. Huang, R. Singh, J. Gu, Z. Tian, J. Han, and W. Zhang, "Manipulating the plasmon-induced transparency in terahertz metamaterials," Opt. Express **19**, 8912 (2011).

116. Q. Bai, C. Liu, J. Chen, C. Cheng, M. Kang, and H. T. Wang, "Tunable slow light in semiconductor metamaterial in a broad terahertz regime," J. Appl. Phys. **107**, 093104 (2010).

117. Y. Lu, X. Jin, H. Zheng, Y. P. Lee, J. Y. Rhee, and W. H. Jang, "Plasmonic electromagnetically-induced transparency in symmetric structures," Opt. Express **18**, 13396 (2010).

118. Y. Lu, J. Y. Rhee, W. H. Jang, and Y. P. Lee, "Active manipulation of plasmonic electromagnetically-induced transparency based on magnetic plasmon resonance," Opt. Express **18**, 20912 (2010).

119. V. T. T. Thuy, N. T. Tung, J. W. Park, V. D. Lam, Y. P. Lee, and J. Y. Rhee, "Highly dispersive transparency in coupled metamaterials," J. Opt. **12**, 115102 (2010).

120. C. Kurter, P. Tassin, L. Zhang, T. Koschny, A. P. Zhuravel, A. V. Ustinov, S. M. Anlage, and C. M. Soukoulis, "Classical analogue of electromagnetically induced transparency with a metal-superconductor hybrid metamaterial," Phys. Rev. Lett. **107**, 043901 (2011).

121. J. Wu, B. Jin, J. Wan, L. Liang, Y. Zhang, T. Jia, C. Cao, L. Kang, W. Xu, J. Chen, and P. Wu, "Superconducting terahertz metamaterials mimicking electromagnetically induced transparency," Appl. Phys. Lett. **99**, 161113 (2011).

122. R. Singh, J. Xiong, A. K. Azad, H. Yang, S. A. Trugman, Q. X. Jia, A. J. Taylor, and H. T. Chen, "Optical tuning and ultrafast dynamics of high-temperature superconducting terahertz metamaterials," Nanophotonics **1**, 117 (2012).

123. W. J. Padilla, A. J. Taylor, C. Highstrete, M. Lee, and R. D. Averitt, "Dynamical electric and magnetic metamaterial response at terahertz frequencies," Phys. Rev. Lett. **96**, 107401 (2006).

124. J. Gu, R. Singh, A. K. Azad, J. Han, A. J. Taylor, J. F. O'Hara, and W. Zhang, "An active hybrid plasmonic metamaterial," Opt. Mater. Express **1**, 31 (2012).

125. R. Singh, Z. Tian, J. Han, C. Rockstuhl, J. Gu, and W. Zhang, "Cryogenic temperatures as a path toward high-Q terahertz metamaterials," Appl. Phys. Lett. **96**, 071114 (2010).

126. R. Singh, D. R. Chowdhury, J. Xiong, H. Yang, A. K. Azad, A. J. Taylor, Q. X. Jia, and H. T. Chen, "Influence of film thickness in THz active metamaterial devices: a comparison between superconductor and metal split-ring resonators," Appl. Phys. Lett. **103**, 061117 (2013).

127. Z. Tian, R. Singh, J. Han, J. Gu, and W. Zhang, “Terahertz superconducting plasmonic hole array,” Opt. Lett. **35**, 3586 (2010).

128. D. R. Chowdhury, R. Singh, A. J. Taylor, H. T. Chen, and A. K. Azad, “Ultrafast manipulation of near field coupling between bright and dark modes in terahertz metamaterial,” Appl. Phys. Lett. **102**, 011122 (2013).

129. D. R. Chowdhury, R. Singh, A. J. Taylor, H. T. Chen, W. Zhang, and A. K. Azad, “Coupling schemes in terahertz planar metamaterials,” Int. J. Opt. **2012**, 148985 (2012).

130. I. Al-Naib, R. Singh, M. Shalaby, T. Ozaki, and Roberto Morandotti, “Enhanced Q-factor in optimally coupled macrocell THz metamaterials: effect of spatial arrangement,” IEEE J. Sel. Top. Quantum Electron. **19**, 8400807 (2013).

131. X. Zhang, Q. Li, W. Cao, J. Gu, R. Singh, Z. Tian, J. Han, and W. Zhang, “Polarization-Independent plasmon-induced transparency in a fourfold symmetric terahertz metamaterial,” IEEE J. Sel. Top. Quantum Electron. **19**, 8400707 (2013).

132. S. B. Chaney, S. Shanmukh, Y. P. Zhao, and R. A. Dluhy, “Aligned silver nanorod arrays produce high sensitivity surface-enhanced Raman spectroscopy substrates,” Appl. Phys. Lett. **87**, 031908 (2005).

133. J. D. Driskell, S. Shanmukh, Y. Liu, S. B. Chaney, X. J. Tang, Y. P. Zhao, and R. A. Dluhy, “The use of aligned silver nanorod arrays prepared by oblique angle deposition as surface enhanced Raman scattering substrates,” J. Phys. Chem. C **112**, 895 (2008).

134. Y. J. Liu, H. Y. Chu, and Y. P. Zhao, “Silver nanorod array substrates fabricated by oblique angle deposition: morphological, optical, and SERS characterizations,” J. Phys. Chem. C **114**, 8176 (2010).
135. W. Zhang, “Resonant terahertz transmission in plasmonic arrays of subwavelength holes,” Eur. Phys. J. Appl. Phys. **43**, 1 (2008).
136. A. Taflove, and S. C. Hagness, “Computational electrodynamics: the finite-difference time-domain method,” 3rd ed. Artech House, (2005).
137. J. D. Jackson, “Classical Electrodynamics,” 3rd ed. John Wiley & Sons: New York, (1998).
138. K. S. Kunz, and R. J. Luebbers, “The finite difference time domain method for electromagnetics,” CRC Press: Boca Raton, (1993).
139. M. A. Ordal, L. L. Long, R. J. Bell, S. E. Bell, R. R. Bell, R. W. Alexander, Jr., and C. A. Ward, “Optical properties of the metals Al, Co, Cu, Au, Fe, Pb, Ni, Pd, Pt, Ag, Ti, and W in the infrared and far infrared,” Appl. Opt. **22**, 1099 (1983).
140. J. Valentine1, S. Zhang, T. Zentgraf, E. Ulin-Avila, D. A. Genov, G. Bartal, and X. Zhang, “Three-dimensional optical metamaterial with a negative refractive index,” Nat. Mater. **455**, 376 (2008).
141. W. Zhang, A. K. Azad, and J. Han, “Direct observation of a transition of a surface plasmon resonance from a photonic crystal effect,” Phys. Rev. Lett. **98**, 183901 (2007).

VITA

Wei Cao

Candidate for the Degree of

Doctor of Philosophy

Dissertation: STUDIES OF TERAHERTZ METAMATERIALS IN TRANSFORMATION OPTICS AND PLASMONICS

Major Field: Electrical Engineering

Biographical:

Education:

Received the Bachelor degree in Electrical Engineering from Tianjin University, China, in July 2007; and received the Master degree in Electrical Engineering from Tianjin University, China, in June 2009. Completed the requirements for the Doctor of Philosophy in Electrical Engineering at Oklahoma State University, Stillwater, Oklahoma in May, 2014.

Experience:

Employed by Oklahoma State University, Department of Electrical Engineering as a research assistant, 2009 to present.

Professional Memberships:

Student member of Optical Society of America (OSA).